Dissertation

Iontronic chemotherapy: a new treatment method for glioblastoma multiforme

submitted by

Linda WALDHERR

MSc, BSc

Dissertation submitted for the Degree of

Doctor of Philosophy (PhD)

at the

Medical University of Graz

Gottfried Schatz Research Center for Cell Signaling, Metabolism and Aging

Chair of Biophysics

under the supervision of

Ass.-Prof. Priv.-Doz. Dipl.-Ing. Dr.techn. Rainer SCHINDL

2020

Statutory Declaration

I hereby declare that this thesis is my own original work and that I have fully acknowledged by name all of those individuals and organizations that have contributed to the research for this thesis. Due acknowledgement has been made in the text to all other material used. Throughout this thesis and in all related publications I followed the "Guidelines of the Medical University of Graz on Good Scientific Practice".

Graz, October 30, 2020

Disclosures

Part of this thesis has been published in

2020 **Blockage of store-operated Ca^{2+} influx by Synta66 is mediated by direct inhibition of the Ca^{2+} selective Orai1 pore**
Linda Waldherr, Adela Tiffner, Deepti Mishra, Matthias Sallinger, Romana Schober, Irene Frischauf, Tony Schmidt, Verena Handl, Peter Sagmeister, Manuel Köckinger, Isabella Derler, Muammer Üçal, Daniel Bonhenry*, Silke Patz* and Rainer Schindl*

During my PhD thesis I also contributed to the following publications

2020 **Luminal STIM1 mutants that cause tubular aggregate myopathy promote autophagic processes**
Matthias Sallinger, Adela Tiffner, Tony Schmidt, Daniel Bonhenry, Linda Waldherr, Irene Frischauf, Victoria Lunz, Isabella Derler, Romana Schober*, Rainer Schindl*
International Journal of Molecular Sciences – Biochemistry

2019 **Sequential activation of STIM1 links Ca^{2+} with luminal domain unfolding**
Romana Schober, Daniel Bonhenry, Victoria Lunz, Adela Krizova, Irene Frischauf, Marc Fahrner, Linda Waldherr, Isabella Derler, Christoph Romanin, Rüdiger H. Ettrich and Rainer Schindl
Science Signaling

2019 **Mechanistic insights into the Orai channel by molecular dynamics simulations**
Daniel Bonhenry, Romana Schober, Tony Schmidt, Linda Waldherr, Rüdiger H. Ettrich and Rainer Schindl
Seminars in Cell and Developmental Biology

2018 **STIM1 and Orai1 regulate Ca^{2+} microdomains for activation of transcription**
Romana Schober, Linda Waldherr, Tony Schmidt, Annarita Graziani, Clemens Stilianu, Lorenz Legat, Klaus Groschner, Rainer Schindl
Biochimica et Biophysica Acta (BBA) - Molecular Cell Research

All co-authors have agreed to the inclusion of their published data in the dissertation. The reproduction of illustrations and figures published from own or third-party publications is granted.

Acknowledgements

During my PhD time I had the opportunity to meet and work together with the most inspiring, instructive and supportive people. I would like to thank each one of them for their help and making this journey such an exciting and thrilling one.

My special thanks go to my mentor and PI Rainer Schindl, without whom this project I am now so eagerly working on, would never have been “born and raised”. His open-mindedness and cooperative spirit showed me that bringing new ideas to life is not only exciting, but also brings all different people with diverse background to sit together on one table – or occasionally also in the mountains.

This leads me to Silke Patz, who was a supporter and mentor of the project from the very beginning. She introduced me to the vast world of neuroscience in such a friendly and clear way that I always felt in good hands, thank you!

I also want to express special thanks to my colleagues from Linköping University, SE, especially Daniel Simon, Maria Seitanidou, Marie Jakešová and Meysam Karami Rad – without their effort this project would not exist and I am very grateful for their help.

Over the last years we established a network of scientists that were extremely supportive and motivational to work with. Their knowledge and enthusiasm for my projects were not only inspiring but also essential to bring them to the point they are now. Therefore, thank you to Nassim Ghaffari Tabrizi-Wizsy, Martin Asslaber, Kurt Feichtinger, Gord von Campe, Beate Rinner, Tadea Urbanic, Verena Handl, Muammer Üçal, Ruth Birner-Grünberger, Tamara Tomin, Sophie Honeder, Peter Sagmeister, Manuel Köckinger, Adela Tiffner, Romana Schober, Matthias Sallinger, Irene Frischauf, Isabella Derler, Daniel Bonhenry, Deepti Mischra and Maximilian Schinagl.

I would also like to thank the members of my dissertation committee, Klaus Groschner and Roland Malli, for their valuable input, guidance and discussions throughout my PhD time.

Aside from that, I always appreciated the fun and relaxed working environment that I found present at the Institute of Biophysics. Therefore, I would like to thank all the colleagues and members of my lab for their help and welcome. I want to thank in particular my PhD mate Tony Schmidt, making lab work especially inspiring with Taylor Swift tunes, his words of encouragement and interest in my work, and occasional dance sessions in the lab. Grazie, Annarita, per il tuo aiuto e consiglio, e per riccette veramente italiane. Also, I want to thank our "Wuzzler-Partie" including Ruth Prassl and Hans Krebs for making our lunch breaks so fun – Schmackes!

Last but not least, biggest thanks to my parents Lothar and Maria, my sister Johanna and my love Kilian. Thank you for being there, for everything!

As a PhD student I received funding by the Medical University of Graz through the PhD program Molecular Medicine (MOLMED), from the Austrian Science Fund (FWF to Rainer Schindl, project number) and the Austrian Academy of Science (ÖAW DOC fellowship).

Table of Contents

Abbreviations and Definitions

3-TSA	3-(trimethoxysilyl) propyl methacrylate
ACh	Acetyl choline
BBB	blood brain barrier
BCNU	carmustine
CAD	CRAC activation domain
CB	cintredekin besudotox
CC	coiled-coil
CE	capillary electrophoresis
CED	convection-enhanced delivery
CLB	Chlorambucil
CNS	central nervous system
CRAC	Ca^{2+} release-activated Ca^{2+} channel
CSC	cancer stem cell
Cyt	Cytidine
DVF	divalent free
EGF	epidermal growth factor
EGFR	epidermal growth factor receptor
EOR	extent of resection
EphA2	Ephrin type-A receptor 2
EphA3	Ephrin type-A receptor 3
EphB2	Ephrin type-B receptor 2
ER	endoplasmic reticulum
FLAIR	Fluid-attenuated inversion recovery
GABA	γ-aminobutyric acid
GAM	glioma-associated macrophage
GBM	Glioblastoma Multiforme

Gem	Gemcitabine
GemIP	Gemcitabine Ionic Pump
GF	growth factor
Glu	glutamate
GSC	glioblastoma stem cell
ICP	intrinsically conductive polymer
IEM	ion exchange membrane
IL-13RA2	interleukin 13 receptor alpha 2
IRE	Irreversible electroporation
LiU	Linköping University
MDSCs	myeloid-derived suppressor cells
MGMT	O^6-methylguanine methyltransferase
nGBM	newly diagnosed GBM
OEIP	Organic Electronic Ionic Pump
OS	overall survival
PEF	pulsed electric field
PFS	progression free survival
PFS6	PFS rates at 6 months
PM	plasma membrane
PS	phosphatidyl serine
RB	retinoblastoma
RE	reversible electroporation
rGBM	recurrent GBM
RT	radio therapy
RTK	receptor tyrosine kinases
RV	remaining tumor volume
SAM	sterile α-motif

SDS-PAGE	sodium dodecyl sulfate polyacrylamide gel electrophoresis
SERCA	Sarcoplasmic/endoplasmic reticulum calcium ATPase
SOAR	STIM-Orai activating region
SOC	Store Operated Calcium
SOCE	Store Operated Calcium Entry
STIM	Stromal Interaction Molecule
TM	transmembrane
TME	tumor microenvironment
TMZ	Temozolomide
VEGF	vascular endothelial growth factor
µFIP	Microfluidic ionic pump

List of Figures

List of Tables

Part I: Iontronic Chemotherapy as New Treatment Method for Glioblastoma Multiforme

Kurzzusammenfassung

Glioblastome sind die häufigsten malignen Tumore im Gehirn bei Erwachsenen. Aufgrund ihres rapiden Wachstums, ihrer genetischen Heterogenität und der häufig auftretenden Therapieresistenzen sind sie schwer zu behandeln, geschweige denn heilbar. Wir präsentieren einen neuen Ansatz zur Therapie dieser Krebsform, bei der sogenannte organische elektronische Ionenpumpen (kurz Ionenpumpen oder OEIP) für die gezielte und kontrollierte Dosierung von Chemotherapie im Gehirn ihr Debüt haben. Zu Beginn ist getestet worden ob der Transport des Chemotherapeutikums Gemcitabin (Gem) mit Ionenpumpen generell möglich ist. Außerdem haben wir die Toxizität von Gem in Glioblastomzellen, Neuronen und Astrozyten bestimmt und konnten nachweisen, dass Gem ein sehr potentes Mittel gegen Glioblastomzellen ist, jedoch Neuronen und Astrozyten nur wenig von seiner toxischen Wirkung tangiert werden. Außerdem zeigen wir, dass die Administration von Gem mittels Ionenpumpen (sogenannten GemIPs) höchstpräzise und kontrollierbar ist. Schlussendlich konnten wir die Anwendung von GemIPs in in Kulturschalen gezüchteten Mikrotumoren testen. Die GemIP-Behandlung ist so erfolgreich, dass in behandelten Mikrotumoren Apoptose signifikant hochreguliert ist und Zerfall der Tumorstruktur deutlich sichtbar wurde. Mit diesen Ergebnissen konnten wir erfolgreich das Fundament für die Weiterentwicklung einer neuen Therapieform, basierend auf Ionenpumpen, für Glioblastome legen.

Abstract

The therapy of glioblastoma multiforme (GBM), the most common and very aggressive form of brain tumors, is facing many challenges. The consequence of these challenges is that therapy approaches have not been improved for decades, and patients can expect a survival time of 15 months, despite therapeutic measures. To overcome these problems, we utilize the novel technology of organic electronic ionic pumps (OEIPs) to transport chemotherapeutic drugs in a precisely controllable manner for the first time. As first proof of principle, we successfully established the OEIP mediated delivery of the chemotherapeutic drug Gemcitabine (Gem). Subsequently, we determined delivery rates at different operation modes and showed that Gem is a very potent drug to kill GBM cells, while leaving neurons and astrocytes untainted. Next, Gemcitabine Ionic Pumps (GemIPs) were mounted on GBM cells grown in monolayers and we showed that the extent of the cell killing rate due to GemIP treatment is indeed tightly controllable. Lastly, we showed by FACS analysis that GemIP treatment effectively induces apoptosis in GBM spheroids and interferes with spheroid cohesion. These experiments are the first important steps in the development of a novel therapeutic implant based on OEIP technology for treatment of GBM.

1. Introduction

Due to the interdisciplinarity of this project, the introduction is separated into three parts. In part I, I take a close look at the disease glioblastoma multiforme, in part II, organic electronic ionic pumps, the drug delivery method I worked with, will be explained in detail, and lastly, in part III, I will give detailed information about the chemotherapeutics that were used for this work.

1.1. Part I: Glioblastoma Multiforme

1.1.1. General overview

Glioma is a summarizing term for description of malignant tumors of the central nervous system (CNS). Depending on the cell of origin, gliomas are differentiated into astrocytomas, oligodendrogliomas, mixed gliomas, etc. (1). In 2018, there were 291,851 reported new cases of cancers in the brain and nervous system worldwide, and 241,037 reported deaths (2), shown in Figure 1. Of all gliomas, glioblastoma multiforme (GBM) is the most frequent one, accounting up to 16 % of all malignant primary brain tumors (3). GBM is a malignant astrocytoma with an incidence rate of 3.2 cases per 100,000 persons per year (4, 5). It is a deadly, incurable disease with poor prognosis of a median survival time of 15 months after diagnosis (5). Less than 5% of patients survive 5 years after diagnosis (6). This is owed to the rapid growth behavior and genetic heterogeneity of GBM tumors, which can double their volume in ca. 50 days (7). GBMs are practically exclusively found in the brain (8), mostly affecting the supratentorial region (6, 8), however, the high invasiveness leads to infiltration of surrounding brain tissue and high likeliness of tumor recurrence, making full resection of the tumor mass hardly possible.

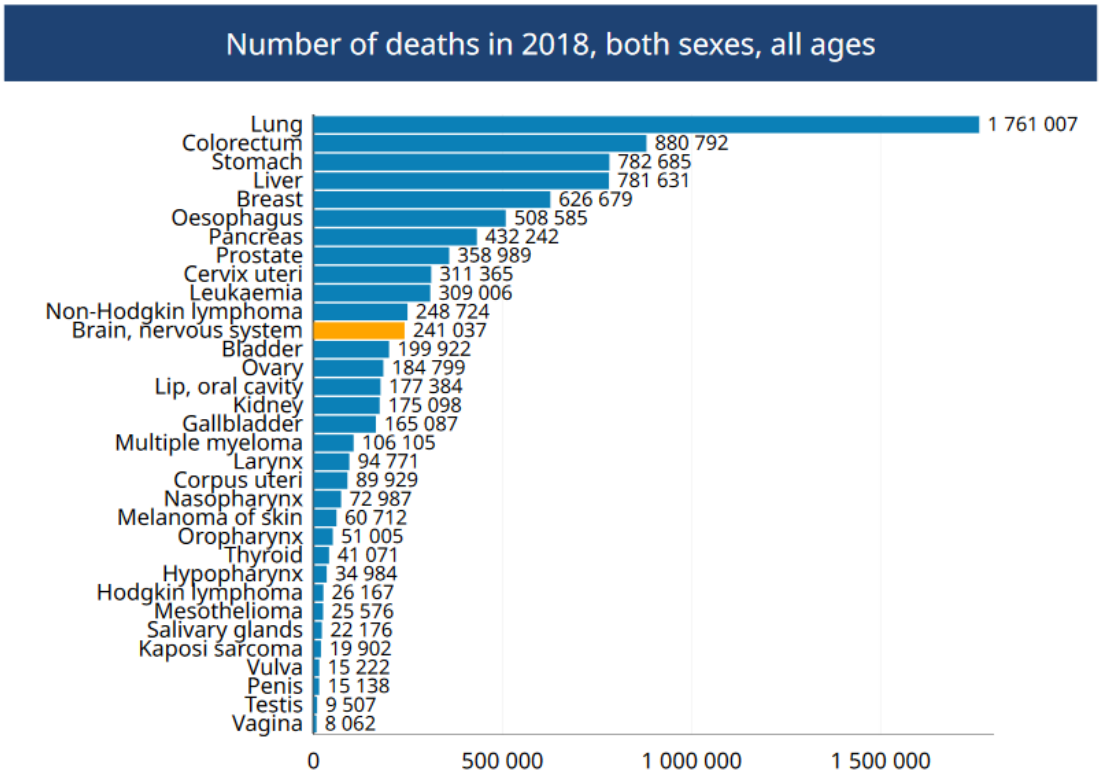

Figure 1 Comparison of number of cancer deaths in 2018
Deaths caused by tumors in the brain and nervous system rank position 12. Data source: GLOBOCAN 2018 (2), reproduced with permission of the publisher "John Wiley and Sons" according to license number 4938200277859 (RightsLink ®).

GBMs are differentiated into primary and secondary GBMs. Most GBMs are of primary nature, mainly occurring in adults above 60 years (5, 9), as described in Figure 2. Secondary GBMs are rare and rather affect younger patients below 45 years (9). Among GBM, four subtypes (grade I-IV) have been identified. These grades are distinct concerning their genetics, disease progression and survival outcomes (8).

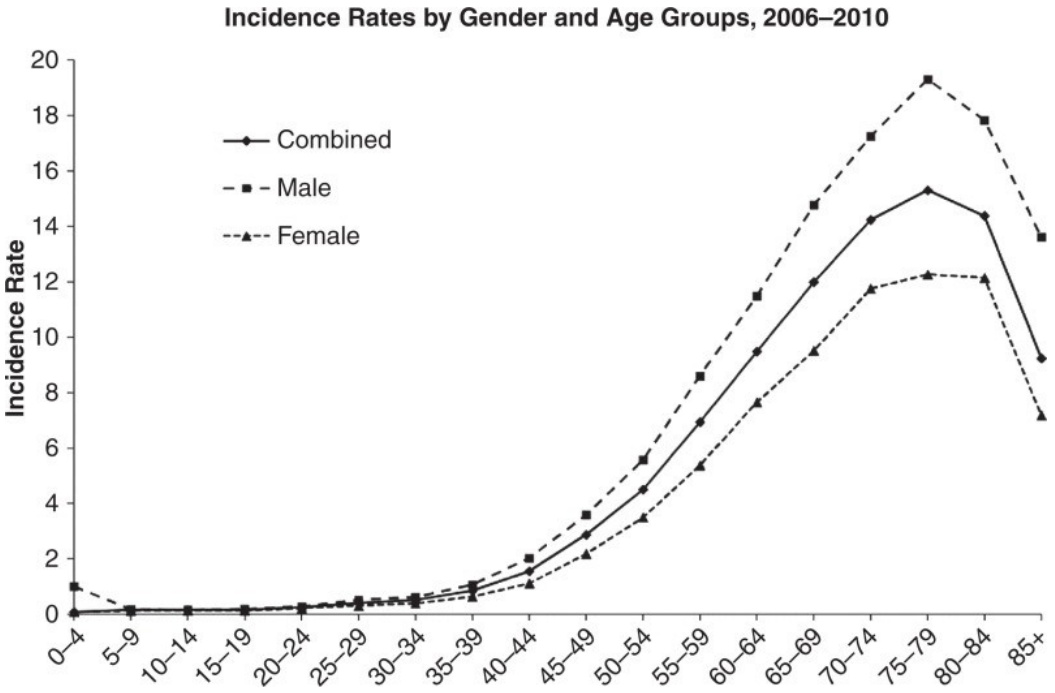

Figure 2 Rates of GBM cases for gender and age groups.
Rates are per 100,000, image reproduced from (5) with permission of the publisher "American Association for Cancer Research" according to license number 4927570684665 (RightsLink ®).

1.1.2. Genetics of GBMs

To describe a GBM based on its genetic characteristics is quite complicated. GBMs are genetically highly heterogeneous, frequently carry genetic mutations, deletions, insertions of amplifications and are extremely instable. This goes even as far as intratumor heterogeneity, which means that different tumor cell subpopulations occur within one tumor. All mutations that occur are acquired aberrations. Genetic predispositions or inheritable mutations that make patients more prone to GBM development are unknown (9). Still, three signaling pathways are reported to be abnormally altered and oncogenic in GBM, 1) the receptor tyrosine kinase (RTK) pathways, 2) retinoblastoma (RB) signaling and 3) p53 signaling (9) (Figure 3).

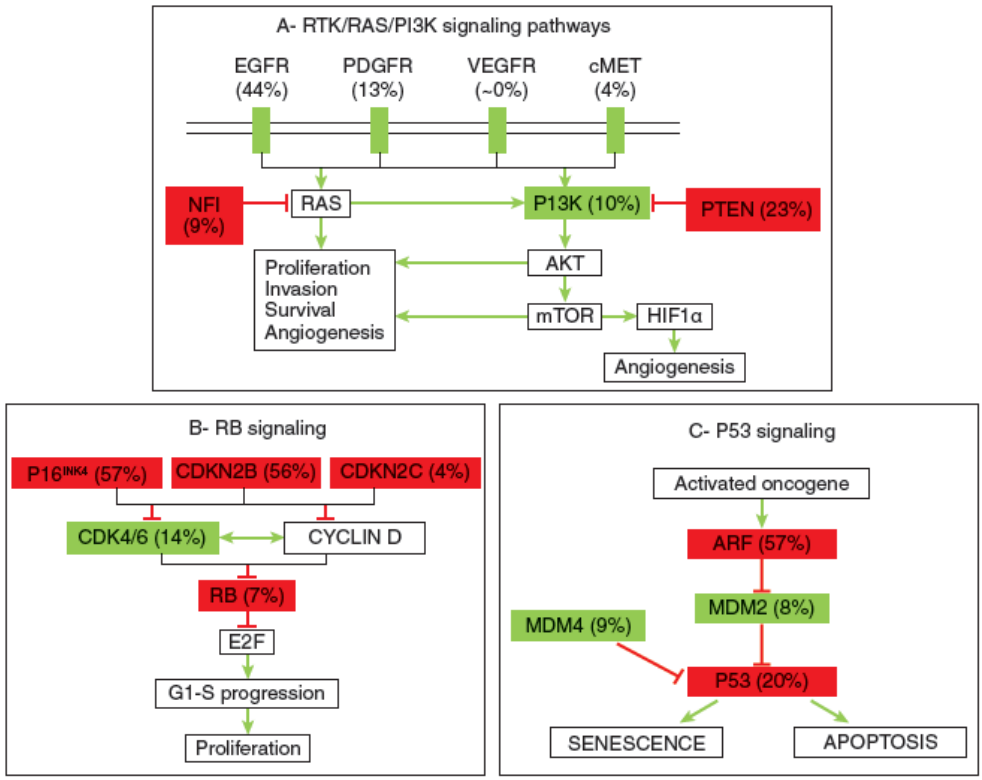

Figure 3 Major genetic alterations in GBM and their frequencies of occurrence.
A) The RTK/Ras/PI3K signaling pathway, B) RB signaling and C) P53 signaling. Green = overactive, red = reduced activity. Figure has been reproduced from (9) with permission of the authors and according to Creative Commons Attribution 4.0 International (CC BY 4.0).

The RTK signaling pathway involves receptors of growth factors (GFs), such as epidermal growth factor receptor (EGFR) and many others. Via different mechanisms (mutations, overexpression of receptor or ligand, genetic amplification), which can co-exist in one tumor, EGFR is overexpressed in the majority of GBMs. As a consequence of EGFR activation, the Ras pathway is also often overly active in GBM and thus, promotes proliferation, survival and migration (9) (Figure 3A). Another frequent observation is the GF induced over-stimulation of the Phosphatidylinositol-4,5-Bisphosphate 3-Kinase/Phosphatase (PI3K) and Tensin Homolog/serine threonine kinase Akt (PTEN/Akt) pathway (Figure 3A). This results, again, in increased proliferation and reduction of apoptosis.

Another commonly observed alteration in GBM genetics is the RB pathway, which plays a role in the cell cycle (Figure 3B). In healthy cells, RB is either inactive and binds the growth factor E2F (resting cells) or becomes phosphorylated during proliferation and releases E2F, which promotes DNA synthesis. This is regulated by negative feedback mechanisms. In GBM, this negative regulation is overcome by RB promotor methylation and results in major discrepancies in the cell cycle.

As in many other cancers, the TP53 pathway is also likely to malfunction in GBM (Figure 3C). As the major DNA damage responder protein, TP53, can either induce DNA repair or, in case of major damage, induction of cell death. In Gliomas, most mutations in TP53 gene are missense mutations that result in DNA binding complications (9).

To date, it is known that the above-mentioned pathways are likely to be abnormally regulated in GBM, however, a series of genetic events that lead to the development of GBM is not known, maybe not even existing (9). The occurrence of the above-mentioned mutations, in combination with many other aberrations can, but not exclusively have to, lead to the development of this disease.

1.1.3. GBM Microenvironment

In GBM, tumor cells are surrounded by different cell populations, comprising cancer stem cells, immune cells, stromal cells, vascular endothelial cells and pericytes (10). Together, they form the tumor microenvironment (TME), shown in Figure 4.

As already mentioned, due to the high intratumor heterogeneity, it is possible more than one molecular variant of GBM cells reside in different compartments of one single tumor (11). This united cell structure forms proliferating and hypoxic areas, and has infiltrating and angiogenic niches that closely interact with the extracellular matrix. GBMs are well vascularized tumors, which is owed to overexpression of vascular endothelial growth factor (VEGF) in the TME (12). VEGF overexpression stimulates neo-angiogenesis, which is, however, abnormal and dysfunctional and results in hypoxic and necrotic areas in the tumor mass (13). It is shown that

the angiogenic and hypoxic niche interact with each other and often support GBM cancer stem cell subpopulations (14).

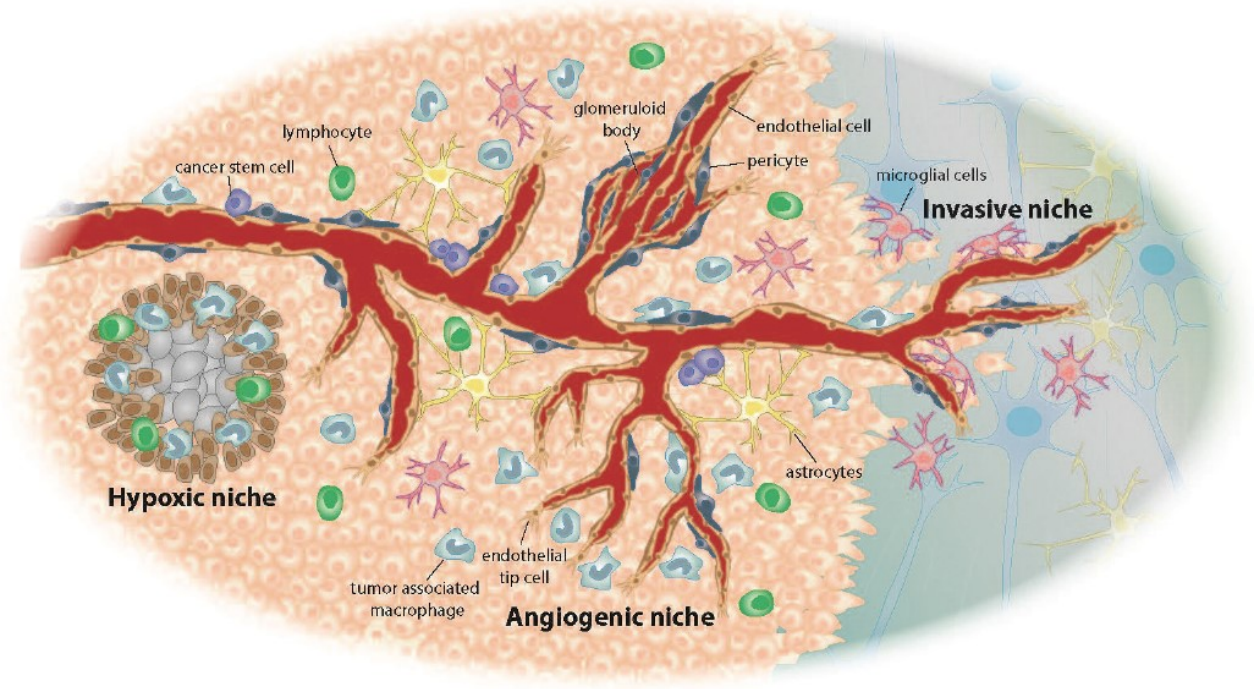

Figure 4: Tumor microenvironment.
Different niches (hypoxic, angiogenic and invasive) occur in GBM. These niches host different cell types, such as cancer stem cells, microglia, endothelial cells, etc. Figure has been reproduced from (10) with permission of the authors according to Creative Commons Attribution 4.0 International (CC BY 4.0).

Among all cell subpopulations found in a single solid GBM, cancer stem cells (CSCs) are probably the hardest to deal with. CSCs are somatic stem cells, and are also called “tumor-initiating cells” or “tumorigenic cells” (15). Stem cells in general are found in niches of various tissues and in general have the potential to a) renew themselves and proliferate, b) differentiate into different lineages due to their multipotent character and c) keep an equilibrium between self-renewal and differentiation, which controls the stem cell number (16). CSCs, therefore, differentiate into the tumor phenotype they originally derive from (17), however, due to mutations they are withdrawn from the niche control and proliferate uncontrollably. Additionally, these cells bear a tumorigenic potential, enabling them to form a tumor after they are transplanted into foreign tissue (16). Due to their special functions, CSCs bear chemo- and radiation resistance, and

consequently initiate tumor recurrence (18, 19). Glioblastoma stem cell (GSC) identification is not trivial, since proper biomarkers are not clearly identified (20, 21) and as a consequence, not applicable for GBM prognosis (22). However, some markers such as CD133 (15), Nanog (23), KlF4 (23), CD44 (24) and ABC transporters (20, 25) seem the most dependable. In GBM, GSCs are found in perivascular niches, in which a GSC-nurturing hypoxic microenvironment is predominant (26). Due to hypoxia, GSCs stabilize hypoxia inducible factors (e.g. HIF-1 (27), HIF-2α (28)), which consequently lead to overexpression of VEGF. This results in neoangiogenesis, which is, as already mentioned, abnormal and dysfunctional, and therefore again hypoxic regions that promote GSC niche development are formed (27). As a result, hypoxic regions in GBM are not exclusively the scene of cell death and necrosis (as in healthy tissue), but they are also a hub for strongly proliferating GSCs, that are generally chemo- and radio resistant. It is obvious that GSCs are a major target in GBM therapy, however, a difficult one to tackle.

Another important cell subpopulation in the TME, responsible for GBM invasiveness and infiltration, are immune cells. 30-50% of the GBM tumor volume can be made up by immune cells (29, 30), especially myeloid-derived suppressor cells (MDSCs) and tumor-associated macrophages (TAMs) (31). GBM cells release chemokines, which attract these cells and lead to their invasion and finally accumulation in the GBM microenvironment (30, 32). In parallel to this, TAMs are not only attracted, but also release supportive factors for proliferation and migration themselves (33) (e.g. release of epidermal growth factor (EGF) (32) and stress-inducible protein 1 (STI1) (34)). Due to their migratory functions, immune cells play a vital role in GBM invasiveness and infiltration.

1.1.4. Standard GBM treatment in the clinics

1.1.4.1. Standard treatment in newly diagnosed GBM

Treatment of newly diagnosed GBM (nGBM) is constituted of three pillars: 1) surgical resection of the maximum tumor mass, followed by 2) radiation therapy and 3) concomitant chemotherapy with temozolomide (TMZ) (35). With these measures, patients face a median survival of 15 months after initial diagnosis (35). Additional intravenous administration of bevacizumab can

prolong progression free survival (PFS) by ca. 3 months, however, does not influence overall survival (OS) (36, 37).

The fist pillar, surgical resection, is vital in the fight against this tumor. Since the extent of resection (EOR) is strongly associated with life expectancy, a maximum safe resection is performed (38-40). Therefore, the tumor cells are visualized by the fluorescent agent 5-aminolevulinic acid (5-ALA; Gleolan®), which roughly indicates the tumor field (41). Additionally, to avoid loss of function, intraoperative stimulation mapping is performed, meaning that patients are awake during resections in eloquent brain areas and therefore the risk of neurologic deficits is reduced (42). One more influencing factor on OS is the remaining tumor volume (RV), which, when it exceeds 2-5 cm^3, significantly reduces survival rates and increases chance of recurrence (40, 43). Aside from resecting the solid tumor, samples are taken for characterization.

The standard of care treatment plan after surgery is a combined therapy of TMZ (75 mg/m^2/day, 7 days per week over 6 weeks) and radiation therapy (RT) of 60 Gy in 30 fractions (focal irradiation in daily fraction of 2 Gy, 5 days a week for 6 weeks), followed by six cycles of temozolomide (150-200 mg/m^2/day for 5 days during each 28 day cycle) (35, 44, 45). This protocol was established by Stupp et al. in 2005 (46), supported by various other trials summarized by Feng et a. (45), is considered a hallmark in GBM care and has remained the best therapeutic option for over a 10 years (47).

TMZ is an alkylating drug that readily passes the blood brain barrier (BBB). In contact with water at physiological pH, the drug gets rapidly hydrolyzed in a base-catalyzed reaction to the compound mitozolomide (MTIC), which further breaks down into a methyldiazonium ion (48, 49). The diazonium ion has high affinity to methylate guanines in the DNA at position O^6, resulting in O^6-methylguanine. This modification can introduce DNA mismatching with thymine and cytosine and point mutations (C:G to T:A transitions) and eventually leads to cell death (49). However, TMZ therapy faces a serious problem, which is TMZ resistance. 50 % of GBM patients are unresponsive to TMZ therapy (50). This is possible due to three molecular mechanisms, 1) overexpression of O^6-methylguanine methyltransferase (MGMT), 2) mismatch repair (MMR) and

3) base excision repair (BER) (49, 50). MGMT is a DNA repair enzyme that can transfer DNA-bound alkyl groups to its own cysteine residues, and therefore, reverses the TMZ methylation effect (49). Both a high expression of MGMT, as well as methylated *MGMT* promotor can indicate whether GBM cells are sensitive to TMZ therapy (51, 52). Still, it is important to keep in mind that, although MGMT expression profile can indicate TMZ sensitivity, it is not the only molecular mechanism that can result in a TMZ resistance.

1.1.4.2. Carmustine/Gliadel wafers

Another, more local approach to treat GBM via nitrosureas is the implantation of biodegradable wafers soaked with the chemotherapeutic drug carmustine (BCNU) into the post-surgical cavity (53, 54). The wafers are biodegradable polymer disks with a diameter of 1.45 cm and are 1 mm thick (FDA, 1996, Ref. ID: 4358718). The polymer is soaked with 7.7 mg BCNU per disk, and maximum of eight wafers can be placed in the post-surgical cavity (FDA, 1996, Ref. ID: 4358718). After placement in the cavity and closure of the patient, the wafers degrade and thereby, release BCNU into its surrounding tissue. The resulting local concentrations are 100-fold higher than those via systemic administration (55). The treatment with Gliadel results in faintly, but significantly, increased mean OS to 16.2 months. However, this increase comes at high cost. The complications caused by these high local cytotoxic concentrations in the brain comprise seizures, myelosuppression, neurologic deficit, wound healing complications, cerebral edemas and infections (55-57). Therefore, application of Gliadel wafers remains to be carefully handled and survival benefit has to be counter valued with incidences of complications.

1.1.5. GBM Recurrence

GBM recurrence is a major problem in GBM treatment. Despite the therapeutic measures, in 80-90 % of cases tumors reappear within a 3 cm area around the resection margin (58-62), shown in Figure 5.

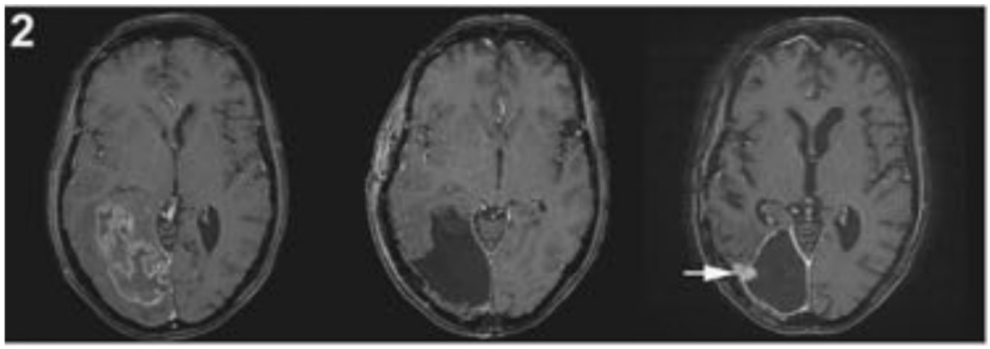

Figure 5 Comparison of MRI scans before and after tumor resection.
Representative gadolinium-enhanced MRI scans showing pre-operative (left), post-operative (middle) and recurrent (right) images. Arrow highlights the recurrence. Image reproduced with modifications from (58) with permission of the authors Kevin Petrecca et al and publisher "Springer Nature" according to license number 4938200698237 (RightsLink ®).

In case of recurrent GBM (rGBM), no standardized therapy protocol is recommended (63, 64). Second surgery is optional for 20-30 % of patients, however, there is a lack of studies that convince to perform such an invasive procedure (63). Re-irradiation is debatable, but again there is lack of incidence that this procedure can improve the OS or PFS (63, 65). In terms of chemotherapy, different other agents (e.g. nitrosureas such as carmustine and lomustine, bevacizumab, re-challenging TMZ) are approved in Europe, improving PFS rates at 6 months (PFS6) by 20-30% (summary of several trials in (64)). Unfortunately, despite some improve in PFS, secondary therapeutic measures do not seem to be promising for OS of GBM patients, yet, and a standardized treatment regimen needs to be developed.

1.1.6. Alternative treatment approaches

For the last 30 years, GBM therapy has remained incurable. It is needless to say that we are in urgent need in developing new treatment approaches that are able to improve patient's chances to fight this aggressive cancer. There are several alternative tactics to treat these tumors, which will be discussed in the following sections.

1.1.6.1. Targeted Cytotoxic Therapy

One major problem in GBM chemotherapy is the BBB. While a few drugs, such as TMZ, readily diffuse over it, many available chemotherapeutics are not able to cross it and therefore, do not reach their site of action. There is scientific interest in designing and synthesizing BBB-passing chemo agents that also target proteins that are over-expressed exclusively in the cancerous brain cells. The receptors IL-13RA2 (66, 67), EphA2 (68-70), EphA3 (71, 72), and EphB2 (73, 74) are considered promising aims of this so-called targeted chemotherapy in GBM, since they are exclusively over-expressed in GBM cells (73). Within the last years, the Debinski Lab (Wake Forest School of Medicine, North Carolina) has pioneered in the development of a cytotoxic drug that tackles all four receptors, a QUAD-CTX (73). From a structural perspective, agents for targeted chemotherapy are cytotoxic derivatives of receptor ligands. For example, the recombinant protein cintredekin besudotox (CB), a combination of interleukin-13 and a Pseudomonas exotoxin, was evaluated in phase I/II/III studies (75-77). Drugs were administered via convection enhanced delivery (see chapter 1.1.6.2), and doses were well tolerated (76). However, OS of patients treated with CB was 10-14 months, depending on catheter positioning of the CED device (75), and could not significantly improve compared to TMZ + RT. This approach may be a new method to treat GBM compartments that are otherwise untreatable – however, it is still in an early stage of development.

1.1.6.2. Convection-Enhanced Delivery

Convection-enhanced delivery (CED) is a catheter-based method for targeted drug delivery to the brain. The technology was developed in the mid-1990s by the group of Edward Oldfield (78, 79). CED devices consist of catheter cannulas that are positioned in the brain, either in the tumor cavity or close to the tumor borders. They cannulas are connected to an external drug reservoir and motor-driven pumps via a burr hole in the skull (illustrated in Figure 6).

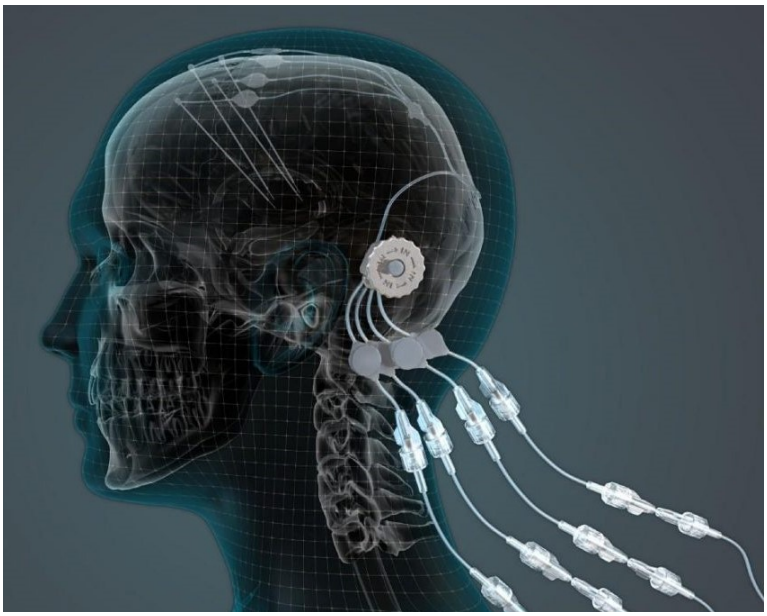

Figure 6: Schematic image of an implanted CED device.
Catheters are placed in the cull and are connected via tubes to the externally placed pumping system. Image reproduced from (80), with permission of “The Cure Parkinson’s Trust”. The reproduction of the illustration is granted.f

In comparison to e.g. carmustine wafers, CED does not rely only on diffusion, but also pressure-driven infusion of drugs (81). Therefore, sufficient delivery of macro molecules (e.g. nanoparticles (82) and CB (76)), as well as their homogenous distribution in the brain tissue can be achieved (79, 83). Typically, a total volume of 5-180 mL of chemotherapeutics are delivered at flow rates between 0.5-10 µL/min (84). This results in spherical drug distribution within a 3 cm area around the release hole of the catheter (40, 78, 81). However, distribution strongly depends on various parameters such as a) molecule size, b) injection volume and c) catheter geometries (85). Also, a serious concern of this technology is backflow and leakage of the released chemotherapeutic along the cannula surface, leading to neural intoxication and skin necrosis, especially at high flow rates and huge infusate volumes (86-88). Aside from this, immediate, early or late adverse events are investigated in several CED studies and are caused by physical brain damage, mechanical stress due to the infusion of fluids and toxicity of the drugs (89). Adverse events comprise from local toxicity, seizures, local toxicity, hemiparesis and headaches (summarized in (89)).

The most prominent clinical trial utilizing CED for GBM treatment was published in the PRECISE trial performed by Kunwar et al. from 2004-2010 (77). In this phase III trial, 296 patients were separated in two groups to receive CB via CED or Gliadel wafers (2:1 ratio). The adverse events did not differ between both arms, only in CB/CED arm the occurrence of pulmonary embolism was significantly increased compared to Gliadel group (8% vs. 1%) (77). However, also the OS was indifferent for both treatment regiments (77). The authors argued that both the variation level of IL13 receptor expression could have had led to minor antitumor effects, as well as insufficient visualization of drug distribution (77).

Although CED seems to be a promising approach in GBM treatment, it still has several drawbacks that need to be improved in order to overweight the costs, adverse events and complexity of this procedure.

1.1.6.3. Irreversible electroporation to overcome BBB limitations

Irreversible electroporation (IRE) uses the principle of electroporation to ablate cancerous tissue. During this strategy, pulsed electric fields (PEFs) are applied to the tissue of interest. The electric field can be either applied by placing two electrodes with opposite polarity or one bipolar electrode in the tissue of interest. In the applied PEF the cell membranes of this tissue form hydrophilic pores (90). If the pulses are moderate, it can be used to transiently permeabilize cell membrane bilayers (91), which is then called reversible electroporation (RE). RE is used for electrochemotherapy, in which cells are permeabilized for transmission of chemo agents, and for delivery of DNA molecules (91). In contrast to this, irreversible electroporation (IRE), can be used to ablate pathological tissue (90). In IRE, the frequency of the electric pulses, or the magnitude of the electric field is increased to cause cellular damage, but importantly, only to an extent that thermal damage is irrelevant (90, 91). This is in contrast to other tissue ablation techniques (microwaves, radiofrequency), which rely on thermal destruction of the tissue. The mechanism of cell death induced by IRE is not exactly clarified, however, it is proposed that cell membranes rupture and apoptosis is induced (90, 92). Therefore, IRE is proposed as cancer treatment that does not rely on chemotherapeutics.

Since 2010, IRE has been used in studies to treat different cancers (91). Typical IRE pulses last 100 µs, with an applied voltage range between 1500-3000 V, with one pulse per second and 90 applied pulses (91). These pulses are known to interfere with nerve function, which has been found to recover within 7 weeks (93). Importantly, during IRE, muscle contractions can occur and therefore, neuroparalytic agents need to be used and carefully monitored during IRE treatment to guarantee proper muscle relaxation and respiration (91).

The application of IRE for brain tumor treatment has not been tested in humans yet. Safety of IRE in the brain has been assessed in canine models, reporting that selected voltages can be safely administered (94). Also, IRE treatment of seven dogs with brain tumors was performed, reported severe *post*-treatment adverse effects that could be partially recovered after 14 days (95).

Currently, IRE is still in an early stage of development and several parameters need to be determined before a safe application in the brain is possible. However, IRE has been proven effective in ablating different cancers in human, and brain cancers in dogs (91). Major obstacles in the further development will be sparing blood vessels and nerves, avoiding local toxicities and leaving the BBB untainted.

1.1.6.4. Opening of the BBB using high-intensity focused ultrasound

This method circumvents the BBB by permeabilizing it locally by applying high-frequency focused ultrasound (HIFU). To perform HIFU, electro-acoustic beams with frequencies ranging from 0.8–5 MHz are focused in brain tissue and reach intensities between 100 – 10,0000 W/cm^2 (for diagnostics < 100 W/cm^2 are used), which causes tissue damage (96, 97). HIFU is therefore also used to ablate deep-seated tumor tissue due to thermal destruction(98). Over the last years, the BBB permeabilization emerged as alternative application of HIFU for GBM treatment.

The mechanism behind HIFU-assisted BBB opening is based on microbubble oscillation. The electro-acoustic waves induce microbubbles in body fluids to oscillate, a phenomenon called cavitation (96). These cavitation forces push the bubbles against vessels, which can cause them to rupture while rapidly releasing fluids. This explosion-like release has the potential to perforate blood vessel walls of the BBB in a reversible manner (96). So far, HIFU-assisted drug delivery has

been shown successful in animal studies, delivering BBB restricted chemotherapeutics, e.g. doxorubicin (99) and trastuzumab (100).

1.2. Part II: Drug delivery utilizing organic electronic ionic pumps

Organic electronic ionic pumps (OEIPs) are drug delivery devices made from organic materials. Due to their softness, high biocompatibility and highly efficient and precise delivery of ionic molecules, these devices are favorable to use in medical applications. In my PhD work, I utilized OEIPs to deliver chemotherapeutics. Due to the structural complexity and bulkiness of chemotherapeutic drugs, the mechanisms and functionality of OEIP mediated delivery of chemo drugs needs to be closely investigated. The delivery of chemotherapeutics via OEIPs represents a pioneer work.

1.1.7. Organic (bio)electronics

Organic electronics utilize carbon-based polymeric macromolecules which can conduct both electrons and ions (101). This conductivity can be influenced and pushed by chemically doping the polymer, thereby creating electron “holes” which serve as charge carriers (p-doping) (101). These conductive polymers have therefore properties normally associated with metals, such as electrical conductivity, however, bear the mechanical advantages of polymers (as softness, bio-compatibility, wettability and modulus) (101, 102). These qualities are especially beneficial in a biological interface, and organic electronics are thus promising alternatives to inorganic electronics, especially for biomedical applications (101). One application is delivery of molecules relevant for biological signaling cascades or therapeutic drugs.

1.1.7.1. Bioelectronic drug delivery systems

Aside from OEIPs, different bioelectronic drug delivery systems are published and will be shortly described. OEIPs themselves are explained in detail in chapter 1.1.8.

1.1.1.1.1. Drug release from intrinsically conductive polymers

Intrinsically conductive polymers (ICPs) are organic polymers doped with drugs. The drug of interest is typically ionic and is incorporated into the polymer during its synthesis, where it works like a counter ion to the charged polymer (102). Once an electric field is applied to the doped ICP, the polymer undergoes reduction or oxidization, leading to repulsion of the dopant drug and release from the polymer (102), schematically shown in the following equation:

$$ICP^{+} / dopant^{-} \xrightarrow{e^{-}} ICP^{0} + dopant^{-}$$

Utilizing ICPs, different agents such as dexamethasone (103), dopamine (104) and chlorpromazine (105) have been delivered. Aside from delivery of the dopant ions, other molecules (cations and uncharged species) can diffuse through the neutralized ICP. Therefore, this method is not the most precise delivery system available.

1.1.1.1.2. Microfluidic pumps

Microfluidics utilize (polymeric) microchannels or microcapillaries for flow-driven transport of fluids (106). Their surface properties and geometries are optimized for precisely controllable flow rates and droplet formation, without putting harm to the tissue they are inserted in. In microfluidic pumps (µFIPs) the microfluidics are combined with electrophoretic drug delivery. This has been successfully used to inhibit epilepsy in rodents (107).

1.1.8. OEIPs

1.1.8.1. General description

The OEIPs used in this work are of the so-called capillary fiber OEIP type, shown in Figure 7A. These devices are miniature electrophoretic devices that consist of a source reservoir and a glass capillary (cross section in Figure 7C) filled with an ion exchange membrane (IEM, Figure 7B, chapter 1.1.8.3), which is embedded in a sealed tube and spans the seal. The liquid, placed into the source reservoir, includes an electrolyte of a highly concentrated chemotherapeutic (highlighted in pink, Figure 7A). The thin IEM-filled capillary channel is the interface with the target, in biological applications: the tissue of interest. In both, source and target electrolyte,

electrodes are placed in order to generate an electric field in which ions migrate (setup in *in vitro* experiments shown in Figure 7D).

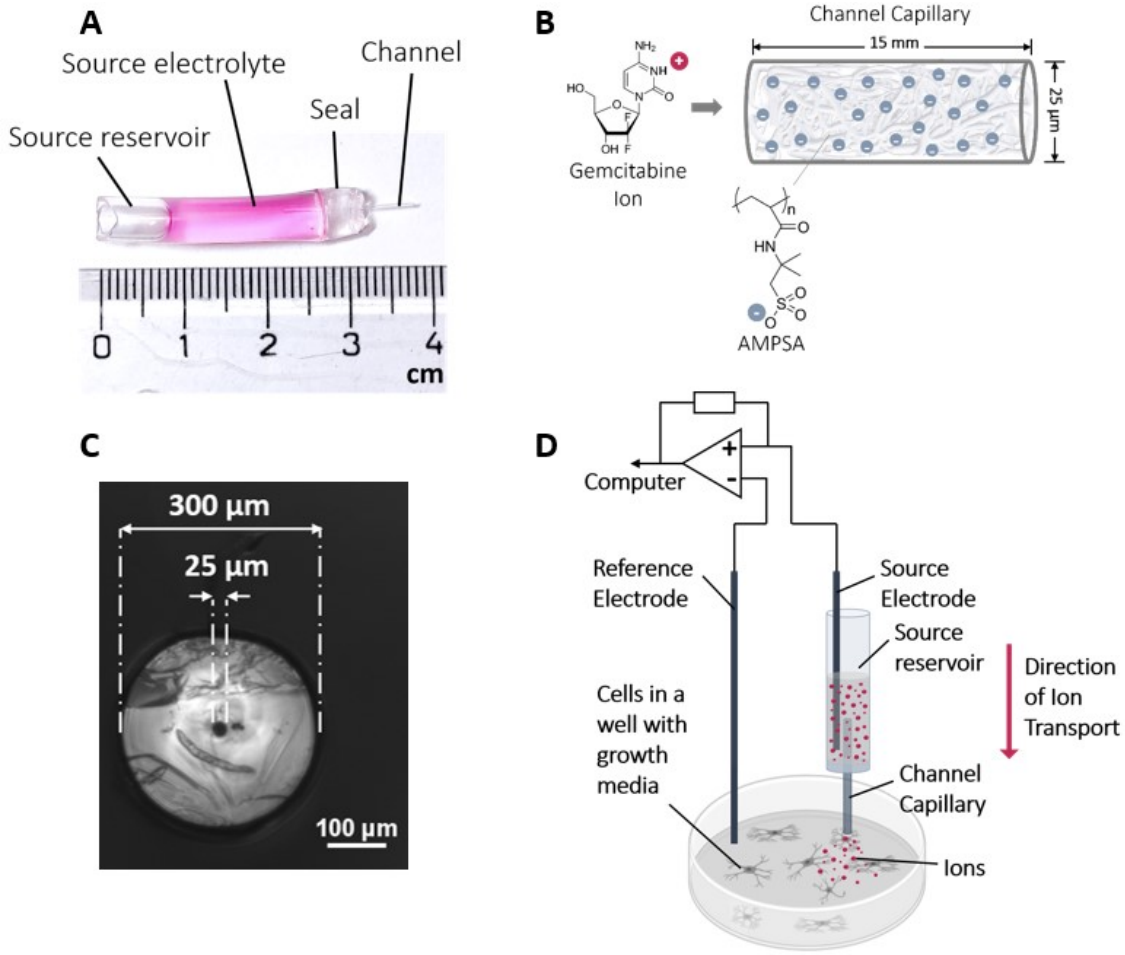

Figure 7 Demonstration of OEIPs.
A: Photograph of an actual OEIP. The source electrolyte (pink) is in the source reservoir. The channel spans the seal of the plastic tube.
B: Schematic of Gem ion transport through a channel capillary filled with a negatively charged AMPSA exchange matrix. The channel capillary has a diameter of 25 µm and a length of 15 mm.
C: Microscopic picture of cross-section of a glass channel capillary. Outer diameter = 300 µm, inner diameter = 25 µm.
D: Schematic illustration of ion pump setup in cell wells. The current is following the physical direction.

1.1.8.2. Electrophoretic ion transport

OEIP function is based on the principle of electrophoresis – the migration of charged particles towards an electrostatically attracting charged electrode within an electrical field (108, 109). The migrating ions are moving in a separation system, e.g. gels or liquids, and are separated due to different electrophoretic velocities (110).

The electrophoretic velocity (v) is proportional to the electric field (E) and the molecule's charge (q) and inversely proportional to its radius (r) , the distance between electrodes (d) and the viscosity of the solution (η) (109), and can be estimated by the following equation:

$$v = \frac{E * q}{d * 6 * \pi * r * \eta}$$

Therefore, the higher the charge of the molecule, the faster its electrophoretic velocity, while the bigger the molecule, the higher the friction and thus, slower electromigration (109). Also, the shape of the molecule and the distribution of π-electrons can influence that molecules of equal mass will show different retention behavior (109).

In general, electrophoresis is a very common separation technique, e.g. in bioanalytics the separation for proteins in sodium dodecyl sulfate polyacrylamide gel electrophoresis (SDS-PAGE), or DNA and RNA separation with agarose gels. One application similar to the capillary fiber OEIPs is capillary electrophoresis (CE). CE utilizes polyimide coated silica capillaries with an internal diameter of 25-100 µm filled with aqueous separation systems (109). As this separation is quite fast, the separation of biological samples such as DNA and serum proteins with CE is a standard analysis method in clinics (109).

1.1.8.3. The electrophoretic background in OEIPs

In OEIPs, electromigration is, above all, utilized for unidirectional release of ions of interest. In OEIPs, the separation system serves mainly as a selectivity filter, gating ions of interest and thus controllably releasing these ions to the target compartment. Electronic signals are thereby converted into directed ionic fluxes (111). This is possible due to the high density of fixed charges that are incorporated in the IEM (112). The capillary fiber (15 mm length, 25 µm internal diameter, Figure 7B, C) is either filled with anion exchange membrane (AEM) or cation exchange membrane (CEM), depending on the ionic character of the delivered species. In the context of this PhD project, two commercially available IEM materials were used for chemo ion delivery. The CEM used for transport of cationic chemotherapeutics is a polyanion of polymerized 2-

Acrylamido-2-methylpropane sulfonic acid (AMPSA) monomers. The AEM, transporting anions, is a polycation made from 2-(acryloyloxy)ethyl trimethylammonium chloride (AETMAC).

1.1.8.1. Advantages and limitations of OEIPs

One major advantage of OEIPs is the high spatio-temporal controllability of the released molecules. Therefore, within seconds, defined concentrations of biological stimulants or drugs can be reached in a confined compartment. Also, this method does not rely on flow of fluids, but is a "dry" delivery method, and therefore does not cause disturbing effects or convectional turbulences in body fluids. Also, the volume and pressure of target compartments is not influenced by OEIP mediated delivery, which is especially of interest in sensitive organs such as the brain. Due the fact that OEIPs are operated by applying an electric field, these devices are among the most precise drug delivery tools currently available.

However, one major limitation of OEIPs is that the size of transportable molecules is strictly limited, as otherwise the IEM is not transmissive. Therefore, delivery of bulky macromolecules (e.g. RNA, immunoglobulins, toxins), which are often of medical interest, is currently not possible. Another phenomenon that can occur while operating an OEIP is water splitting (112). This happens due to concentration polarization at the inlet of the capillary channel. During operation of an OEIP, in the microenvironment of the inlet the delivered molecules are depleted, while their counterions build up. Subsequently, due to the lack of deliverable ions and the applied electric field, electric-field enhanced splitting of water into OH^- and H^+ occurs. The ions then can move in the electric field through the IEM (112). This, however, can be overcome by enriching the concentration of the source electrolyte, as Seitanidou et al. have shown (112).

1.1.8.2. Currently established applications of OEIPs

Since the first publication of OEIP technology in 2007 (113), different applications have been developed for this spatio-temporally controllable delivery method. *In vivo*, it has been shown that the delivery of the neurotransmitters glutamate (Glu), aspartate (Asp) and γ-aminobutyric acid (GABA) via OEIPs could mimic a synaptic nerve and modulate mammalian sensory (114). Also, OEIP-mediated GABA delivery was successfully applied for pain decrease (115) and epileptic

seizure control (107, 116, 117). Also, OEIPs were applied to interfere with inflammation by delivering salicylic acid to monocytes (118). Aside from medical science, OEIP-mediated delivery has evolved as scientific platform to study plant physiology, delivering the plant hormones auxin and abscisic acid (119, 120).

1.3. Part III: Chemotherapeutic drugs studied in this PhD project

In order to employ OEIPs for electronically controlled chemotherapy first important steps are to (i) find drugs which could be used for the application via OEIPs, (ii) observe their GBM cell killing effectiveness and (iii) test their applicability for OEIP mediated delivery. Therefore, the molecules of interest need to be in a charged state and their molecular weight needs to be in a range between 0-300 g/mol. In the context of this project, the drugs Gemcitabine and Chlorambucil were examined, with main emphasis on Gemcitabine.

1.1.9. Gemcitabine

Gemcitabine (2', 2'-difluoro 2'deoxycytidine, sold under the brand name Gemzar® by Eli Lilly and Company, here abbreviated as Gem) is a potent chemotherapeutic agent approved for the treatment of non-small cell lung cancer, pancreatic cancer, bladder cancer and breast cancer via intravenous injection (IV) (FDA, Ref. ID: 3503046). As it can barely cross the BBB (121), its application to brain tumors via IV is less practical. A chemotherapeutic treatment approach with a new drug has the potential to circumvent resistance and to improve prognosis, especially in TMZ-resistant forms of GBM. Gem is, moreover, a very potent radio-sensitizer since it can inhibit DNA replication following treatment with ionizing radiation (122, 123).

For an electrophoretic application which bypasses the BBB, we aim to use OEIP technology to deliver Gem in the form of a “Gem Ionic Pump” (GemIP) implant. Gem is a chemical analogue of the DNA building block cytidine, and undergoes therefore the same cellular pathways and mechanisms as cytidine to get to its final site of action, the DNA. The mechanism of Gem action requires activation by triple phosphorylation following cellular uptake. Integration of activated Gem into cellular DNA causes an arrest of cell division in S-phase followed by apoptosis of both

tumorigenic and healthy cells (122, 124). Highly proliferative cells, such as cancer cells, are thus extremely sensitive to this drug.

In order to perform OEIP-mediated delivery of Gem, it has to electromigrate through the electric field. Therefore, Gem must be in a charged/ionic state. With a predicted pKa of the nitrogen in the pyrimidine ring of 3.65 (Figure 8A, Chemicalize was used for pH prediction, March 2019, https://chemicalize.com/, developed by ChemAxon), the molecule is expected to be in a protonated and single positively charged state below this pH. Accordingly, it is predicted that 30 % of Gem molecules will be found in a protonated state, i.e. Gem:H^+ at pH 4 (Figure 8B, Gem^+ curve in yellow) (125, 126). This and the molecular weight (ca. 263 g/mol) of the molecule indicate that the Gem is a promising candidate for functional OEIP mediated delivery with an CEM (e.g. polyAMPSA).

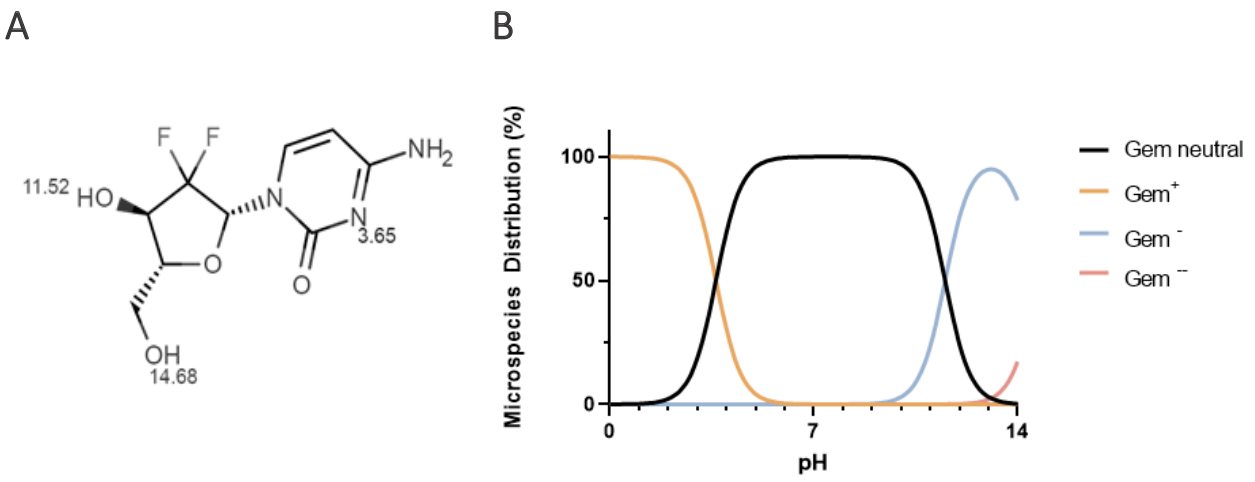

Figure 8 Gemcitabine and its protonation behaviour.
A: Chemical structure and predicted pKa values of Gem.
B: Distribution of micro species for differently protonated forms of the Gem molecule. The predicted curves in % of distribution (commercially available ChemAxon software: chemicalize.com) shows in red: the single positively charged ionic form of Gem, in blue: the neutral molecule, in yellow: the single negatively charged molecule (deprotonation of hydroxide pKa 11.52) and in green: the double negatively charged molecule (deprotonation of both hydroxides).
Chemicalize was used for pH prediction, March 2019, https://chemicalize.com/, developed by ChemAxon,

1.1.10. Chlorambucil

The chemotherapeutic drug Chlorambucil (CLB) (Figure 9A) occurs as another possible candidate for OEIP mediated delivery. The compound is usually used as a standard treatment for leukemia, has a molecular weight of 304 g/mol and carries a single negative charge at physiological pH. Since this drug is negatively charged, an AEM membrane is needed for OEIP mediated delivery (e.g. polyAETMAC).

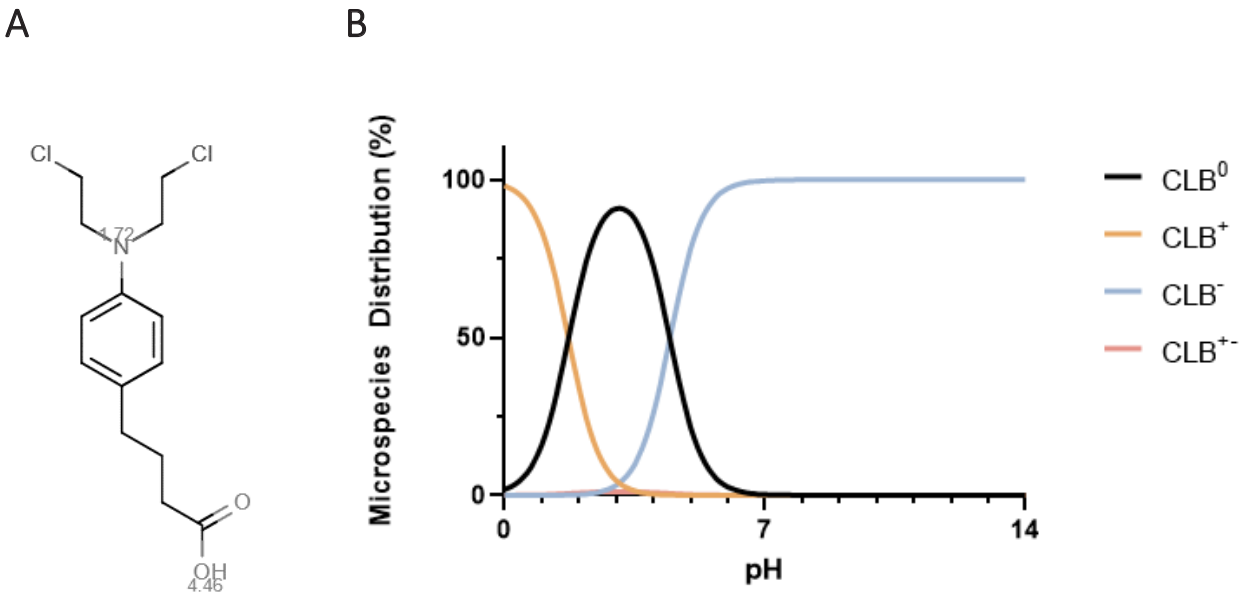

Figure 9 Chlorambucil and its protonation behaviour.
A: molecular structure of CLB. The acidic pKa of the carboxylic acid is 4.46.
B: Distribution of micro species for differently protonated forms of the CLB molecule. The predicted curves in % of distribution (commercially available ChemAxon software: chemicalize.com) shows in red: the single positively charged ionic form of CLB (protonation of nitrogen at pKa 1.72), in blue: the neutral molecule, in yellow: the single negatively charged molecule (deprotonation of hydroxide pKa 4.46) and in green: the netto neutral molecule (deprotonation of hydroxyl group, protonation of nitrogen).
Chemicalize was used for pH prediction, March 2019, https://chemicalize.com/, developed by ChemAxon,

2. Hypothesis and Aims/Aims and Objectives

2.1. Treatment of GBM with Gemcitabine Ionic Pumps

In this project, we establish bioelectronic chemotherapeutic delivery via ionic pumps for the treatment of tumors in the brain. Unlike other delivery methods, OEIP technology does not rely on a flux of fluids – only ions migrate, allowing "dry" chemotherapeutic delivery, without further disruption of the fragile biochemical environment at the delivery outlet. Due to this, we consider OEIP mediated drug delivery the ideal method to deliver BBB restricted, potent chemotherapeutics directly to GBM tumors and to improve the GBM treatment and OS rates on a long term.

The aims of my PhD project are therefore

- To establish an OEIP operation laboratory at the Gottfried Schatz Research Center at the Medical University of Graz
- To proof the principle of OEIP mediated delivery for the chemotherapeutic Gem
- To characterize OEIP mediated Gem delivery (determination of delivery rates and efficiency)
- To evaluate GemIP safety as operation *in vitro*
- To use GemIPs for the treatment of GBM cell monolayers and microtumors

Delivery of chemotherapeutic drugs for the treatment of cancer has, to date, not been explored, making the proposed project, to the best of our knowledge, a pioneering application of OEIP technology.

3. Materials and Methods

3.1. Manufacturing of in-house source measure units (SMUs)

SMUs were developed and manufactured by Meysam Karami Rad (Linköping University) and manufactured by Kurt Feichtinger (Medical University of Graz). The in-house produced SMUs serve as alternative to commercially available sourcemeters, e.g. provided by Keithley Tektronix, USA. These Arduino-based devices are an attractive low-cost option to operate OEIPs and were used exclusively to operate OEIPs in this work.

3.2. OEIP fabrication

The fabrication of OEIP devices was performed by Maria Seitanidou and Marie Jakešová.

The fabrication steps are described in detail in the PhD thesis " Overcoming Limitations of Iontronic Delivery Devices" of Maria Seitanidou (127).

Shortly summarized, the CEM was prepared by mixing AMPSA monomers with polyethylene glycol diacrylate (PEG-DA) and a photoinitiator (2-hydroxy-4'-(2-hydroxyethoxy)-2-methyl-propiophenone). The glass capillaries (Polymicro Technologies, 15 µM internal diameter, 125-300 µM external diameter) were used both as uncoated fibers and as polyimide coated fibers (batch dependent). Fibers were rinsed with DI H_2O and one end a syringe adapter was assembled. With syringes, 2 M KOH was flushed through the capillaries to activate the OH-groups of the inner silica surface, followed by salinization with 3-(trimethoxysilyl) propyl methacrylate (3-TSA). This step causes reaction of the silanizing agent with the silanol groups, making the surface hydrophobic due to presented methacrylic groups. The CEM material (AMPSA mixture) is flushed into the capillary and photopolymerized. Finally, the capillary fiber is cut into 15 mm long pieces and assembled in heat-shrink tubes using hot tweezers.

3.3. Compounds

Temozolomide (TMZ) was obtained from Merck Millipore, USA and stored as powder at 4 °C and dissolved in corresponding media immediately before use. Gemcitabine and Cytidine were obtained from Merck Millipore, USA and stored as 100 mM aqueous stock at -20°C until use. CLB

was obtained from Merck Millipore, USA, and was diluted in 96 % EtOH at 100 mM and stored at -80°C. Staurosporin was used form Merck Millipore, USA and stored as 1 mM stock in DMSO at -20°C until use. Digitonin (Merck Millipore, USA) was dissolved in water at 5 mg/mL and diluted to working concentration of 50 µg/mL immediately before use.

3.1. Detection of Gem via UV Absorption

As reported, the Gem concentration was detected via UV absorption of the molecule at 267 nm (128). To verify this, the absorption spectrum of Gem was determined with a CLARIOstar plate reader (BMG Labtech, Germany) over a spectral range of 220-400 nm. The target concentration itself was determined at a NanoDrop Microvolume Spectrophotometer (Thermo Fisher Scientific, USA).

3.2. Determination of delivery rates

OEIPs were assembled in an Eppendorf tube with a reservoir of 50 µL deionized water. The OEIP source contained 100 mM Gem adjusted to pH 4 with 0.0001 M HCl. Utilized electrodes were PET sheets covered with PEDOT:PSS and optional AgCl coating to increase the capacity and carbon coating for better contacts were placed in the target and source. OEIP channels were filled with Gem at constant 0.5 V for 2 h. Afterwards, target solutions were replaced with fresh water and OEIPs were run at 10, 20 or 0 nA for 8 h. The concentration of Gem in the target was detected with a NanoDrop (Thermo Fisher Scientific, USA) at 267 nm. The delivery rate was calculated by multiplying the measured Gem concentration [pmol/L] with the target volume [L] and divided by the time of delivery [min].

3.3. Gem stability

To determine the stability of Gem over three weeks, for each time point, samples of 50 µM Gem with adjusted pH were prepared. The samples were stored in an incubator (37°C, 5% CO_2) for up to three weeks, samples were taken and measured after 0, 7, 14 and 21 days and the concentration was determined via NanoDrop (Thermo Fisher Scientific, USA).

3.4. Cultivation of cells

In view of the marked genetic heterogeneity of GBM, we selected a panel of four GBM cell lines with different levels of MGMT expression and variable *p53* mutation status. The chosen cell lines are described in Table 1.

Cell Line (ATCC No.)	Cell Type	TMZ sensitivity	MGMT expression	p53
U-87 MG (ATCC HTB-14)	Human	high(129)	low(130, 131)	wild-type(132)
A172 (ATCC CRL-1620)	Human, GBM	high(133)	null (131)	wild-type(132)
U-251 MG	Human, GBM	high(50)	null(131)	mutant(134)
LN-18 (ATCC CRL-2610)	Human, GBM grade IV	low(129)	high(135, 136)	mutant(134)

Table 1 Characteristics of the glioma cell lines.

U-87 MG cells were cultivated in E-MEM supplemented with 2 mM L-glutamine, 1 mM sodium pyruvate, 0.1 mM non-essential amino acids (NEAA) and 10 % fetal bovine serum (FBS). U-251 MG were cultivated in D-MEM supplemented with 2 mM L-Glutamine and 10 % FBS. All media and supplements were obtained from Thermo Fisher Scientific, USA. In order to form spheroids, U-251 MG cells were seeded at a density of 10.000 cells/well into round-bottomed ultra-low attachment plates (Corning, USA) and further proceeded after 30 h sphere formation.

U-87 MG cells were cultivated in E-MEM media supplemented with 2 mM L-glutamine, 1 mM sodium pyruvate, 0.1 mM non-essential amino acids (NEAA) and 10 % fetal bovine serum (FBS). U-251 MG were cultivated in D-MEM media supplemented with 2 mM L-Glutamine and 10 % FBS. All media and supplements were obtained from Thermo Fisher Scientific, USA. Primary neurons and astrocytes were obtained freshly from rat brain. Briefly, rats at postnatal day 0-1 will be sacrificed by decapitation; 4 cortical hemispheres out of 2 pups will be quickly removed, washed with phosphate buffer, crosswise chopped in 100 µm squares (McIlwain Tissue Chopper) and transferred to 1 ml Accutase for 20 min at 37°C. Enzymatic digestion will be stopped by adding serum-containing medium. Suspension will be filtered through a 0.4 µm cell strainer and

centrifuged for 5 min at 300 g. For cultivation of neurons, cells will be re-suspended with the cultivation medium (Neurobasal A Medium supplemented with 1 % B27, 0.5 mM GlutMAX (all Thermo Fisher Scientific), 5 ng/mL ß-FGF and 20 ng/mL EGF (both PrePro Tech)). After 4 initial days ßFGF concentration was increased to 10 ng/mL. Astrocytes were cultivated in D-MEM supplemented with 20 % FBS, 2 mM GlutaMAXX (all Thermo Fisher Scientific, USA), 1 mM sodium pyruvate (Merck Millipore, USA) and 0.2 % normocin (Invivogen, France).

3.5. IC_{50} curves of Gem, TMZ and CLB

IC_{50} curves were obtained by seeding U-87 MG at a density of 4000 cells/well and U-251 at a density of 1500 cells/well. After settling, cells were treated for 72 h with a range of freshly prepared TMZ solutions (0, 50, 100, 500, 1000, 2000, 5000, 7000, 10000, 12500, 15000, 20000), Gem solutions (0.0001, 0.001, 0.01, 0.1, 1, 5, 10, 50, 100, 500, 700, 1000, 2000, 5000, 7000, 10000 µM) and CLB solutions (0.1, 1, 10, 50, 100, 200, 300, 400, 500, 600, 800, 1000, 5000 µM). Cell viability was analyzed after 72 h incubation by performing a CellTiter 96® AQueous One Solution Cell Proliferation Assay (MTS) (Promega, Germany) according to manufacturer's protocol. Results were read out on a CLARIOstar platereader (BMG Labtech, Germany) at 490 nm. Sigmoidal curve fit was done with Prism 8 software (GraphPad, USA) by using a variable slope with four parameters and the following equation: Y = Bottom + (Top-Bottom)/(1+(IC50/X)^HillSlope).

3.6. Real-time monitoring of apoptosis and necrosis

To monitor apoptosis and necrosis, a Real RealTime-Glo™ Annexin V Apoptosis and Necrosis Assay (Promega, Germany) was performed. U-87 MG cells (4000 cells/well) were seeded into flat-bottomed black-walled 96-well plates (Corning, USA). After settling, cells were treated with a final concentration of 1 µM staurosporin (positive apoptosis control), 50 µg/mL digitonin (positive necrosis control) and Gem (0.1, 1, 10 µM). The 2X Detection Reagent was prepared according to manufacturer's protocol and added to the cells as well. Readout of luminescence (annexin V) and fluorescence (at 485 nm excitation/520–30 nm emission, necrosis) was performed on a CLARIOstar platereader (BMG Labtech, Germany).

3.7. Determination of growth

To observe cell growth under presence of 1 mM Gemcitabine, cells were seeded in flat-bottomed black-walled 96-well plates (Corning, USA) at a density of 8000 cells/well (U-87 MG) and 4000 cells/well (U-251 MG). After settling, cells were treated with 1 mM Gemcitabine and untreated controls were carried out in parallel. Analysis was performed after 0, 24, 48 and 72 h by performing a Hoechst stain (6 µg/mL Hoechst 33258 in PBS, incubation for 10 min/room temperature/dark), followed by two wash steps with PBS. Results were read out on a CLARIOstar platereader (BMG Labtech, Germany) at 350 nm excitation/455 nm emission.

3.8. GemIP operation on U-87 MG monolayers *in vitro*

To observe effects on GBM cells, U-87 MG were seeded at a density of 4000 cells/well in 250 µL media in 96 well plates. To fill the channels, OEIPs were installed as described as in "Determination of Delivery Rates for Gem". OEIP channels were pre-filled with Gem or Cytidine (Cyt) at constant 0.5 V for 2 h. After settling of the cells, OEIPs with Gemcitabine-filled channels were mounted on the wells, with the channels immersing into the cell media but without contacting the monolayer of cells at the well bottom. As electrodes, Orgacon electrodes without AgCl paste were used. The source reservoir consisted of 100 mM Gem adjusted to pH 4 (0.0001 M HCl). Additionally, the OEIPs with source filled with 100 mM Cyt at pH 4 (0.0001 M HCl) were mounted identically as those with Gem. After operation for certain time periods, OEIPs were dismounted and cells were incubated for 72 h to observe the effects of treatment microscopically at 4X magnification (Olympus IX70 microscope equipped with camera model 34.0) and VisiView Software (Visitron, Germany) and cell viability was measured (procedure described in 3.5).

3.9. GemIP operation on U-251 MG spheroids *in vitro*

U-251 MG cells were seeded at 10,000 cells/well in round-bottom microplates with ultra-low attachment surface (Corning, USA) and cultivated for 30 h to assure formation of spheroids. Afterwards, OEIPs were installed as described in chapter 3.8 and were operated for 24 h at 10 nA. After OEIP mediated treatment, OEIPs were dismounted and spheroids were incubated for

further 48 h (followed by flow cytometric analysis of cell death, see chapter 3.11) or 96 h (microscopy). For visualization of spheroid disassembly, microscopic pictures of spheroids were taken at 4X magnification on an Olympus IX70 microscope (Diagnostic Instruments Inc., USA) with camera model 34.0 and VisiView Software (Visitron, Germany). The dense spheroid area was analyzed via IMARIS picture detection software (Oxford Instruments, UK).

3.10. Mass spectrometric determination of Gem concentration after 24 h

Chromatographic separation was carried out on a Dionex UltiMate 3000 system equipped with a Zorbax SB-C18 column (50 mm x 4.6 mm, 1.8 µm, Agilent, USA) with a flow rate of 0.3 mL/min (solvent A: 0.1 % formic acid in water; solvent B: 0.1 % formic acid in acetonitrile). Injection volume was 2 µL and the following gradient was applied: 0-10 min: 1% B - 30% B; 10-13 min: 1% B. Chromatography was coupled to a TSQ mass spectrometer (Thermo Fisher Scientific, USA) operated with electrospray ionization source in positive mode. Selected reaction monitoring mode was enabled with a parent mass of 264.100 Da for Gem and fragment masses of 94.980 Da and 112.000 Da. Peak integration and analysis was performed using Thermo Xcalibur Quan Browser (version 3.0.63).

3.11. Analysis of apoptosis in spheroids using flow cytometry

Detection of apoptosis in spheroids was performed by utilizing a FITC Annexin V Apoptosis Detection Kit I (BD Biosciences, USA) following the manufacturer's protocol. Measurements were performed on a CytoFLEX (Beckmann Coulter, USA), the acquisition is terminated after 10,000 cell counts and follow-up data analysis is performed with CytoFLEX analysis software (Beckmann Coulter, USA).

4. Results

4.1. Channel filling and constant delivery of Gem with OEIPs

In order to establish constant delivery of molecules, the IEM of OEIP channels need to be filled/loaded with the molecules of interest. Therefore, a so-called "channel-filling protocol" is conducted, in which small cations from buffer solutions (e.g. K^+, Na^+, Ca^{2+}, Mg^{2+}), that are initially present in the IEM, are replaced by the chemotherapeutic cations due to their migration in the electric field. A theoretical current trace profile of this channel-filling process is shown in Figure 10. While a constant voltage is applied and the source consists of a saline buffer (e.g. 10 mM KCl), a stable current is recorded (Figure 10, phase I). After exchanging the buffer with a solution containing sterically more demanding and bulkier molecules (e.g. 100 mM Gem at pH 4), the electromigration of these bulky molecules through the IEM results in an increase of resistance of the channel, and therefore a decrease of the recorded current (Figure 10, phase II). Phase II is therefore considered as a filling/exchange phase, in which both molecules from the previous and the new source are present and migrate through the IEM matrix. Once the current stabilizes again (phase III, Figure 10), it is assumed that mainly drug molecules of the new source are present in the IEM and a constant drug delivery is supposedly established.

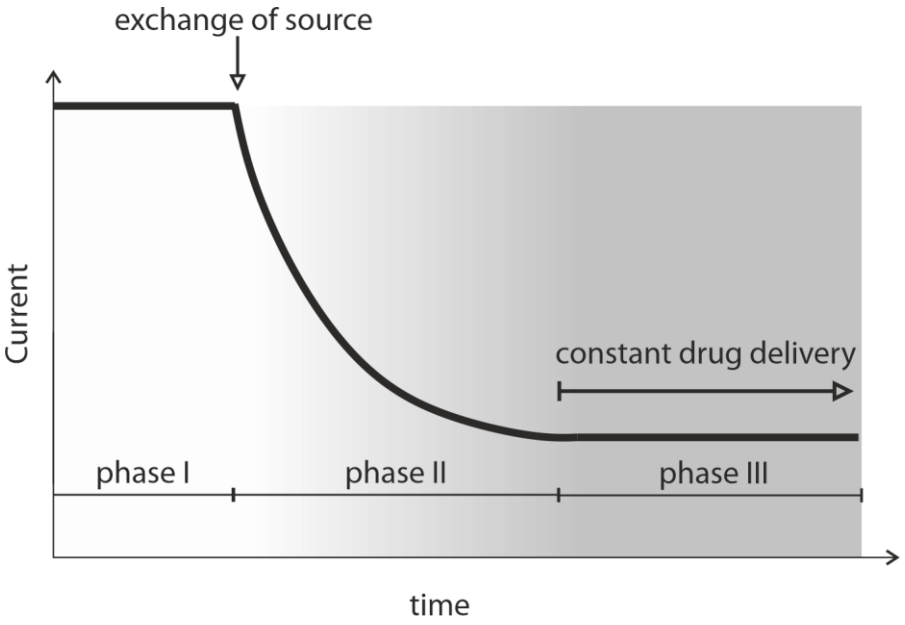

Figure 10 Theoretical current trace profile.
The current trace shows the typical recorded current when a source electrolyte is exchanged for a source containing molecules with higher molecular weight than the previous electrolyte at constant voltage.

A representative current profile trace of the realistic channel filling process of a GemIP is shown in Figure 11. In contrast to the theoretical current trace (Figure 10), phase I was here omitted. The device was filled with a source consisting of 100 mM Gem at pH 4 while 0.5 V were constantly applied. Two major observations can be made based on this profile trace, (a) the phase II decay, in which the exchange of cations in the IEM occurs, is observed within the first six hours of operation, and (b) although the decay becomes less steep at around 10 nA (device-dependent), the recorded current does not stabilize, even after 24 h of operation. We observed this behavior in all OEIP devices filled with Gem, and concluded that the ongoing phenomenon is based on “clogging” of the IEM with Gem molecules. “Clogging” means, that due to the molecular interactions and steric hindrance of Gem in the IEM, there is a build-up of Gem, resulting increased resistance and reduced ion conduction. These effects will be further characterized and discussed in the following chapters.

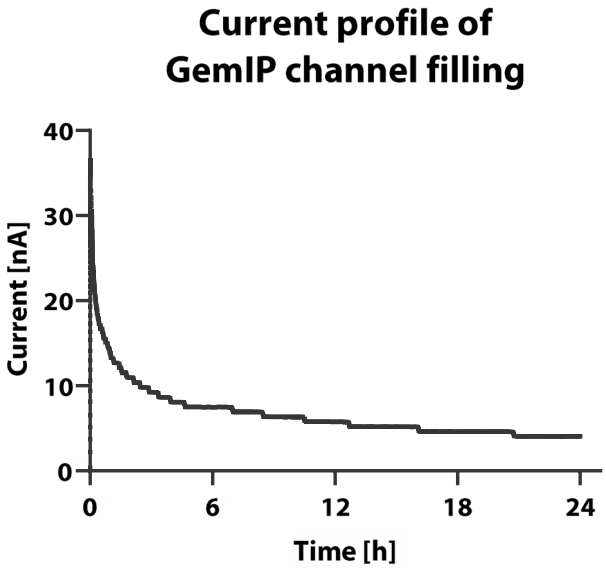

Figure 11 Realistic channel filling trace for GemIPs.
GemIP was operated with a source consisting of 100 mM Gem at pH 4, while applying 0.5 V constantly for 24 h.

4.2. Determination of delivery rates

Based on this current profile trace, the next aim was to determine whether Gem can be detected in the target electrolyte, and consequently to calculate the delivery rates at different addressing modes. Therefore, an absorption spectrum of Gem (500 µM) was detected via UV absorbance, resulting in maximum absorbance at 267 nm (Figure 12, left), as already reported by Singh et al., 2015 (128). The linear range of Gem UV detection is between 2.5-500 µM, shown in Figure 12, right.

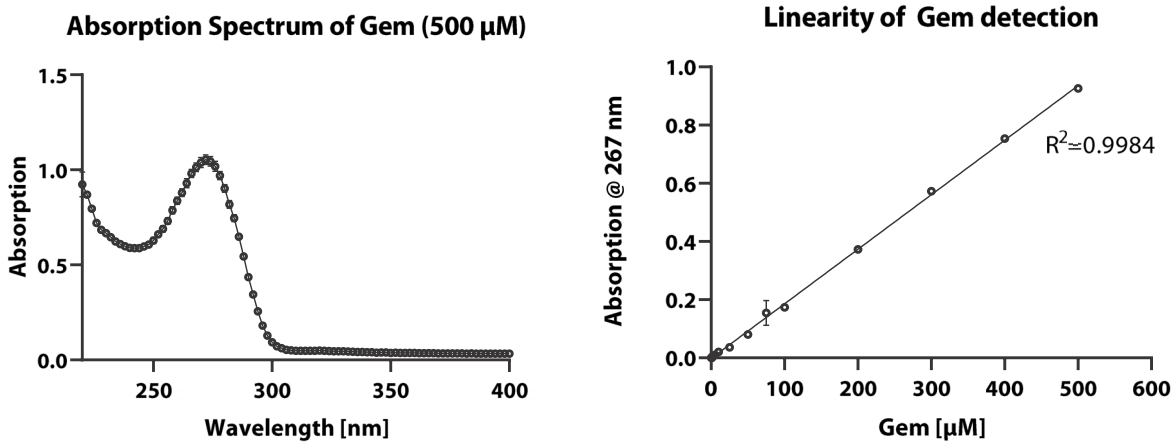

Figure 12 Absorption characteristics of Gem.
Left: Spectrum of absorbance of aqueous Gem solution (500 µM), recorded from 220-400 nm. Right: Linear range of Gem detection via UV absorption at 267 nm.

Accordingly, GemIPs were installed with a source of 100 mM Gem, pH 4 and a target solution of 30 µL dH_2O. The GemIPs were operated for 8 h at 10, 20 nA (active delivery) or 0 nA (for determination of passive delivery). Afterwards, the Gem concentration in the target was determined via UV absorbance at 267 nm and the delivery rates were calculated based on the following equation:

$$Delivery\ rate\ \left[\frac{mol}{s}\right] = \frac{Gem\ concentration\ \left[\frac{mol}{L}\right] * target\ volume\ [L]}{time\ of\ delivery\ [s]}$$

The measured delivery rates were 1.54 ± 0.68 pmol/min at 10 nA, 1.55 ± 0.73 pmol/min at 20 nA and 0.16 ± 0.10 pmol/min at 0 nA, plotted in Figure 13. These results indicate that the delivery of Gem via OEIPs is indeed possible and that the application of an electric field is essential to generate delivery rates that are relevant for physiological applications. It also showed that GemIP operation at 10 and 20 nA results wide spreading of values, and that the difference of mean delivery rates is not significantly increased when the current is increased from 10 to 20 nA.

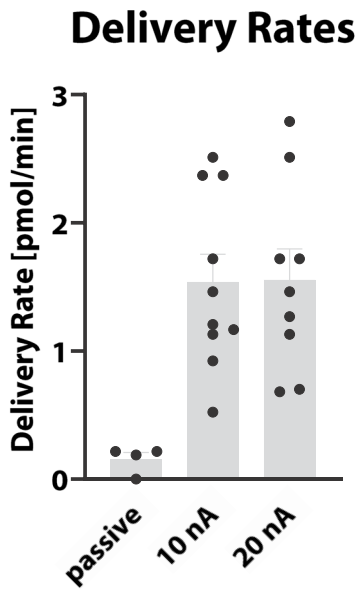

Figure 13 Comparison of delivery rates of GemIPs.
GemIPs were differently addressed (0, 10 and 20 nA). Results shown as mean ± SEM of four different GemIP devices, operated at least twice with each addressing.

We hypothesize that this is due to the already mentioned clogging of the IEM with Gem ions. To our current knowledge we assume that Gem cannot migrate without restrictions through the IEM due to a) π-π-electron interactions between Gem and AMPSA molecules, and b) steric hindrance of the spacious Gem molecule in the closely linked IEM matrix.

4.3. Mass Spectrometric analysis of GemIP performance

In order to evaluate the general range of performance of GemIPs, we utilized 20 different GemIPs from one batch and operated them for 24 h at 10 nA. Two different concentrations were calculated, the predicted concentration, which is calculated based on the current that was applied (grey in Figure 14) and the realistic concentration, calculated based on linear fitting of mass spectrometric measurements of all 20 GemIP devices (red in Figure 14). From this comparison, we could see that the efficiency of delivery is below 1%, which is presumably due to the mentioned clogging and due to the fact that Gem is a spacious molecule. Also, it becomes visible that the realistic measured concentrations vary strongly between devices.

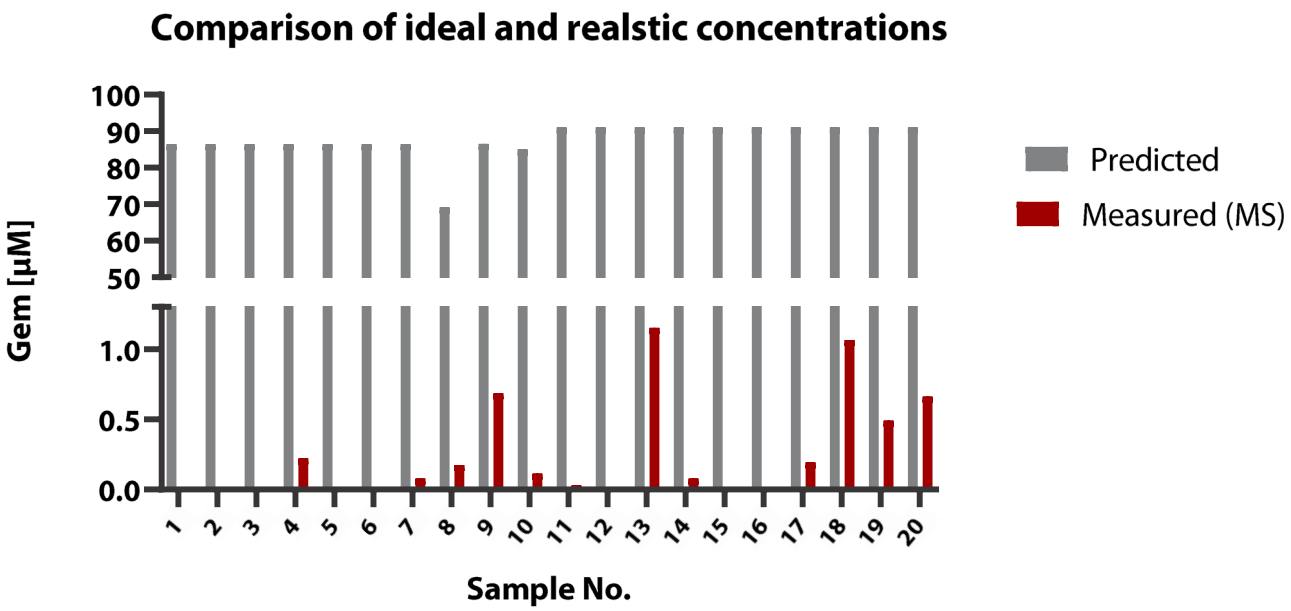

Figure 14 Comparison of delivered [Gem].
Twenty GemIP devices were operated for 24 h at 10 nA. Concentration in the target was determined via MS measurements.

We also observed the performance of single GemIP devices operated for total 48 h, in order to show that the operation time has direct influence on delivery rates. Therefore, we operated six GemIPs at 10 nA for 24 h and measured the Gem concentration in the target (observation 1, Figure 15). The procedure was repeated directly afterwards (observation 2, Figure 15), and results in lowered final concentrations for all measured devices.

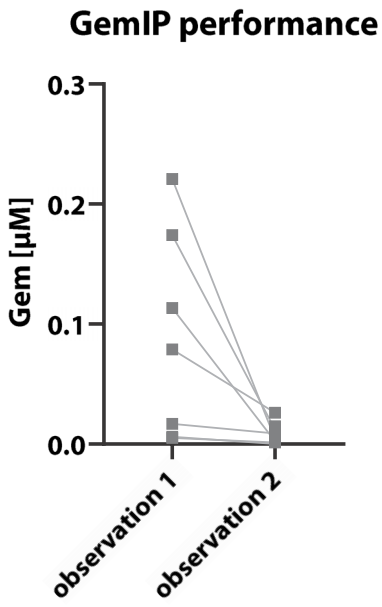

Figure 15 Performance of GemIPs over total 48 h.
Delivered Gem concentration delivered by GemIPs (n=6) was detected after two subsequent operation sessions with 24 h each. Samples were drawn after 24 h (observation 1) and 48 h (observation 2) of continuous GemIP operation at 10 nA. For all devices, decreased delivery of Gem occurs after the first 24 h operation session.

In parallel, the voltage, which was detected during the constant current operation mode of GemIP measurements, continuously increased (representative voltage profile shown in Figure 16). This resembles again the clogging complications that occur during constant operation. The voltage increases as the resistance increases.

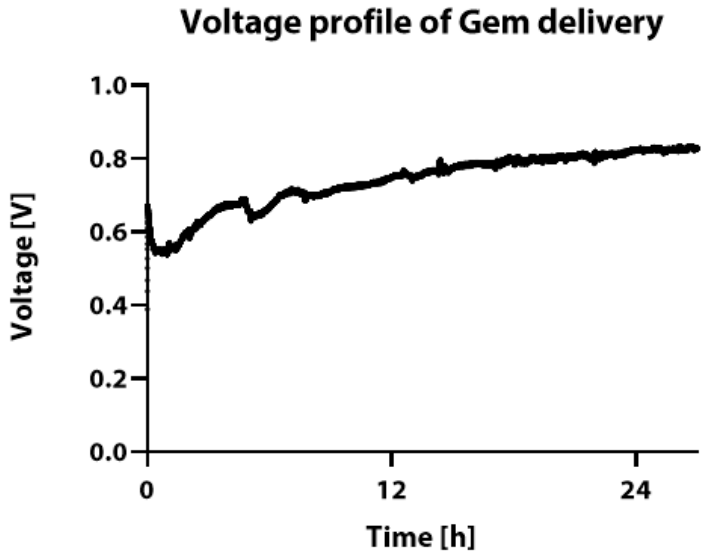

Figure 16 Voltage trace of GemIP operated at 10 nA constantly.
The increase in resistance becomes evident by the constant increase in the recorded voltage at constantly applied 10 nA.

These results sum up that the OEIP mediated Gem delivery is a) functional, b) controllable via the applied electric field and c) clogging occurs to an extent that is still tolerable for our first *in vitro* experiments, but needs to be improved in further generations of GemIPs.

4.4. Gem stability

The long-term aim of this project is the development of a GemIP based brain implant, which has a source reservoir body in which Gem will be stored in its protonated state at acidic pH values. We therefore considered the evaluation of Gem at low pH values as important parameter to proceed with this drug in further experiments. Gem solutions (100 µM) were acidified to pH 3 and stored at 37°C for three weeks. After each week, the concentration of the samples was measured via UV absorbance at 267 nm and normalized to the absorbance of 100 µM Gem.

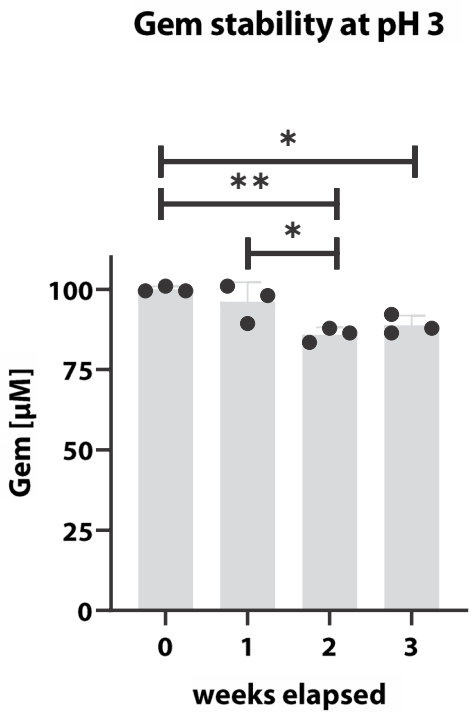

Figure 17 Stability of Gem at acidic pH of 3 over three weeks.
Results are shown as mean ± SEM, n=3 from one single experiment, one-way ANOVA, *: p-value < 0.1, **:p-value <0.01.

The concentration decreased significantly, but slightly by ca. 10% % over three weeks, with a concentration of 96 ± 6 µM after the first week, 85 ± 2 µM after the second, and 89 ± 3 µM after the third week, shown in Figure 17. We considered the extend of Gem degradation acceptable for our planned purposes, and therefore, continued with the evaluation of Gem as agent for GBM treatment.

4.5. Gem as potent chemo agent for treatment of GBM

First of all, we observed the major pathway through which Gem induces cell death in the GBM cell line U-87 MG. We therefore performed an apoptosis and necrosis assay, which measures on one hand the apoptosis via a luminescent reaction, and on the other hand the necrotic cell death via fluorescence. For detection of apoptosis, the lipid asymmetry including the presence of phosphatidyl serine (PS) in the outer membrane leaflet is utilized as indicator of this cellular process. In healthy cells, the bipolar membrane building block PS is only represented in the inner

leaflet of the lipid bilayer of the cell membrane. Only when cells become apoptotic, PS flips to the outer leaflet (137). The protein annexin V has high affinity for PS, and binds to it once it is present at the outer leaflet. This reaction was used for detection, utilizing two labeled subunits of annexin V which produce a luminescent signal once they bind to PS and each other. In contrast to this, the detection of necrosis relies on the accessibility of DNA, which occurs when the cell membrane ruptures, a hallmark of necrosis. The fluorescent DNA dye used for detection of necrosis can then enter the cell and intercalate in the DNA, resulting in a fluorescent readout. In the performed tests, we compared three Gem concentrations (0.1, 1 and 10 µM) with the signals induced by the well-established apoptosis inducer staurosporin (1 µM) and the necrosis-inducer digitonin (50 µg/mL) over 72 h, shown in Figure 18.

In Figure 18A, the maximum of apoptotic signals induced by different compounds and concentrations is shown. Both 1 and 10 µM Gem significantly induced apoptosis, comparable to the signal of the positive apoptosis control staurosporin. The lowest Gem concentration (0.01 µM) did not significantly induce apoptosis and was comparable to the signals of the growth control and digitonin (50 µg/mL). In Figure 18B, the time course of the induced effects is shown. For staurosporin (1 µM), the maximum apoptosis signal is already reached after 24 h, while for 1 and 10 µM Gem the maximum is reached after 48 h.

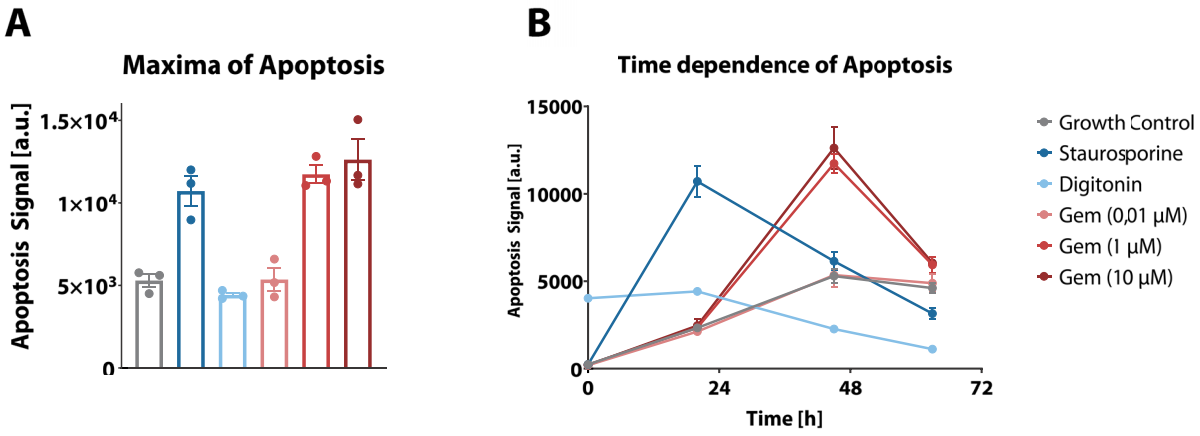

Figure 18 Cell death pathways caused by Gem treatment in U-87 MG cells.
A: Maxima of Apoptosis.
B: Time course of apoptosis. Treatment with staurosporin (1 µM, positive apoptosis control), digitonin (50 µg/mL, positive necrosis control), Gem (0.01, 1, 10 µM) or no treatment (growth control). Results are shown as mean ± SEM, n=3, single experiment.

Analysis of induced necrosis showed that the major pathway of cell death induced by Gem is clearly apoptosis. The signal maxima of fluorescent signal remained low for all three tested concentrations, and in comparison the positive control digitonin tremendously lower, even lower than staurosporin samples (Figure 19A). The time course (Figure 19B) shows that over the whole time, the necrotic signal increased slightly in staurosporin and 1/10 µM Gem, however, to an extent we evaluate irrelevant.

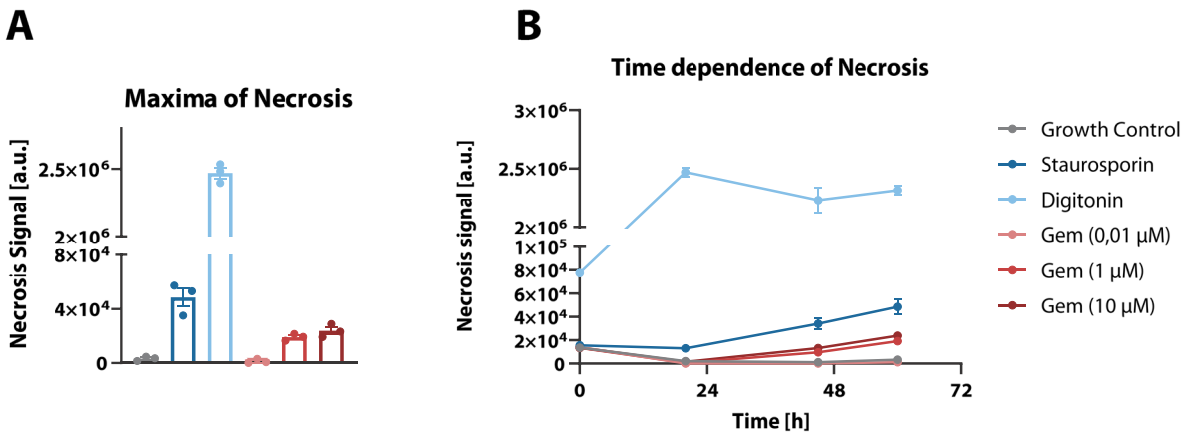

Figure 19 Cell death pathways caused by Gem treatment in U-87 MG cells.
A: Maxima of necrosis. B: Time course of necrosis. Treatment with staurosporin (1 µM, positive apoptosis control), digitonin (50 µg/mL, positive necrosis control), Gem (0.01, 1, 10 µM) or no treatment (growth control). Results are shown as mean ± SEM, n=3, single experiment.

We next determined the effect of Gem on cell growth, by performing staining of nuclei with Hoechst dye (Figure 20). U-87 MG (Figure 20, blue) and U-251 MG (Figure 20, red) cells were therefore treated with 1 mM Gem for up to 72 h, controls remained untreated. This data shows that Gem has the potential to inhibit cell growth of these cells completely, even to an extent that cell number is reduced over 72 h.

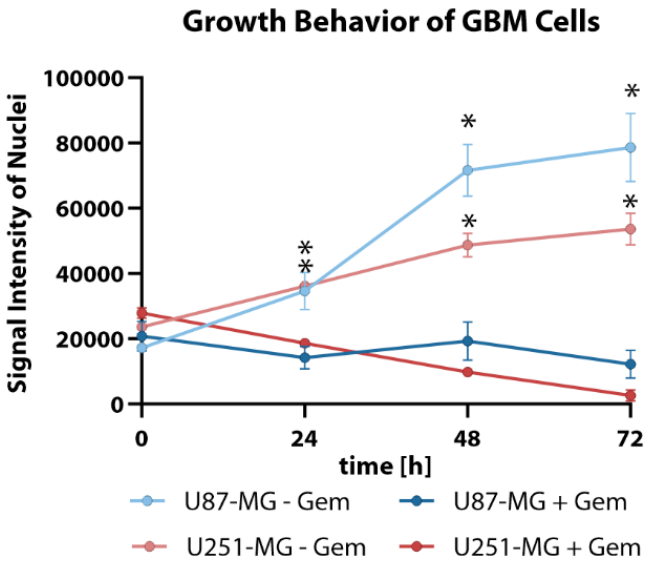

Figure 20 Growth behavior of GBM cells after treatment with 1 mM Gem.
U-87 MG and U-251 MG cells were treated with 1 mM Gem for up to 72 h. Results are shown as mean ± SEM from a single representative experiment, n=3, two-sided t-test, *: p-value < 0.1.

This is an essential quality of a chemotherapeutic. Since GBM can double its volume within 50 days, the explosive growth of these cells needs first and foremost to be stopped. These results show that Gem indeed has the potency to do so, and to therefore, generates a time window for therapeutic measures while keeping the cell growth contained.

In the next step we determined IC_{50} values for Gem and TMZ. There are some few reported IC_{50} values for Gem in GBM cell lines (134), and a plethora of IC_{50} values for TMZ in GBM, of course. However, TMZ IC_{50} values vary between the low micromolar to the millimolar range (50), most probably due to the high mutagenic potential of GBM cell lines and different treatment protocols. We therefore considered it essential to establish IC_{50} curves for the cell lines we utilized throughout this project, and compared them with IC_{50}ies for healthy brain cells such as neurons and astrocytes (Figure 21).

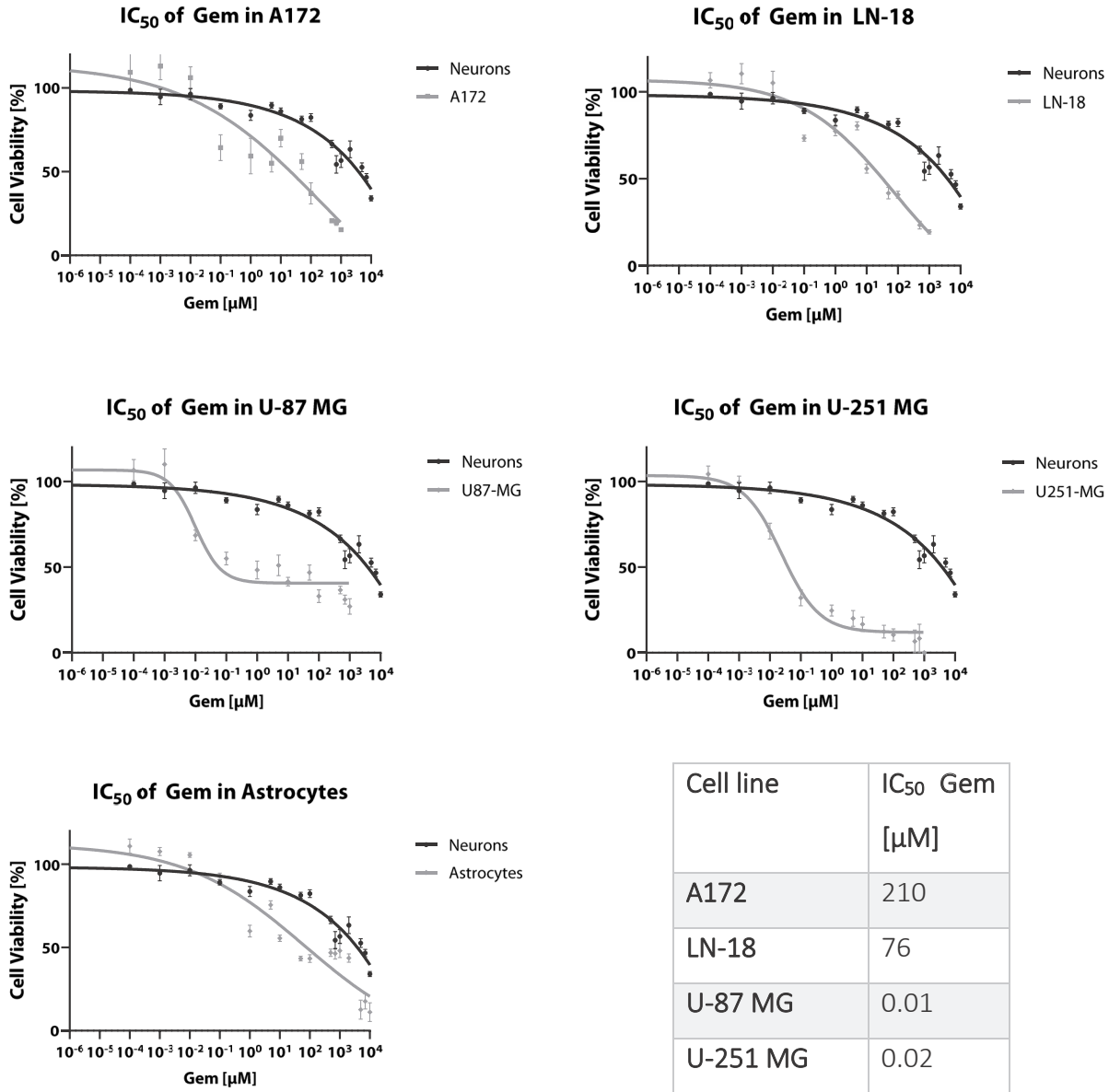

Cell line	IC_{50} Gem [µM]
A172	210
LN-18	76
U-87 MG	0.01
U-251 MG	0.02
Astrocytes	66
Neurons	ca. 10000

Figure 21 IC_{50} values of Gem after 72 h treatment in GBM cell lines, astrocytes and neurons.
The values are plotted in comparison to neuronal toxicity caused by Gem, in order to visualize the therapeutic window. All values shown as mean ± SEM, data from at least two independent experiments, n ≥ 6.

These resulting IC_{50} curves for each GBM cell line are shown in comparison to the IC_{50} in neurons. This was done to visualize the huge differences of effects on cell viability in malignant and healthy brain cells caused by Gem. As expected, neurons react to Gem only at high concentrations, and have an IC_{50} above 10 mM. This is owed to the mechanism of action of Gem, which incorporates into the DNA and subsequently triggers apoptosis. Since neurons are static cells, this effect of Gem does not come in. Vice versa, the effect does become noticeable especially in the explosively growing GBM cell lines U-87 MG and U-251 MG. Their IC_{50} is remarkably low in the low nanomolar range. Worth mentioning is that in U-87 MG, the cell viability reaches a plateau at ca. 50 % and decreases only slightly high concentrations in the millimolar range. We assume that all treated cells have in fact incorporated Gem into their DNA and undergo cell cycle arrest, however, they are still viable to a certain extent. Therefore, they can still chemically reduce the compound used to detect cell viability, and consequently contribute to increased cell viability.

For the moderately proliferating GBM cell lines A172 and LN-18, as well as for astrocytes, the IC_{50} is in the micromolar range (all IC_{50} values for Gem are summed up in Figure 21). Although these values are higher than those of U-87 MG and U-251 MG, the analysis of this data shows that Gem treatment of GBM opens a “therapeutic window”, which means that Gem concentrations low enough to harm GBM cells, but leaving neurons untainted, can be applied, especially with the controlled dosing via OEIPs.

Identical to Gem, we performed IC_{50} determination in GBM cell lines and neurons using TMZ (Figure 22). Based on this data set, we could make three main observations, (i) TMZ does not have the previously mentioned “therapeutic window”, making it difficult to treat GBM locally with TMZ at concentrations that are harmless to neurons, and (ii) TMZ values are in general higher than IC_{50} values in literature. To explain this phenomenon we hypothesize that on one hand GBM cells have a tremendously high mutagenic potential, which means that during cultivation and passaging, the cells easily mutate and develop different phenotypes that respond differently to TMZ.

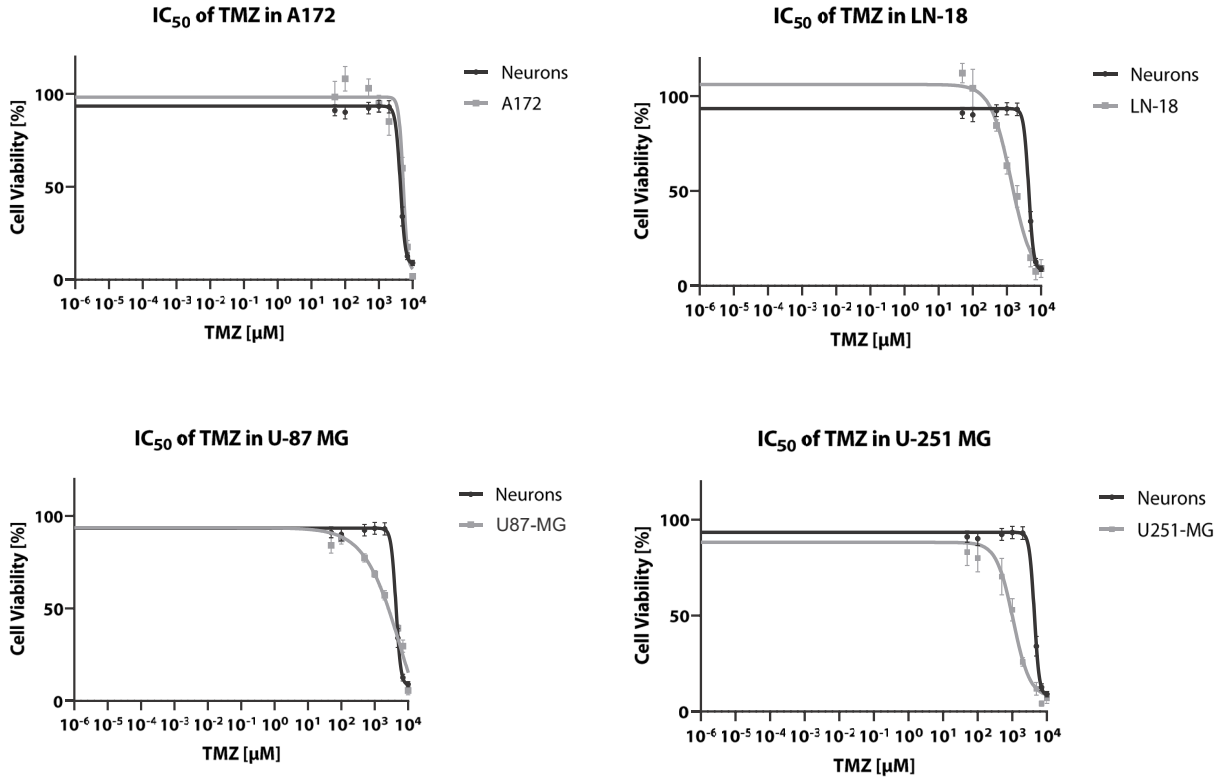

Cell line	IC_{50} TMZ [µM]
A172	5280
LN-18	1357
U-87 MG	6369
U-251 MG	1065
Neurons	4362

Figure 22 IC_{50} values of TMZ after 72 h treatment in GBM cell lines and neurons.
The values are plotted in comparison to neuronal toxicity caused by TMZ, in order to visualize the therapeutic window. All values shown as mean ± SEM, data from at least two independent experiments, n ≥ 6.

On the other hand, in the studied literature, TMZ is in general dissolved in DMSO, which is favorable since TMZ has higher solubility in DMSO than in water, and it decomposes in aqueous solutions spontaneously. Still, for generating some reported IC_{50} curves using TMZ in DMSO, the

biocompatible DMSO concentration of 0.1 % must have been overstepped. In contrast, for determination of the here presented IC_{50} values, TMZ was dissolved freshly in media each time before preparing an IC_{50} dilution series. We therefore hypothesize that the lower IC_{50} values reported in literature could also be the result of a combined toxicity from DMSO and TMZ.

The third observation (iii) was that the interference of GBM cell viability caused by TMZ occurs only at concentrations up to 100,000 fold higher than with Gem (visual comparison in Figure 23).

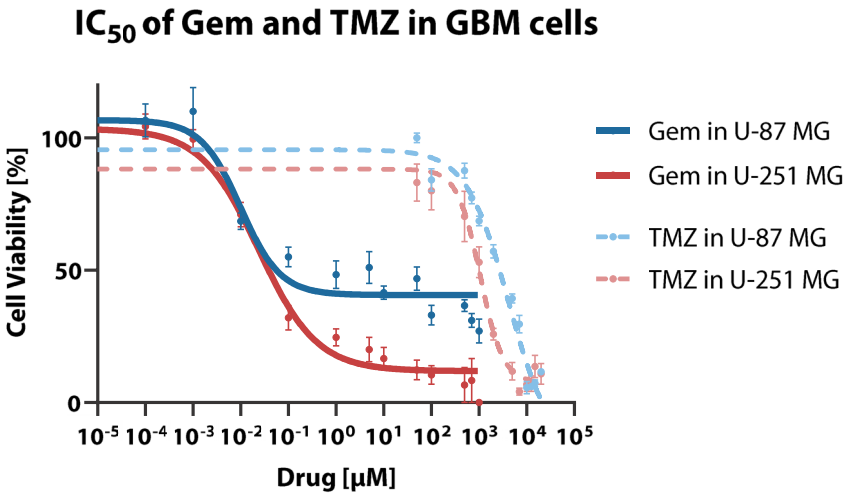

Figure 23 Comparison of IC_{50} curves of Gem and TMZ in U-87 MG and U-251 MG.
Values shown as mean ± SEM, n=6 from 2 independent experiments.

In summary, this data suggests that Gem is a potent chemotherapeutic, also in the application for GBM. It indeed induces apoptosis, inhibits cell growth and has remarkably low effective concentrations in strongly proliferating cells, while static and cells with reduced proliferation are not affected that strongly by its cytotoxic potential. Additionally, in comparison with TMZ, Gem seems to be more potent, inducing severe cytostatic effects already at low concentrations.

4.6. GemIP treatment of GBM cells in monolayers

Based on these results, we evaluated Gem as strong chemotherapeutic agent to treat GBM cells with OEIP technology. In our next experiment we had two goals, to evaluate whether Gem is still a potent cell toxic drug after it has been delivered via OEIPs, and to exclude that the OEIP setup

or operation causes cell toxic effects itself. Therefore, we installed different OEIP devices on U-87 MG cells in 96-well plates, and treated the cells manually with the same compounds as positive treatment controls (Figure 25). On one hand, we utilized GemIPs with a source electrolyte constituted of 100 mM Gem at pH 4, and conducted in parallel the manual treatment with 50 µM Gem. On the other hand, we established so called CytIPs, which are ion pumps with a source electrolyte of 100 mM Cytidine (Cyt) at pH 4. Gem is the "bad twin" of Cyt. These two molecules share the same basic structure, but Gem has two fluorine atoms incorporated in its furanose backbone at position C2 (Figure 24). Based on this, the protonation behavior of Cyt is very similar to Gem, accordingly it should be in single positive charged state at pH 4 and have a comparable electromigration behavior.

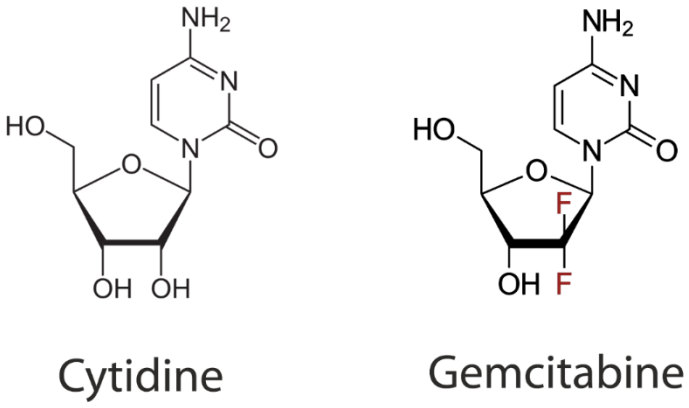

Figure 24 Comparison of Cyt (left) and Gem (right).
The two fluorine atoms are highlighted in red, resembling the main functional feature responsible for the toxicity of Gem. Both images of simple structural formulas are ineligible for copyright and therefore in the public domain, because it consists entirely of information that is common property and contains no original authorship.

The cells were treated either manually (50 µM Gem or Cyt) or with GemIPs/CytIPs for 7 h at 10 nA, followed by further 72 h of incubation and determination of cell viability (Figure 25). In parallel, untreated U-87 MG were grown as growth control.

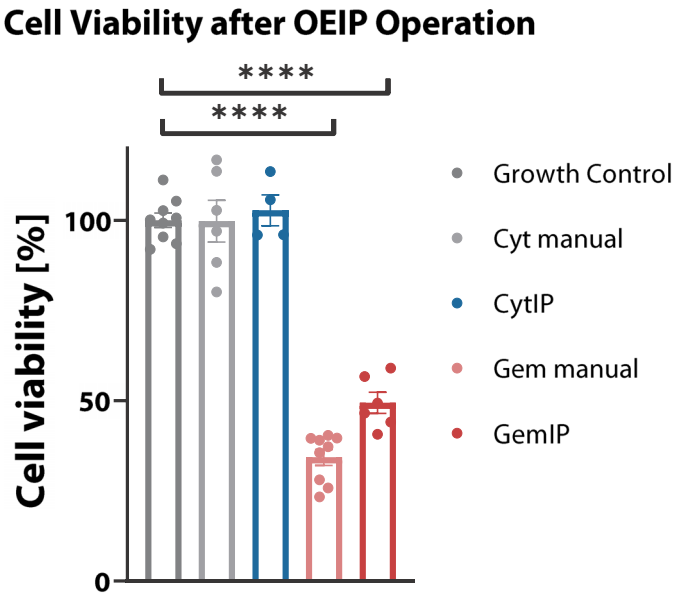

Figure 25 Evaluation of biocompatibility of OEIP mediated transport.
Cell viability of U-87 MG cells treated with both ion pumps delivering cytidine (CytIP) and Gem (GemIP) were compared with manual treatment of both compounds at 50 µM concentration. Values shown as mean ± SEM, sample size = 4-9 from at least 2 individual experiments, *** = p-value < 0.0001, one-way ANOVA.

The comparison of cell viability shows that a) neither 50 µM Cyt, nor CytIP treatment does interfere with cell viability (mean cell viability for 50 µM Cyt = 99 ± 14 %, for CytIPs = 102 ± 8 %) and does not differ to growth controls (100 ± 6 % cell viability). This shows that this OEIP setup is biocompatible and does not cause cytotoxic effects *per se*, neither does the application of the electric field, nor the electrode material. And b), this experiment showed that OEIP-delivered Gem still has the cytotoxic potential after the iontronic delivery process and is not electrochemically oxidized or reduced in an electrode reaction, nor does it react with the IEM AMPSA and becomes biochemically inactive. In fact, GemIP operation significantly reduced cell viability to 49 ± 7 % ($p < 0.0001$, one-way ANOVA), comparable to 50 µM Gem treatment which resulted in a mean cell viability of 34 ± 7 % ($p < 0.0001$, one-way ANOVA). The effects caused by GemIP treatment were also visualized microscopically (Figure 26), showing the strong cytostatic potential of the drug.

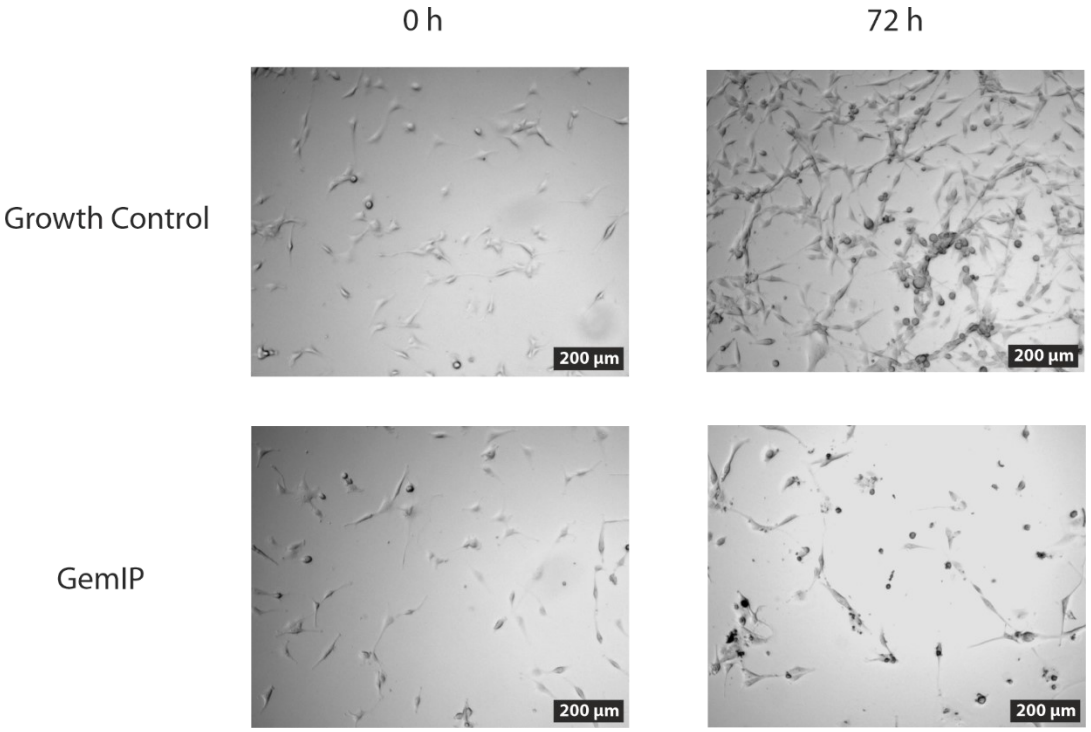

Figure 26 Microscopic images of U-87 MG before and after GemIP treatment.
Images are in comparison to untreated growth controls. Scale bars = 200 µm.

Next, we performed GemIP dosing experiments, in which we treated U-87 MG for different intervals of time and compared it with manual dosing (IC_{50} curve of Gem in U-87 MG, shown also in Figure 21 and Figure 27). GemIPs were installed identically as in the previous experiment and operated at 10 nA for different time intervals, up to 24 h, on U-87 MG cells (4000 cells/well, 250 µL growth media). In parallel, the same OEIP devices were operated for 24 h at 10 nA, but the target was not constituted of cells but of 250 µL water. The Gem concentration of the aqueous targets was measured via MS, and resulted in a mean Gem concentration of 0.2 ± 0.3 µM Gem. Based on this concentration after 24 h OEIP operation, the Gem concentration after different pump time intervals was then calculated and plotted to corresponding cell viability after 72 h. The resulting concentration-dependent cell viability curve shown in Figure 27, red.

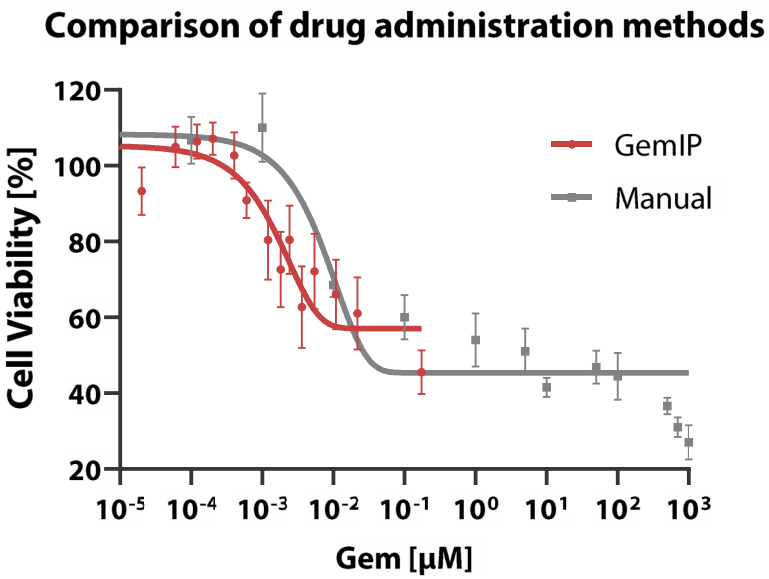

Figure 27 Dosing comparison of GemIPs vs. manual drug application in U-87 MG cells.
For manual dosing, n= 6 from 2 independent experiments, nor GemIPs, n=30 from 3 independent experiments, values shown as mean ± SEM.

This indicates that a precise dosing with GemIPs is indeed possible and comparable to manual dosing. Interestingly, the error bars become larger in proportion with the OEIP operation time, which is again an indicator for the clogging and therefore, major differences in the delivery rates and resulting cell viability.

4.7. GemIP treatment of GBM spheroids

Since our long-term goal is the use of GemIPs for treatment of brain tumors, we tested GemIPs in a more complex experimental *in vitro* setup – so called microtumors or spheroids. Tumor spheroids are formed by cultivating adherent cell lines in ultralow-attachment surface dishes – therefore, the cells cannot adhere to the surface of the dish, but they assemble in a spheroidal shaped unit (shown in Figure 28).

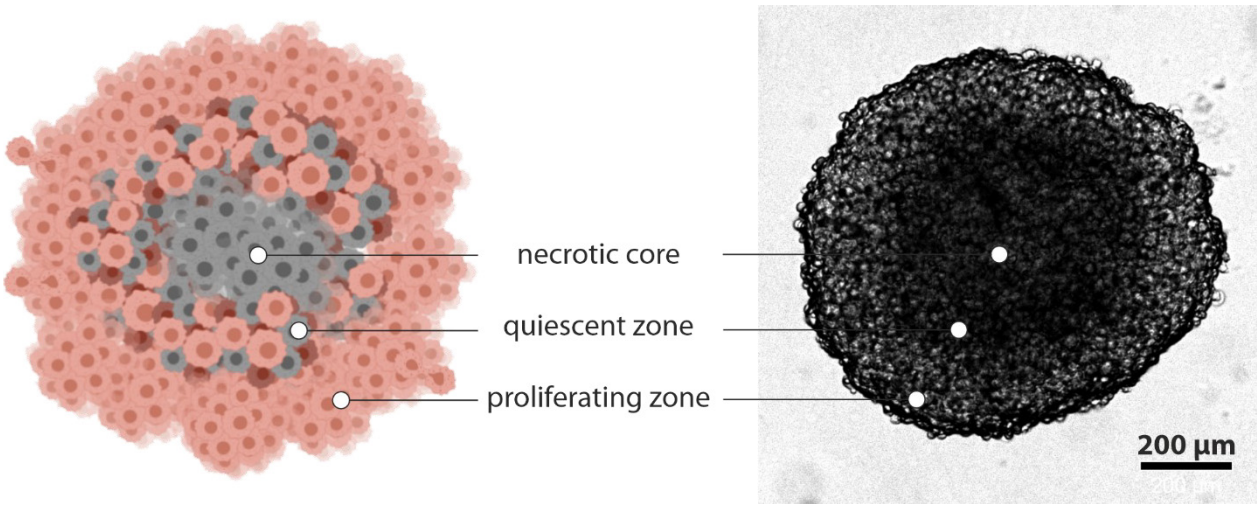

Figure 28 Schematic illustration (left) and microscopic image (right) of a spheroid.

These cell aggregates have an architecture and cellular context that is comparable to a tumor. The dense spherical structure causes restricted supply of nutrients and oxygen for cells that are in the very core of the unit (necrotic core). In the middle of the spheroid, cells are also undersupplied, which is why they go into quiescence do not divide any longer (quiescent zone). Only the very outer shell of the spheroid can proliferate normally as they are supplied with sufficient nutrients and oxygen. These described features, such as a hypoxic and necrotic core, are usually observed in native tumors. Also, intracellular interactions are mimicked in this model (138-140). Due to its simplicity, low-costs and tumor mimicking qualities, this *in vitro* tool becomes more and more established to anticipate clinical efficacy of anti-cancer treatment procedures (141). We therefore tested the GemIP treatment in U-251 MG spheroids, by positioning the capillary channel of the OEIP in close vicinity of a spheroid (Figure 29).

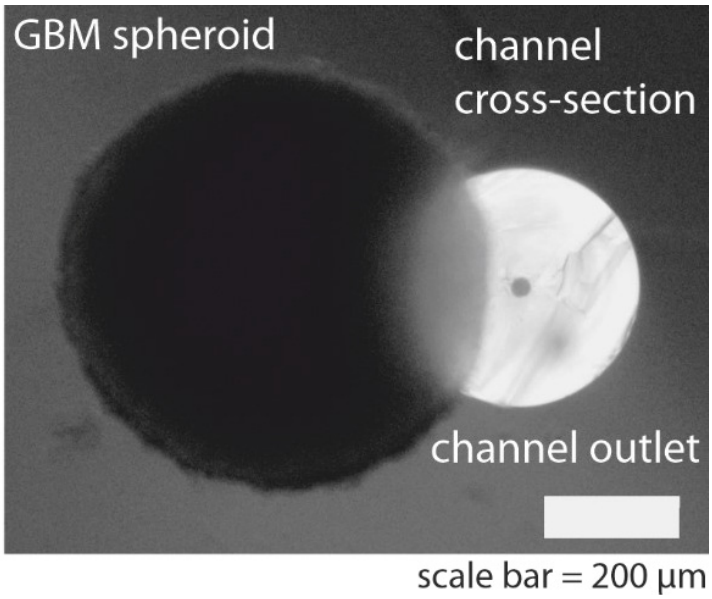

Figure 29 GemIP channel cross section next to a U-251 MG spheroid.
The spheroid was grown in ULA plates from 10,000 cells initially seeded, spheroid formation was performed over 30 h.

GemIPs were operated for 24 h at 10 nA, dismounted and, depending on the further readout, incubated for another 30 h (followed by flow cytometric analysis) or 96 h (followed by microscopy). For flow cytometric analysis (Figure 30), we carried out untreated growth controls and positive controls treated manually with 1 and 10 µM Gem. GemIPs were installed identical to previous cell OEIP experiments. In order to detect cell death in spheroids, five spheroids were pooled for each sample, cells were stained with FITC-labeled annexin V which labels early and late apoptotic cells. The FITC signal was quantified over 10,000 cell counts and afterwards stopped. The analysis showed that cell death is generally high, also untreated controls showed that 50 ± 13 % of detected cells are apoptotic (Figure 30, grey). This, however, is not surprising, considering that spheroids have a necrotic core. Apoptosis was significantly increased in all Gem-treated samples, leading to 66 ± 10 % apoptosis for 1 µM Gem (manually), 66 ± 6 % for 100 µM (manually) and 75 ± 8 % for GemIPs (Figure 30).

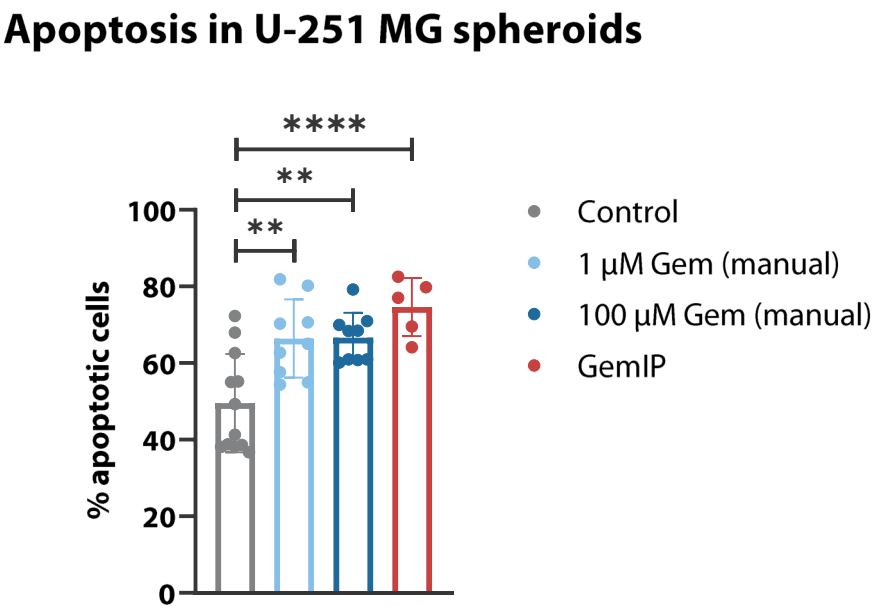

Figure 30 Flow cytometric analysis of apoptosis induced in U-251 MG spheroids.
10,000 cells/spheroid were initially used, spheroid assembly took 30 h. Treatment was done by GemIPs (24 h at 10 nA) or manual Gem application (1 and 10 µM) in comparison with untreated growth controls. Spheroids were incubated for 48 h after drug application. Results are shown as mean ± SEM, n=5-9 from three independent experiments, **: $p < 0.01$; ****: $p < 0.0001$ (two-way ANOVA).

This showed that apoptotic cell death is tremendously induced by positioning and operating a GemIP device in close vicinity of a microtumor. We also observed the spheroid cohesion and density via microscopy. Therefore, cells were identically treated as in the flow cytometry experiments, however, they were incubated for further 96 h after treatment (Figure 31).

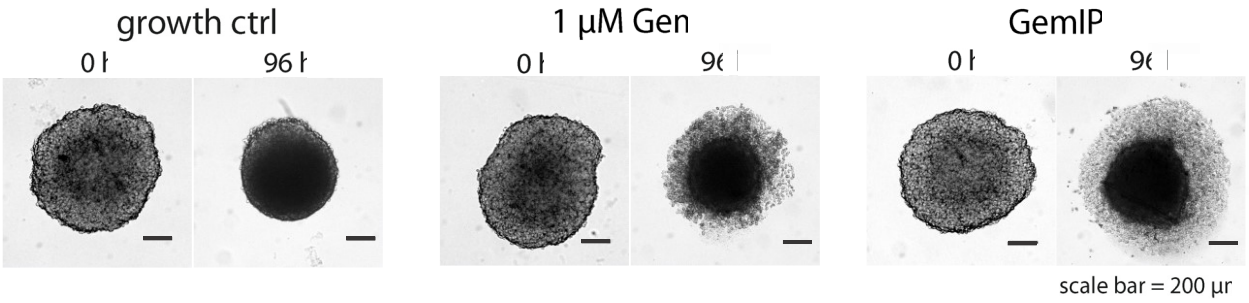

Figure 31 Microscopic comparison of U-251 MG spheroids before and after GemIP treatment.
10,000 cells/spheroid were seeded, after 30 h, the before (t = 0 h) picture was taken, after GemIP treatment and manual treatment with Gem (1 µM) for 96 h another picture was acquired. Scale bar = 200 µm.

First of all, it becomes obvious that under untreated conditions, spheroids win firmness over 96 h and become denser. However, if treated with Gem (both manually and with GemIP), the cell interactions are disturbed and the spheroids fall apart. This can also be seen by the halo-like disintegrated cells around the dark spheroid core. We also observed that handling spheroids treated with Gem is quite difficult as they fall apart during pipetting processes or mild centrifugation, which can be normally performed in healthy spheroids without harming them. Therefore, we showed that GemIPs can significantly and relevantly induce apoptosis in microtumors to an extent that the cell aggregation is completely destructed.

4.8. Chlorambucil – another potential drug for treatment of GBM

In order to find other chemotherapeutic drugs that can be applied via OEIP mediated drug delivery, we found chlorambucil (CLB) as potential candidate. Simultaneous to experiments in chapter 4.5, IC_{50} curves were measured for CLB in A172, LN-18, U-87 MG and U-251 MG cells (Figure 32). It becomes clear that CLB has not as potent features as Gem, with IC_{50} values in the micromolar range around 100 µM, however, there is still a therapeutic window comparing the IC_{50} of CLB in neurons, which is twice as high as in GBM cell lines.

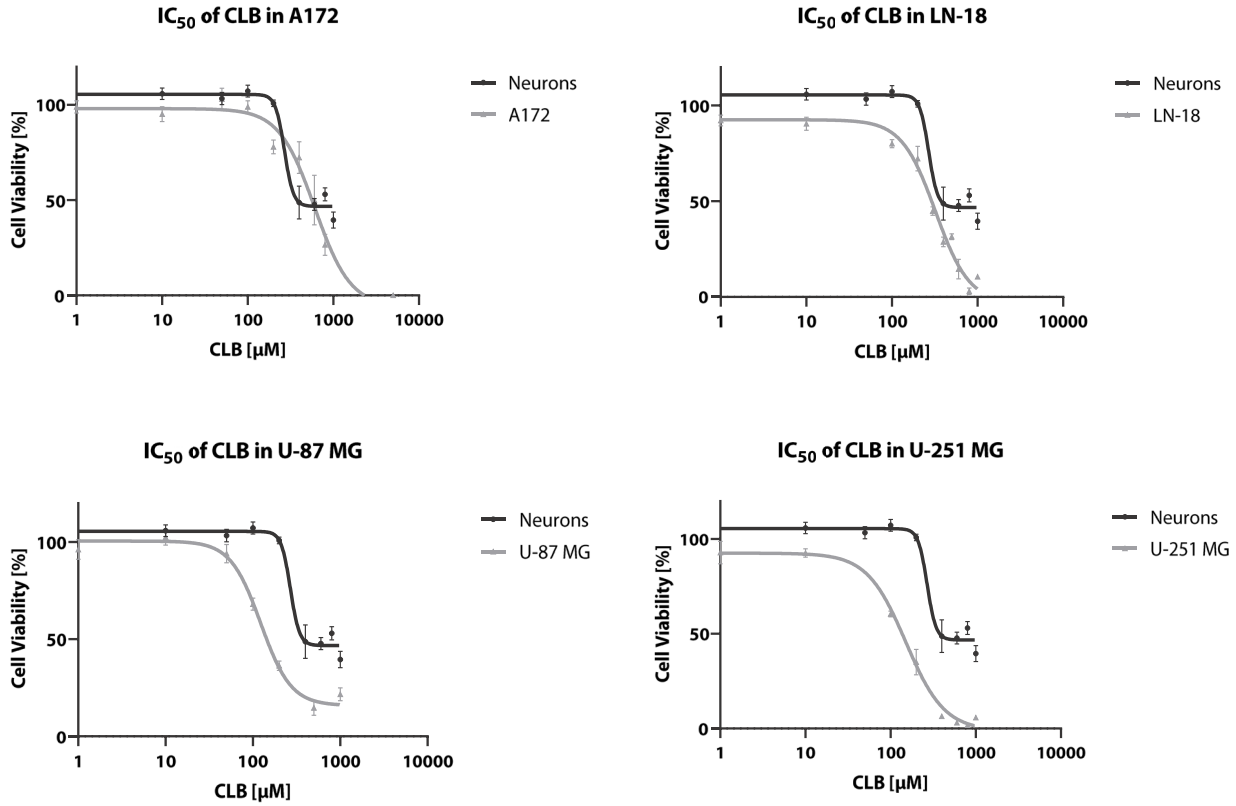

Cell line	IC_{50} CLB [µM]
A172	98
LN-18	93
U-87 MG	100
U-251 MG	92
Neurons	268

Figure 32 IC_{50} values of CLB after 72 h treatment in GBM cell lines and neurons.
The values are plotted in comparison to neuronal toxicity caused by CLB, in order to visualize the therapeutic window. All values shown as mean ± SEM, data from at least two independent experiments, n ≥ 6.

5. Summary and Discussion

Bioelectronic drug delivery via OEIP technology is a new and evolving field. To our knowledge, we established first iontronic drug delivery platform in Austria at the Gottfried Schatz Research Center at the Medical University of Graz. In close collaboration with our partners from Linköping University (LiU, SE), we successfully established well-equipped OEIP operation set ups. Also, we laid base for a broad scientific network at the Medical University of Graz to work on this interdisciplinary project. With the help of all these outstanding and open-minded scientists, it was possible to take the first ground-breaking steps in the revolution of brain cancer treatment with bioelectronic drug delivery technologies.

After the operation of OEIPs was established in our lab, we started with the search for appropriate chemotherapeutics and found the "old-school" compound Gem, which we considered based on molecular size and chargeability suitable for our purpose. Therefore, in first experiments the applicability of Gem via OEIPs was tested, and was indeed, successful. Also, the stability of the compound at acidic pH values over three weeks, and its outstanding cell killing properties were a motivation to use this drug for further steps. Gem does not only induce cell death at lowest concentrations in the nanomolar range in most aggressively growing GBM cell lines (124, 134), it also vehemently stops tumor cell proliferation and growth at concentrations that do not affect neuronal cell viability. Importantly, the main cellular pathway that cells treated with Gem undergo is apoptosis, which is absolutely favorable compared to necrosis. Instead, necrosis is often connected with uncontrolled inflammation. Interestingly, Gem is also much more potent compared to the gold standard medication TMZ, which is in line with Rieger et al., 1999 (134). Also, CED-mediated Gem administration to brains of rats (142) and non-human primates (143), showed that a single Gem dose (up to 15 mM) can be well tolerated without observation of tissue toxicity over a period of up to 42 days. These reports and our own findings gave us the motivation to continue the OEIP mediated delivery of Gem via GemIPs for the treatment of GBM cell monolayers and GBM microtumors. Also, in the treatment of GBM cells, Gem delivered via GemIPs was a potent cell killer. Not only killing of GBM cell monolayers, but outstandingly also of GBM microtumors was successfully performed via GemIP mediated delivery

of the drug. Considering more the GemIP delivery itself, we showed that a precise dosing via the applied electric field is indeed possible and, in fact, comparable to manual application of known drug concentrations. However, we also observed obstacles in the operation of GemIPs. Due to the structure of Gem, a long term delivery of Gem through the IEM is limited. We assume that due to π-π-electron interactions between the IEM material polyAMPSA and the electrons of the aromatic ring in Gem, a build-up of Gem in the IEM occurs. This might be also facilitated by the more rigid and spacious molecular structure of the cytotoxic compound. What occurs within the capillary channel exactly could not be addressed, however, we definitely observe an increase in capillary channel resistance, and a reduction of GemIP drug delivery performance when devices are operated multiple times. This problem has to be overcome in the next generations of GemIPs. Our first approach is to exchange the IEM material to so-called dendrolyte polymers, established by our cooperation partners from LiU (120, 144, 145). Utilizing the dendrolyte IEM material could also reduce the amount of co-delivered H^+ ions, and therefore, reduce OEIP operation times. Another way to overcome clogging is by adapting the design, shape or dimensions of the capillary channels. Besides that, this is important for further applications in more complex animal models.

Currently, we plan to establish an **EL**ectro**PH**oretic **I**mplant (ELPHI), which has a spherical design of multiple capillary channels assembled into a soft and biocompatible implant shell in a way that they span the implant walls (Figure 33). Within ELPHI's body, the reservoir electrode is incorporated into the drug reservoir. At the surface of the implant, the counter electrode is placed.

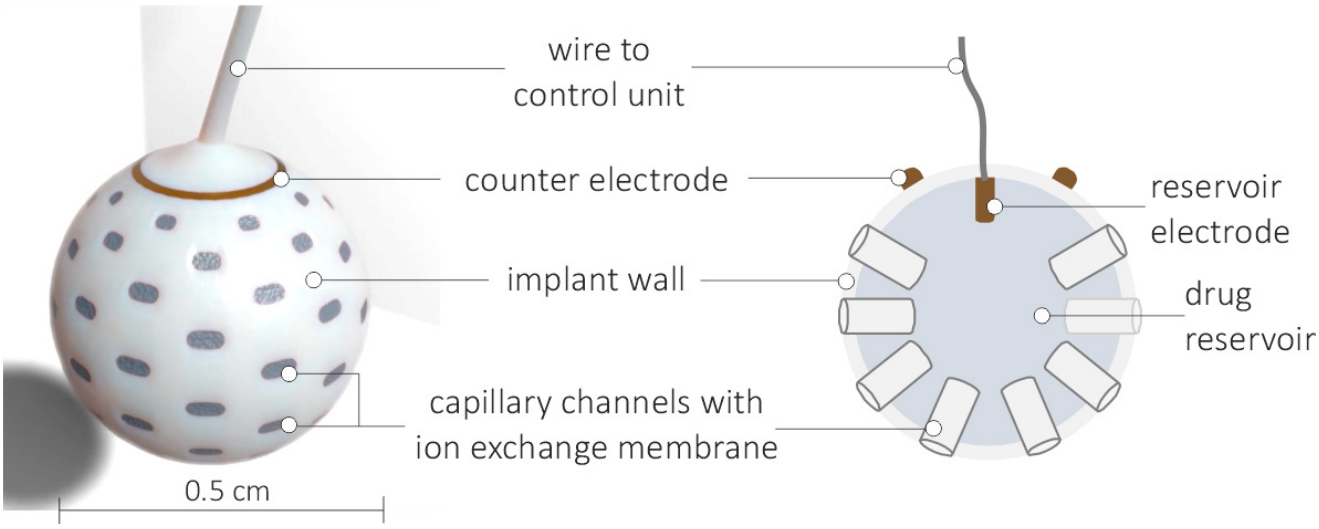

Figure 33 Current electrophoretic implant design: ELPHI.

The electric control will be performed via a distant control unit, which is connected to the implant via subcutaneous wiring (Figure 34). The control unit is placed beneath the collar bone, similar to a heart-pace-maker, and can be switched on and off by inductive fields.

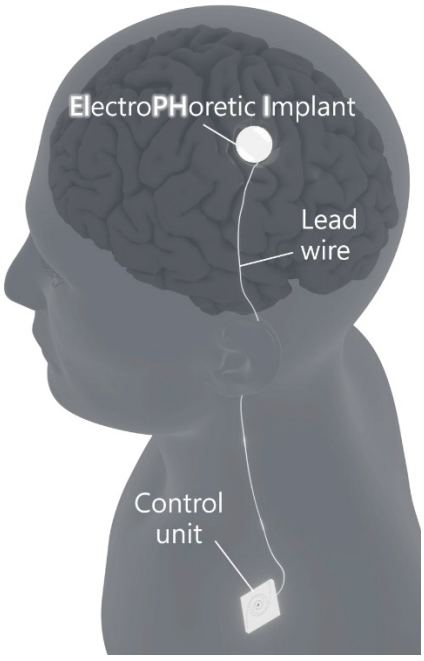

Figure 34 Whole body view of the implant ELPHI in the brain.
The implant body is connected with its distantly placed control unit via subcutaneous wires.

Our final goal is therefore to place the whole ELPHI system (electrophoretic device in the brain, wires and control unit) after tumor resection into the operation cavity, close the patient and let an important healing period hold on. After the healing, ELPHI can be operated for certain windows, and can be combined with TMZ therapy and radiation. We expect, that with an added dimension of treatment possibilities, the recurrence and progress of GBM can be drastically diminished and that life expectancy of GBM is higher and qualitatively higher.

Part II: Investigation of the Binding Dynamics of the Store Operated Calcium Entry Channel Blocker Synta66 and its Potential Application in GBM

Kurzzusammenfassung

Ionenkanalkomplexe, bestehend aus dem Kalziumkanal Orai1 und dem Kalziumsensor Stromal interaction molecule 1 (STIM1), vielversprechende Angriffsziele in der Entwicklung neuer Medikamente, vor allem zur Behandlung von Entzündungs- und Auto-Immunerkrankungen, auch aber mit wachsendem Interesse für die Behandlung von Krebs. In dieser Arbeit untersuchen wir deshalb den Orai1-Hemmer Synta66 auf seine mögliche Rolle in der Therapie von Glioblastomen. Dafür wurde einerseits die Interaktion von Synta66 in der Orai1-Pore, andererseits die Synta66-verursachten Effekte in Glioblastomzellen untersucht. Unsere Ergebnisse zeigen, dass Synta66 eine sehr selektive Bindung in der Orai1-Pore eingeht, welche durch Mutationen in der Bindungsregion abgeschwächt wird. In *in vitro* Versuchen mit drei Glioblastomzelllinien sieht man, dass Synta66 das Einströmen von Kalzium durch den Orai1-STIM1-Kanal komplett hemmt, diese Hemmung jedoch keinen Effekt auf die Lebensfähigkeit beziehungsweise das Wachstum dieser Zellen hat. Auch eine kombinierte Behandlung mit Synta66 und dem Chemotherapeutikum TMZ war nicht in der Lage, die Zellen sensitiver auf TMZ zu machen. Aufgrund dieser Resultate betrachten wir Synta66 als präzises Werkzeug zur Untersuchung von Orai1-STIM1-mediierten Signalkaskaden, beurteilen es jedoch als ungeeignet für den Einsatz in der Glioblastomtherapie.

Abstract

Development of new drugs is often based on targeting proteins that play essential roles in cell signaling processes, such as the store-operated Ca^{2+} (SOC) channel complex constituted from the Ca^{2+} sensor stromal interaction molecule (STIM1) and the Ca^{2+} channel Orai1. This channel complex is an interesting target for development of drugs to treat auto-immune and inflammatory diseases, but also for cancer treatment. We therefore investigated the Orai1-inhibitor Synta66 on its potential role as an anti-cancer drug. The binding interactions of Synta66 with the Orai1 pore were investigated from different angles, on one hand the site of binding was investigated by performing patch clamp recordings and computational analyses, on the other hand, *in vitro* experiments observing Synta66 effects in three GBM cells were conducted. We found that Synta66 selectively binds to Orai1 in the pore region, which can be diminished by introducing different mutations in the pore region. Synta66 binding results in effective inhibition of SOCE, however, does not interfere with cell viability, growth nor does it synergize with TMZ treatment. Therefore, we suggest Synta66 as highly selective SOCE inhibitor to study effects downstream of SOCE signaling, however, not as a drug for GBM treatment.

6. Introduction

6.1. Store Operated Calcium Entry

Store-operated Ca^{2+} channel entry (SOCE) is a ubiquitous cellular mechanism to generate long lasting calcium signals, of key relevance especially for immune cell function, including T-cell activation (146-150). SOC channels are specifically localized in endoplasmic reticulum (ER) - plasma membrane (PM) junctions, formed by the highly Ca^{2+} selective plasma membrane channel Orai and the Ca^{2+} sensor protein stromal interaction molecule (STIM), located in the ER. Upon ER store-depletion, these two proteins bind directly to each other to mediate the Ca^{2+} release-activated Ca^{2+} channel (CRAC) current (151-153). Loss-of-function mutations in either STIM or Orai result in severe combined immune-deficiency, muscular hypotonia and ectodermal dysplasia. Instead, gain-of-function mutations are the cause of the multisystemic Stormorken Syndrome (MIM#185070), cognitive defects, miosis and for tubular aggregate myopathy (TAM) (MIM#160565) (154, 155).

6.2. Structural Aspects of Orai

Taking a closer look at the Orai channel, it becomes clear that the channel has unique and rather unusual structure and properties in comparison to other ion channels. While many ion channels are formed from tetramers, the crystal structure of *Drosophila melanogaster* Orai (dOrai) revealed that Orai channels form by arranging six subunits around a central axis, establishing a homomeric hexamer, shown in Figure 35 (156). Each subunit comprises four transmembrane (TM) helices (M1-4) which span the membrane. The M1 helices form a funnel-like pore when they assemble in the hexamer, which has a length of 5.5 nm (156). Through the pore, Ca^{2+} ions are conducted one after another in a so-called single ion conduction mode (156). Helices M2 and M3 do not participate in the pore formation. M4 extends into the cytosol (M4 extension helix) and can stake two conformation states that occur in pairs (one green and one orange state per pair). Therefore, the Orai hexamer has three-fold symmetry, shown in Figure 35 (156).

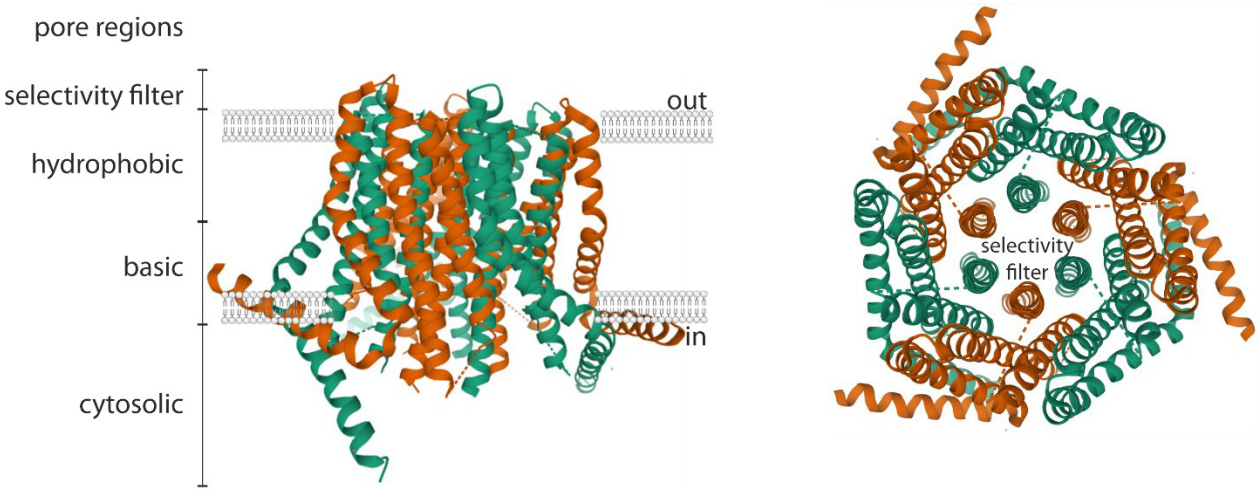

Figure 35 Protein structure of the Orai hexamer.
The Orai hexamer is formed from green and orange subunits shown from the side (left) and top (right) in its closed conformation. The pore is sectioned into four regions, selectivity filter, hydrophobic and basic region and cytosolic region. PDBID: 4HKR. Reproduced with permission of the publisher "The American Association for the Advancement of Science" according to license number 4938210478680.

The Orai channel pore is divided into the selectivity filter, the hydrophobic and basic pore region and the cytosolic part (Figure 35, left). At the extracellular pore entrance, a ring of glutamates (position E106 in M1) forms the selectivity filter (Figure 35, right). Due to the selectivity filter and the hydrophobic pore, the permeability for Ca^{2+} is 1000-fold higher than for Na^{+} (157, 158), which is another outstanding feature of this ion channel. The glutamate side-chains allow a transient binding of Ca^{2+} ions and can be either an up- or down-rotamer, which brings flexibility and therefore, presumably facilitates ion accommodation and permeation (159). It is tempting to speculate that a Ca^{2+} bound to the down-rotamer is pushing into the hydrophobic pore when a second Ca^{2+} binds to glutamate residues in the up-rotamer. The hydrophobic part of the pore is found more central and is the narrowest section of the pore. Three subsequent pore-lining hydrophobic residues of M1 are expected to largely diminish even permeation of single water molecules in the closed channel configuration (160, 161), shown in Figure 36.

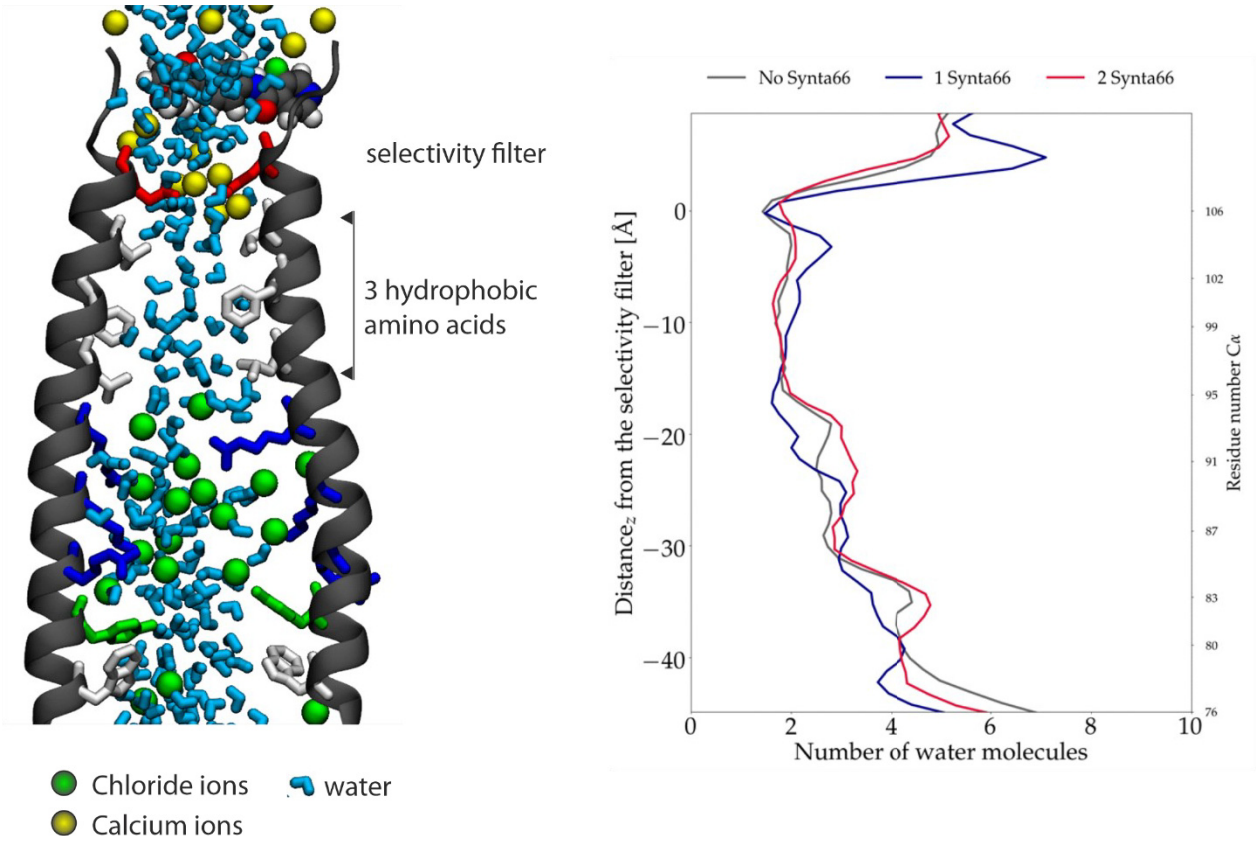

Figure 36 Hydration profile of the Orai pore.
On the left the Orai pore is shown with Synta66 in its binding pocket close to the selectivity filter. Blue sticks resemble water molecules, green and yellow spheres resemble chloride and calcium ions, respectively. To the right the pore hydration profile across the pore is shown.

Consequently, Ca^{2+} ions would not be able to pass this hydrophobic pore segment in the crystallized closed dOrai conformation. Therefore, to enable Ca^{2+} gating, the TM helices move outward and widen in the hydrophobic region by ~ 2 Å. This widening can also be imitated by introducing a mutation at position H134 (H134A mutation) in the mid-section of the pore (161), shown in Figure 37 . This is sufficient to induce Ca^{2+} permeation with the low conductivity of Orai channels below 1 pS (163). Electrostatic repulsion of monovalent ions by Ca^{2+} in the pore is expected to increase the selectivity even further. Only in divalent-free conditions (DVF), Orai

channels conduct monovalent ions (163). Physiologically, Orai gating is mediated via direct binding to STIM1/2 that induces a small extension of the Orai channel (159, 161).

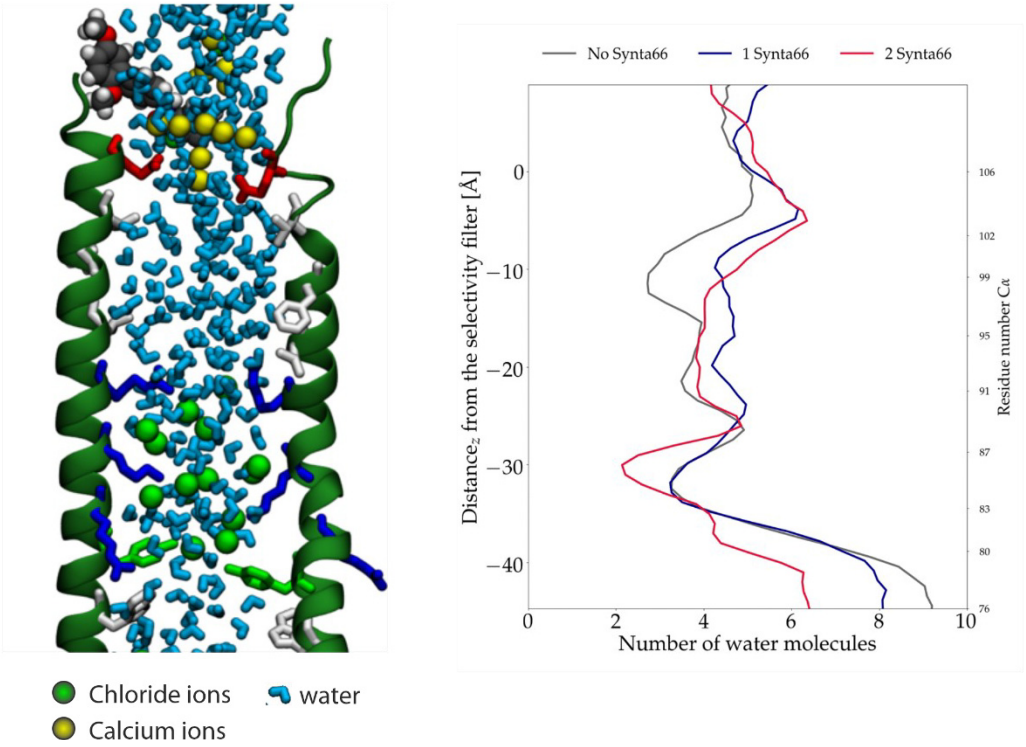

Figure 37 Hydration profile of the Orai1-H134A-pore.
On the left the Orai pore is shown with Synta66 in its binding pocket close to the selectivity filter. Blue sticks resemble water molecules, green and yellow spheres resemble chloride and calcium ions, respectively. To the right the widened pore is shown, having increased pore hydration, especially in the hydrophobic region.
Reproduced from (162). All co-authors have agreed to the inclusion of their published data in the dissertation. The reproduction of illustrations and figures from own or third-party publications is granted according to Creative Commons CC BY 4.0 license.

In order to find the amino acids that play a key role in Orai Ca^{2+} selectivity, different mutations have been introduced into the channel and channel characteristics were observed (summarized by Krizova et al. (164)). For my project, studying the interaction of Synta66 with Orai1, the mutations E106D and H134A were observed in more detail, shown in Figure 37. Mutation of the selectivity filter E106 to aspartic acid (E106D) has been shown to reduce Ca^{2+} selectivity and enhance pore diameter (165-167). Mutation of H134A (in M2, see Figure 37) results in a highly Ca^{2+} selective channel, with a pore showing similar properties to a STIM-activated channel (161, 168).

6.3. Structural Aspects of STIM

STIM1 is a finely tuned sensor that responses to calcium levels in the range of 100-400 μM (169, 170) in restricted ER-PM junctions (171, 172). In resting cell conditions, STIM1 reveals a dynamic constitutive movement along microtubules, whereas store-depletion results in redistribution of STIM1 into cluster/puncta at ER-PM junctions (173, 174). STIM2 responds already to small changes in ER Ca^{2+} which makes it an ideal trigger for low agonist stimuli (175, 176). Both STIM1 and its close homolog STIM2 are single-pass transmembrane proteins with their N-terminus residing in the ER lumen and their larger C-terminal part within the cytosol. STIM1 and STIM2 share two important functions, i) sensing ER Ca^{2+} levels and ii) binding and activating Orai channels to generate Ca^{2+} signals. Their ER luminal part, which functions as a Ca^{2+} sensor of intraluminal $[Ca^{2+}]_{ER}$, contains a Ca^{2+} sensing canonical (c) EF hand, a stabilizing non-canonical (n) EF hand and a sterile α-motif (SAM) domain followed by a single α-helical transmembrane (TM) domain (177-183). Upon decrease of ER Ca^{2+} levels, the bound Ca^{2+} ion dissociates from the cEF hand which, together with a far N-terminal STIM1 sequence, destabilizes the EF hand-SAM complex (179, 184-187). This triggers a STIM1 di/oligomerization mechanism which is transduced to the C-terminal site via a long coiled-coil 1 (CC1) helix. Biochemical experiments suggest that the di/oligomerization is mediated via a zipper mechanism (188, 189). This zipping mechanism then leads to the release of a larger cytosolic binding pocket, named SOAR (STIM–Orai activating region) or CAD (CRAC activation domain) for coupling to and activation of Orai channels (180-182).

6.4. The role of SOCE inhibition in brain cancer treatment

Interference with calcium signaling has been shown to have great potential in drug development, especially for treatment of immune and inflammatory diseases. FDA approved therapies that interfere with calcium signaling are foremost regulators of immune responses (e.g. T-cell activation modulators cyclosporine A and FK506 (190)). Aside from immunosuppressors, development of anti-cancer agents targeting SOCE channels emerged within the last years. Especially for hard-to-treat cancers there is a permanent search for new cellular targets that could be an alternative to standardized chemotherapeutic cytostatics and methylating agents.

Interference with different channels, including STIM/Orai has been shown to restrict cancer cell progression (reviewed in (191, 192)).

Of course, the potential of SOCE inhibitors as treatment for GBM, which is currently unsuccessfully treated, has been considered and researched (192, 193). Generally, SOCE in the brain is regulated in astrocytes via by STIM1 and Orai1, triggering the vesicular release of cellular transmitters such as ATP (194). There is evidence that knockdown of STIM1/Orai1 via siRNA diminishes cell growth (195, 196), migration (197) and invasion (198), and can induce cell cycle arrest (199). These studies put forth the idea of utilizing SOCE blockers as GBM treatment alternative, which has indeed been studied in different GBM cell lines using the blockers diethylstilbestrol (DES), SKF-96365 and 2-aminoethoxydiphenyl borate (2-APB). All of them efficiently hindered SOCE, which resulted in reduction of migratory potential and induction of apoptosis in GBM cell lines (195, 196, 198, 200).

However, the impact of SOCE inhibitors can vary quite severely among GBM cell lines (195, 196, 200). This could be owed to the high genetic instability observed in GBM and consequently, differences in expression of STIM1/2 and Orai1/2/3. Due to the fact that some SOCE inhibitors act differently on ion channel isoforms, the expression pattern could strongly influence the outcome of the SOCE inhibition. Additionally, SKF-96365 and 2-APB have been shown to inhibit other ion channels as well (201). Therefore, we need to address the elephant in the room, which is to clarify whether the anti-cancer effects result specifically from SOCE inhibition or are a conglomerate of cellular effects due to alterations in the cell machinery.

7. Aims and Objectives

In this study, we investigated the SOCE blocker Synta66 (shown in Figure 38) in three different GBM cell lines A172, LN-18 and U-87 MG. We observed the potential of Synta66 mediated SOCE inhibition and investigated the influence on cell viability and growth in these GBM cell lines. Additionally, Synta66 was structurally compared with another SOCE blocker that is currently used in clinical trials and evaluated whether Synta66 can synergize TMZ treatment.

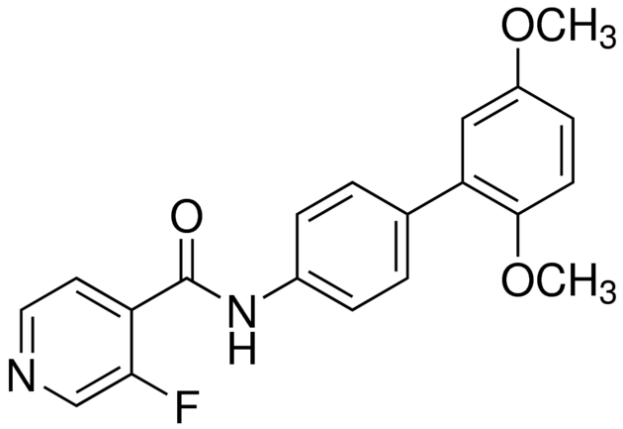

Figure 38 Molecular structure of Synta66, PubChem CID 11337104.
This image of a simple structural formula is ineligible for copyright and therefore in the public domain, because it consists entirely of information that is common property and contains no original authorship.

To bring our observations into a broader context and to elucidate the binding events between Synta66 and the Orai1 pore, we observed the inhibitory action of Synta66 in different Orai1 pore geometries via patch-clamp experiments in cooperation with colleagues from Johannes Kepler University Linz. Furthermore, in cooperation with the Academy of Sciences of the Czech Republic in Nove Hrady, computational docking experiments, molecular dynamics simulations and hydration profiles of different Orai pores were generated. Additionally, measurement of Förster Resonance Energy Transfer (FRET) was performed at Johannes Kepler University Linz to observe whether Synta66 interferes with Orai-Orai and STIM-Orai coupling. The results are summarized and published in Waldherr et al. 2020 Cancers (162).

8. Materials and Methods

Methods are also described in Waldherr et al. 2020 Cancers (162).

8.1. Cell culture

Cultivation of U-87 MG cells is described in chapter 3.4. A172 (Medical University of Graz cell culture core facility) were cultivated in Dulbecco's Modified Eagle's Medium (DMEM) supplemented with 10 % FBS. LN-18 cells (ATCC, USA) were cultivated in DMEM supplemented

with 5 % FBS. All cell lines were cultured for a maximum of ten passages following the recovery of frozen cells. All media and supplements were obtained from Thermo Fisher Scientific, USA.

8.2. Compounds

Temozolomide (Merck Millipore, USA) was stored as powder at 4 °C and dissolved in corresponding media immediately before use. Synta66 (Merck Millipore, USA) was stored as a 50 mM stock solution in DMSO at -80°C until use. For use of Synta66 in cell experiments, stocks were dissolved to a maximum DMSO concentration of 0.1 %.

8.3. Calcium Imaging

80 % confluent cells on glass cover slips were loaded with 1 µM FURA-2-AM (Sigma-Aldrich, USA) in Calcium-free Tyrode buffer for 40 min at room temperature/dark, followed by washing with calcium free tyrode buffer ± 10 µM Synta66 for 10 min at RT/dark. During the recordings (Olympus IX71) using Live Acquisition v2.6 software (FEI, Planegg, Germany), cells were excited alternately using 340/26 and 380/11 nm filters (Semrock, Rochester, NY, USA) in an Oligochrome excitation system (FEI), and fluorescent images were captured using 510/84-nm emission filter (Semrock) with an ORCA-03G digital CCD camera (Hamamatsu, Herrsching am Ammersee, Germany). The 340/380 ratio was used as an index of cytosolic Ca^{2+} levels. In time-course experiments, fluorescent cells were recorded initially in a calcium-free tyrode solution followed by addition of 30 µM BHQ. Subsequently, fluorescent cells were recorded in a 2 mM calcium tyrode solution with 30 µM BHQ. Analogous experiments were recorded in the presence of 10 µM Synta66.

Calcium free Tyrode buffer consisted of (in mM) 0.1 EDTA, 138 NaCl, 1 $MgCl_2$, 5 KCl, 10 Hepes, 10 Glucose, pH 7.4. 2 mM Calcium Tyrode buffer consisted of (in mM) 2 $CaCl_2$, 138 NaCl, 1 $MgCl_2$, 5 KCl, 10 Hepes, 10 Glucose, pH 7.4.

2 mM Calcium Tyrode buffer consisted of (in mM) 2 $CaCl_2$, 138 NaCl, 1 $MgCl_2$, 5 KCl, 10 Hepes, 10 Glucose, pH 7.4. 2 mM Calcium Tyrode buffer consisted of (in mM) 2 $CaCl_2$, 138 NaCl, 1 $MgCl_2$, 5 KCl, 10 Hepes, 10 Glucose, pH 7.4.

8.4. Western Blotting

Harvesting of cells and preparation of lysates was performed on ice. Cells (80 % confluent 10 cm dishes) were harvested in ice-cold PBS with a cell scraper, pelleted by centrifugation (500 rpm, 4 °C, 6 min) and washed 2x with PBS before lysis in 700 µL of ice-cold lysis buffer (0.5% Nonidet P-40, 20 mM Tris-HCl, 100 mM NaCl, 2 mM EDTA, 10% glycerol) for 30 min on ice with pipetting. Lysed cells were then centrifuged for 10 min, 4°C, 14,000 rpm and the protein content of the supernatant was estimated via BCA Assay (Thermo Fisher Scientific, USA). For Orai1 western blotting, lysates (20 µg) were de-glycosylated using a PNGase F kit (New England Biolabs, USA), according to the manufacturer's protocol. For STIM1 western blots, lysates remained glycosylated. Afterwards, (de)glycosylated lysates were separated by SDS-PAGE, transferred to a nitrocellulose membrane, which was blocked with 5% BSA in TBS-T for 1 h. The primary antibodies were diluted in corresponding blocking buffer (Orai1 from Sigma-Aldrich, USA at 1:2000 dilution, vinculin from Sigma-Aldrich, USA at 1:5000 dilution, STIM1 from Abcam, USA at 1:1000 dilution, GAPDH from Abcam, USA at 1:1000 dilution) and the membranes were incubated over night at 4°C. Visualization was performed by incubating with horse radish peroxidase-conjugated secondary antibodies and enhanced chemilumiscent reaction (GE Healthcare Amersham, USA) on a ChemiDoc MP Imaging System (BioRad, USA). Band intensities were analyzed using ImageJ.

8.5. Cell viability (MTS Assay)

Cell viability was observed in seeded in 96-well plates with 4000 cells/well. Cells were treated with 1 µM and 10 µM Synta66 (0.1% DMSO in each) and cell viability was measured via MTS assay (CellTiter 96 AQueous One Solution Cell Proliferation Assay, Promega, Germany) after 24, 48 and 72 h on via absorption at 490 nm (CLARIOstar, BMG Labtech, Germany).

8.6. Cell growth (Hoechst Assay)

Cells were seeded in flat-bottomed black-walled 96-well plates (Corning, USA) at a density of 8000 cells/well in 200 µL media. After attachment, cells were treated with 1 or 10 µM Synta66

(0.1% DMSO). Number of nuclei was determined with Hoechst stain as described in chapter 3.7 after 0, 24, 48 and 72 h at 350nm/455nm (CLARIOstar, BMG Labtech).

8.7. IC_{50} with Synta66 and TMZ

Protocol described in detail in chapter 3.5. Briefly, U-87 MG and A172 cells were seeded at a density of 4000 cells/well, and LN-18 cells at a density of 2000 cells/well. After settling, cells were treated for 72 h with a range of freshly prepared TMZ solutions (TMZ concentrations [µM]: 0, 50, 100, 500, 1000, 2000, 5000, 7000, 10000, 12500, 15000, 20000) ± 10 µM Synta66. 0

9. Results

The here presented results have been published in Waldherr et al., Cancers, 2020 (162).

9.1. Western Blotting for Orai1 and STIM1

Due to the fact that inhibition of STIM1 and Orai1 signaling were the proteins of interest in our further studies, we verified the expression of both proteins in cell lines U-87 MG, A172 and LN-18 by performing western blot analysis of deglycosylated cell lysates (for Orai1, to achieve clear bands as in (202)) and normal lysates for STIM1 (Figure 39A, B). In LN-18, Orai1 expression is the highest, followed by A172 and U-87 MG (Figure 39A). STIM1 expression is highest in A172, followed by LN-18 and U-87 MG (Figure 39B).

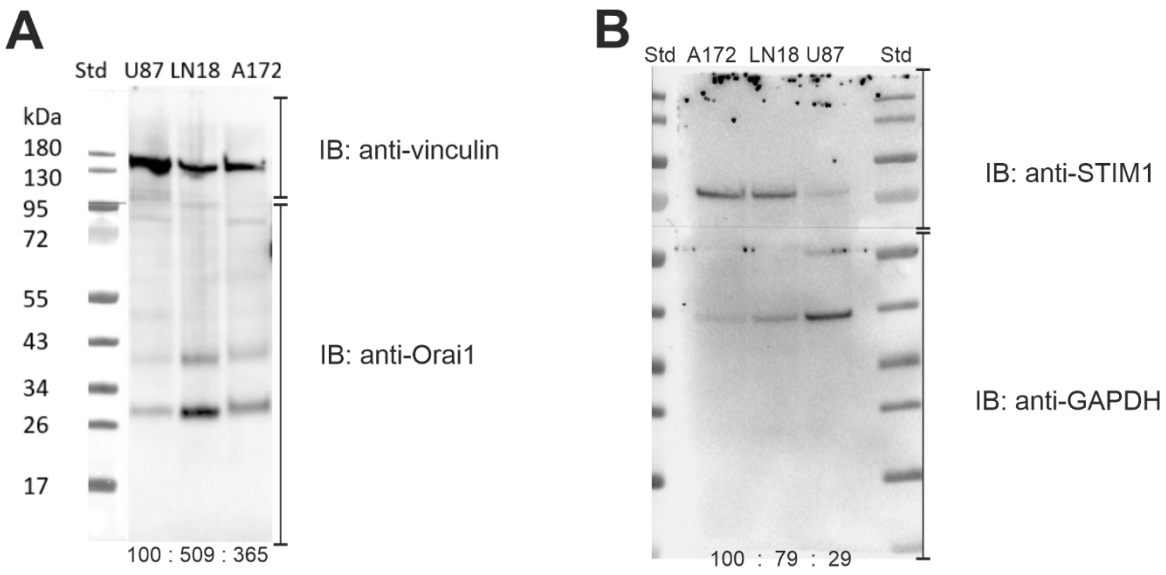

Figure 39 Western Blot for Orai1 (A) and STIM1 (B)
Loading controls are vinculin and GAPDH, respectively. At the bottom, relative intensities, normalized to the first band, are shown. Reproduced from (162). All co-authors have agreed to the inclusion of their published data in the dissertation. The reproduction of illustrations and figures has been granted from the publisher "MDPI Cancers" according to Creative Commons CC BY 4.0 license.

9.1. Calcium Recordings in GBM cell lines with Synta66

Subsequently, we evaluated the inhibitory potential of Synta66 on SOCE in the mentioned three cell lines. Therefore, we determined relative SOCE by performing ratiometric Ca^{2+} imaging in Fura-2 AM loaded GBM cells (Figure 40C-F). To start off, cells were observed a Ca^{2+}-free Tyrode buffer, with subsequent depletion of the ER by inhibition of Sarcoplasmic/endoplasmic reticulum calcium ATPase (SERCA) pumps with benzohydroquinone (BHQ, 30 µM). This resulted in transiently increased cytosolic [Ca^{2+}]. Consequently, Tyrode buffer containing 2 mM Ca^{2+} was added and SOCE was activated and measured (Figure 40, black traces). The identical procedure was performed with cells that were incubated with 1 and 10 µM Synta66 for 10 min before measurement and in the presence of Synta66 during the whole measurement (Figure 40, blue traces).

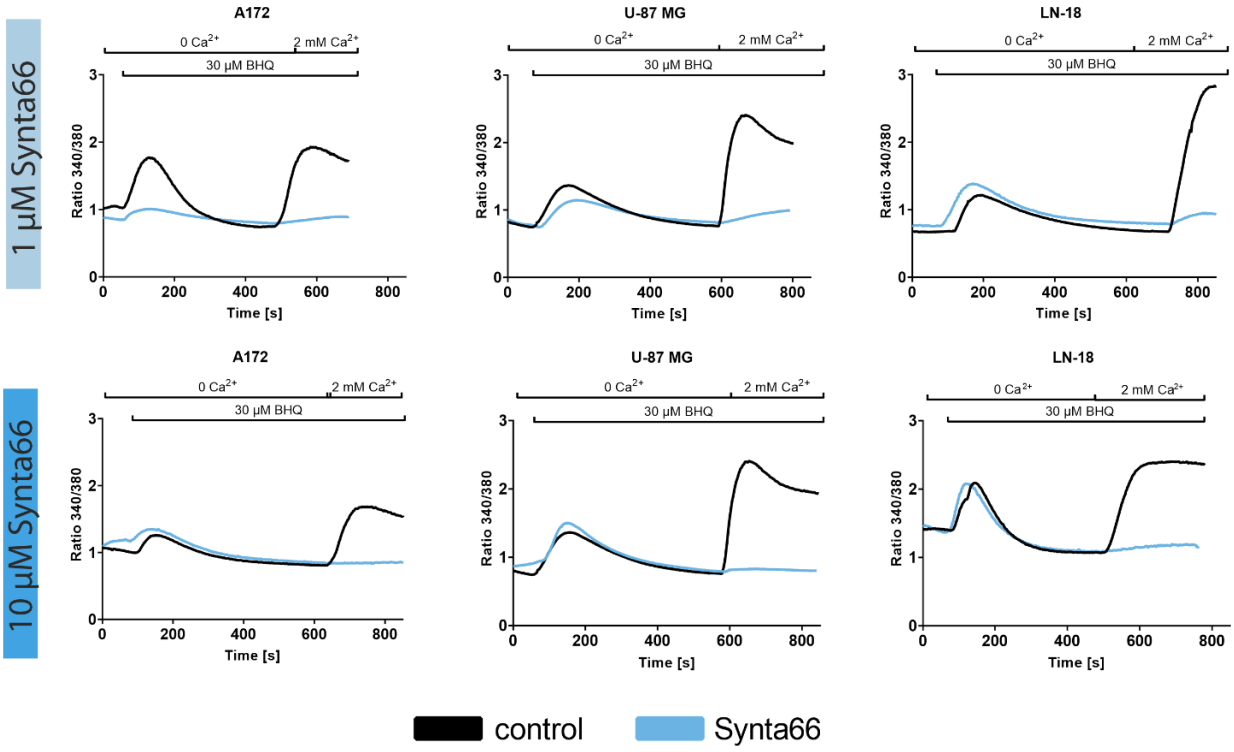

Figure 40 Cytosolic Ca^{2+} measurements in GBM cell lines with Synta66.
Representative traces of cells that were loaded with FURA-2 AM and monitored initially in a Ca^{2+} free extracellular solution followed by application of 30 µM BHQ and addition of 2 mM Ca^{2+} to monitor SOCE (black). Analogous experiments with pre-treatment of Synta66 (blue, 10 µM top, 1 µM bottom) immediately before the start of the experiment was used. Reproduced from (162). All co-authors have agreed to the inclusion of their published data in the dissertation. The reproduction of illustrations and figures has been granted from the publisher "MDPI Cancers" according to Creative Commons CC BY 4.0 license.

In the statistics on the relative SOCE (Figure 41), a potent inhibition of SOCE was also determined in A172 cells (no detectable SOCE), LN-18 cells (no detectable SOCE), as well as U-87 MG (7.0 ± 0.6 % remaining SOCE peak, Figure 41). Treatment with 1 µM Synta66, could also efficiently inhibit SOCE in GBM cell lines (Figure 41; remaining SOCE in A172 at 2.8 ± 0.3 %, in LN-18 cells 6.2 ± 0.4 % and in U-87 MG cells 14.8 ± 0.6 %). These findings clearly highlight that Synta66 is a robust inhibitor of SOC signaling in the three GBM cell lines A172, U-87 MG and LN-18.

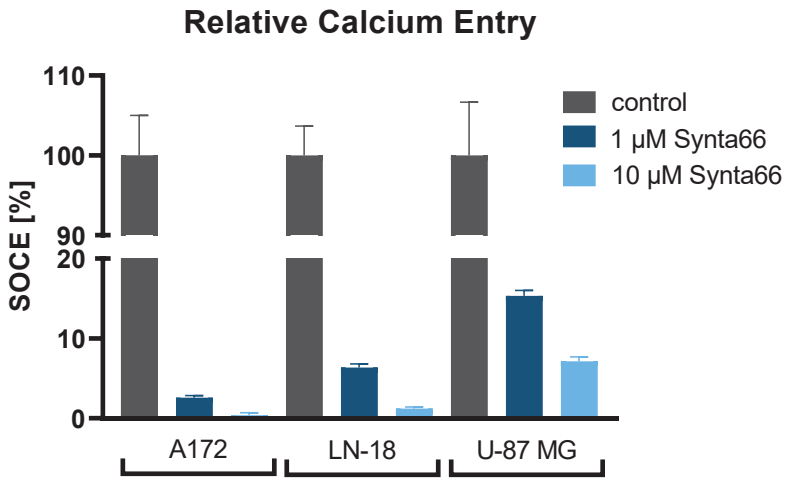

Figure 41 Statistical analysis of relative calcium entry in GBM cell lines treated with Synta66.
Reproduced from (162). All co-authors have agreed to the inclusion of their published data in the dissertation. The reproduction of illustrations and figures has been granted from the publisher "MDPI Cancers" according to Creative Commons CC BY 4.0 license.

In collaboration with Dr. Tiffner, we determined that Orai1 mediated Ca^{2+} currents are efficiently inhibited by 1 and 10 µM Synta66 (162). Remarkable, analogous experiments but with a non-selective Orai1-E106D pore mutant completely diminished the Synta66 mediated inhibition (162).

9.2. Synta66 partially enhances growth in LN-18 and U-87 MG cells

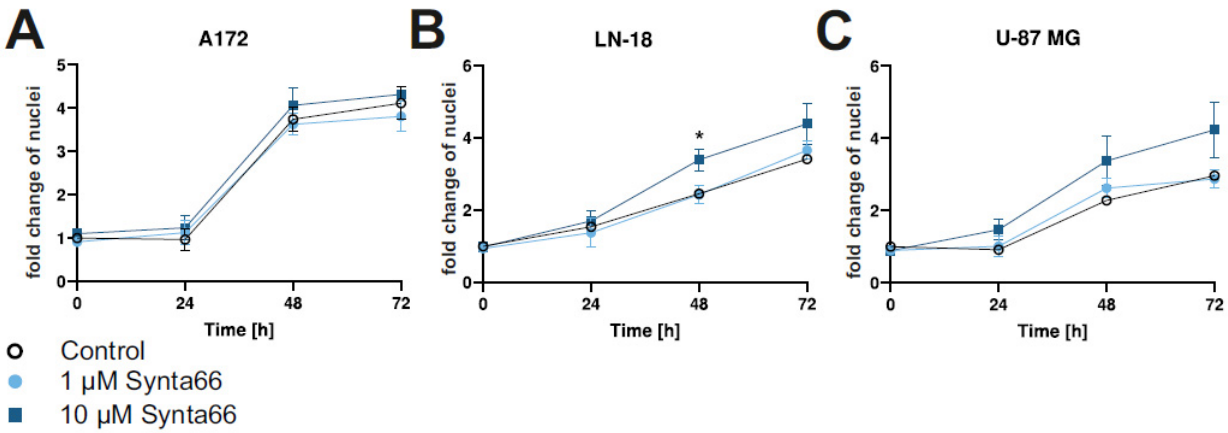

Figure 42 Effect of Synta66 on growth of GBM cell lines.
1 and 10 µM Synta66 are light and dark blue, respectively. (A) LN-18, (B) A172 and (C) U-87 MG was examined via Hoechst staining of nuclei. Signal was normalized to control signal at t=0 h, results shown as mean ± SEM, n=6 from two independent experiments; two-sided *t*-test, *: p-value < 0.05.

Previous experiments using pharmacological interference of SOCE have determined significant impairment of proliferation in various GBM cell lines, GBM1, GBM8 and U-251 MG (195, 198). We evaluated cell growth in A172, LN-18 and U-87 MG cell lines upon treatment with Synta66 (Figure 42) by quantification of Hoechst-stained nuclei in cultured cells at 24, 48 and 72 h after treatment. All three GBM cell lines treated with 1 µM Synta66 were comparable to vehicle-treated growth controls (0.1 % DMSO, Figure 42). Treatment with 10 µM Synta66, however, resulted in higher cell growth levels in LN-18 and U-87 MG cells at 48 h and 72 h (Figure 42B, C), though the differences were statistically significant only in LN-18 at 48 h (*: $p < 0.05$, two-sided t-test). A172 cells did not exhibit any noticeable differences (Figure 42A).

9.3. Synta66 slightly synergizes TMZ treatment in U-87 MG cells

Consequently, we determined the viability of the cells that were treated with 1 or 10 µM Synta66 for 24, 48 and 72 h. We observed that these Synta66 concentrations did not change cell viability drastically in any of the three cell lines (Figure 43).

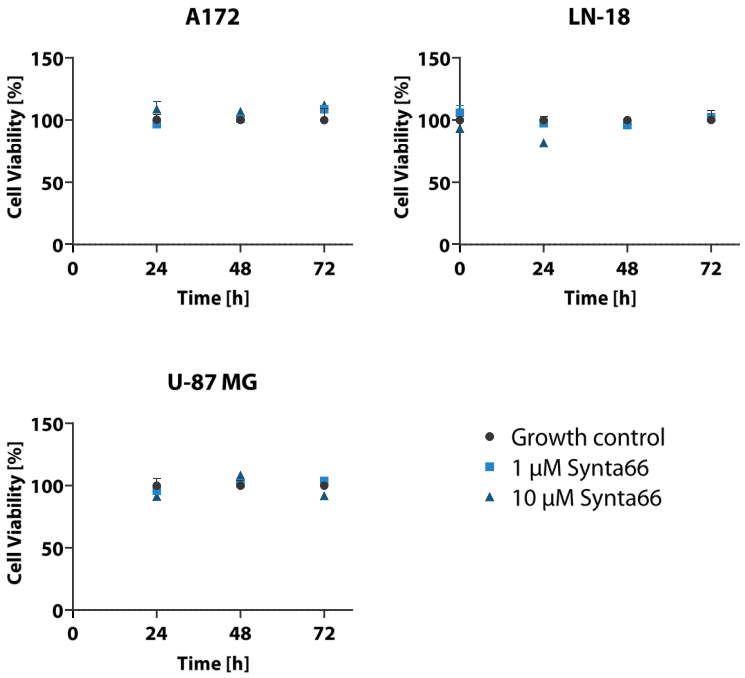

Figure 43 Cell viability of GBM cell lines treated with Synta66.
A172, LN-18 and U-87 MG were treated with 1 and 10 µM Synta66 for 72 h. Results are shown as mean ± SEM, n=6 from two independent experiments.
Reproduced from (162). All co-authors have agreed to the inclusion of their published data in the dissertation. The reproduction of illustrations and figures has been granted from the publisher "MDPI Cancers" according to Creative Commons CC BY 4.0 license.

Interestingly, the combination of Synta66 with TMZ showed that 10 µM Synta66 treatment increased the TMZ-sensitivity of U-87 MG cells at a statistically significant level (Figure 44A, IC_{50} TMZ alone = 3.7 mM, TMZ + 10 µM Synta66 = 1.4 mM, two-sided t-test, *:$p < 0.05$). In A172, increased TMZ sensitivity mediated by Synta66 was not significant (Figure 44B, IC_{50} TMZ alone = 4.4 mM, TMZ + 10µM Synta66 = 2.9 mM, two-sided t-test). In LN-18 cells, synergistic effects due to combinatory treatment of Synta66 with TMZ were not observed (Figure 44C).

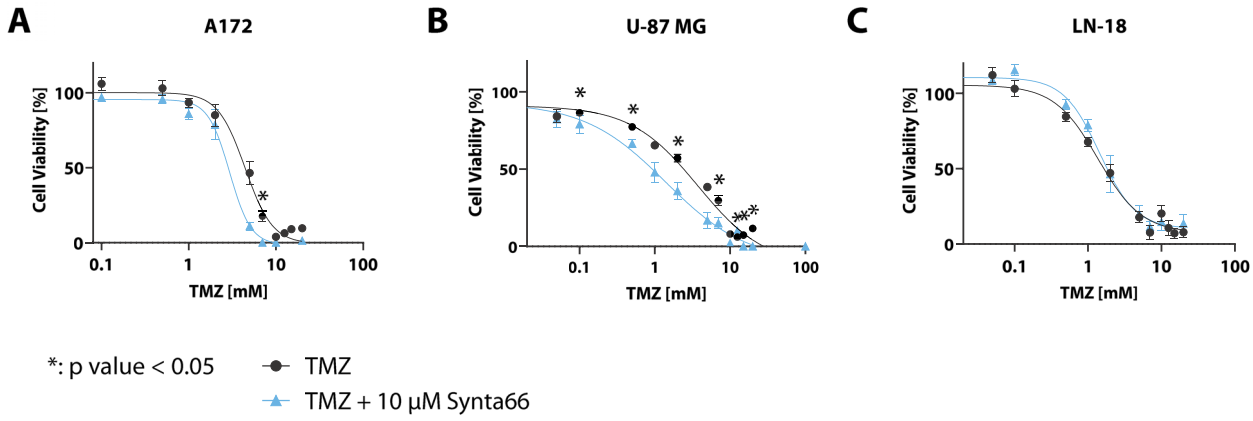

Figure 44 Cell viability after treatment with TMZ ± 10 µM Synta66.
Different TMZ concentration ± 10 µM Synta66 was observed in GBM cell lines after 72 h treatment via MTS assay. Cells were treated with fresh solutions of TMZ, in order to keep the DMSO concentration <0.1 %. Results shown as mean ± SEM, n=6 from two independent experiments, *: p-value < 0.05.
Reproduced from (162). All co-authors have agreed to the inclusion of their published data in the dissertation. The reproduction of illustrations and figures has been granted from the publisher "MDPI Cancers" according to Creative Commons CC BY 4.0 license.

9.4. Theoretical comparison of Synta66 with compound CM-4620

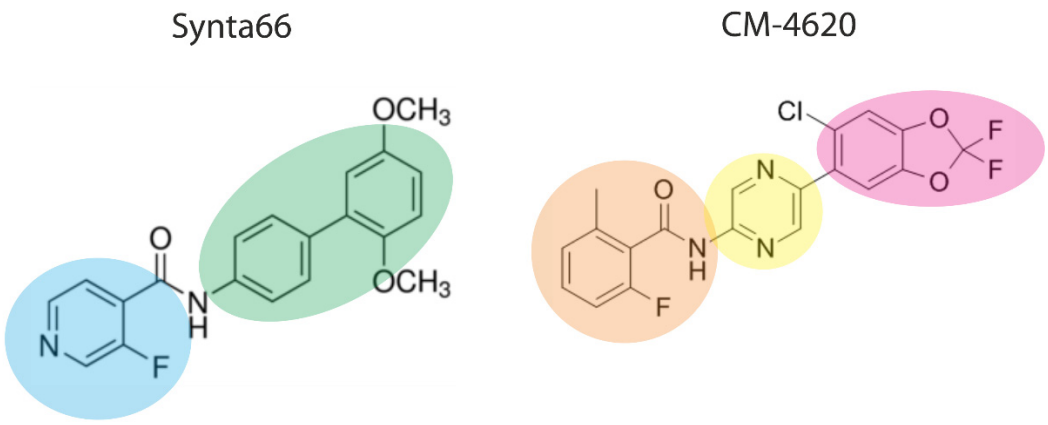

Figure 45 The two SOCE blockers Synta66 (left) and CM-4620 (right, PubChem CID 122507647).
Both images of simple structural formulas are ineligible for copyright and therefore in the public domain, because it consists entirely of information that is common property and contains no original authorship.

We also compared Synta66 (Figure 45, left) binding to Orai1 channel to SOC inhibitors with structural similarities. CM-4620 (Figure 45, right) is structurally related to Synta66 and currently

used in Clinical phase II trials for the treatment of pneumonia in COVID-19 patients and acute pancreatitis (42, 43). Considering the differences of the functional groups of both compounds, the specificity and binding affinity can be altered. Synta66 is based on a 3-fluoroisonicotinamide (Figure 45, blue), in which the nitrogen can function as a proton acceptor and has a lipophilic bi-aryl moiety (Figure 45, green). In comparison, CM-4620 is based on a 2-fluoro-6-methyl benzamide (Figure 45, orange) and carries no proton acceptor capabilities deriving from its benzamide ring structure. Attached to the basic structure is a pyrazine group (Figure 45, yellow, N as electron donor or acceptor), followed by a difluorobenzol[d][1,3]dioxole (Figure 45, pink), which adds lipophilic character to the molecule. The affinity of these ligands to the Orai pore may be comparable due to the general similarities of the basic structure. At the same time it is feasible that the introduction of functional groups, such as an dioxole moiety in CM-4620, promotes binding of the compounds to different regions of the Orai channel complex.

10. Discussion

It has been previously shown that targeting the SOCE signaling cascade in cancer has potential to interfere with tumor growth and progression. Genetic silencing of the STIM1/Orai1 proteins via siRNA interference have yielded promising reductions in tumor progression and metastasis in xenograft models of breast, cervical and prostate cancer cells (203, 204). In addition, siRNA interference against Orai3 largely suppressed prostate cancer tumor progression in nude mice (205). These and other findings have stimulated the research targeting SOCE inhibition in GBM cells. Favorable effects such as inhibition of growth, migration and proliferation of tumor cells caused by SOCE inhibitors DES, SKF-96365 and 2APB have been already shown in GBM *in vitro* (195, 196, 198, 200). Nevertheless, the specificity of these inhibitors was a question of interest since, for example, 2APB inhibits Orai1-mediated currents but instead stimulates Orai3 currents (206). Our experiments showed that Synta66 efficiently inhibited SOCE in three GBM cell lines, A172, LN-18 and U-87 MG. This blockage, however, did not result in any change in cell viability, in contrast to the previous studies that used less-specific inhibitors 2APB, DES and SKF-96365 or gene silencing for inhibition of SOCE in GBM cell lines (195-200). Another explanation for the

effects observed in these studies could be that the reported effects were not directly related to the disturbance of SOCE in these cells, but rather through disruption of other signaling mechanisms.

The inhibition of Orai channels by SOC inhibitors such as Synta66, BTP2 and GSK-7975A strongly depends on the Orai isoform (207). Recently, Zhang et al. showed that in Orai1 10 µM Synta66 indeed inhibit SOCE currents, but the same concentration of Synta66 stimulates Orai2 currents and does not affect Orai3 currents (207). The Synta66 block was also reduced in concatenated Orai dimers (207), which indicates that the SOC channels in the observed GBM cell lines U-87 MG, A172 and LN-18 are mainly constituted of Orai1 isoform. Consequently, different constitution of Orai channels in physiological conditions and different GBM cell lines may lead to different observations of SOCE inhibition mediated by Synta66 in GBM.

We summarize that in our experiments Synta66 interacts with high selectivity with the Orai1 pore and thus efficiently blocks SOCE in GBM cells. By performing patch clamp experiments, we proved that STIM1/Orai1 currents are completely inhibited by Synta66. Instead, Orai pore mutants with less Ca^{2+} selectivity (Orai1 E106D and H134A) also showed diminished sensitivity to Synta66 inhibition (162). We observed in FRET experiments that the inhibitory effect of Synta66 does not rely interfere with STIM1-STIM1 or STIM1-Orai1 coupling (162). In cell viability tests, we could neither observe significant reduction of GBM cell viability over 72 h among Synta66 treatment, nor interference with GBM growth. Also, Synta66 did only partially increase sensitivity of GBM cell lines to TMZ. Due to its high specificity to the Orai1 pore we consider Synta66 a useful and precise tool to evaluate the influence of Orai1 channels in cancer signaling pathways.

11. Bibliography

1. Hanif F, Muzaffar K, Perveen K, Malhi SM, Simjee Sh U. Glioblastoma Multiforme: A Review of its Epidemiology and Pathogenesis through Clinical Presentation and Treatment. Asian Pac J Cancer Prev. 2017;18(1):3-9.
2. Bray F, Ferlay J, Soerjomataram I, Siegel RL, Torre LA, Jemal A. Global cancer statistics 2018: GLOBOCAN estimates of incidence and mortality worldwide for 36 cancers in 185 countries. CA Cancer J Clin. 2018;68(6):394-424.
3. Ostrom QT, Gittleman H, Farah P, Ondracek A, Chen Y, Wolinsky Y, et al. CBTRUS Statistical Report: Primary Brain and Central Nervous System Tumors Diagnosed in the United States in 2006-2010. Neuro Oncol. 2013;15(suppl_2):ii1-ii56.
4. Batash R, Asna * N, Schaffer P, Schaffer NF, Moshe. Glioblastoma Multiforme, Diagnosis and Treatment; Recent Literature Review. Current Medicinal Chemistry. 2017.
5. Thakkar JP, Dolecek TA, Horbinski C, Ostrom QT, Lightner DD, Barnholtz-Sloan JS, et al. Epidemiologic and molecular prognostic review of glioblastoma. Cancer Epidemiol Biomarkers Prev. 2014;23(10):1985-96.
6. Tamimi AF, Juweid M. Epidemiology and Outcome of Glioblastoma. In: De Vleeschouwer S, editor. Glioblastoma. Brisbane (AU): Codon Publications; 2017.
7. Stensjøen AL, Solheim O, Kvistad KA, Håberg AK, Salvesen Ø, Berntsen EM. Growth dynamics of untreated glioblastomas in vivo. Neuro Oncol. 2015;17(10):1402-11.
8. Davis M. Glioblastoma: Overview of Disease and Treatment. Clinical Journal of Oncology Nursing. 2016;20(5):S2-S8.
9. Lombardi MY, Assem M. Glioblastoma Genomics: A Very Complicated Story. In: De Vleeschouwer S, editor. Glioblastoma. Brisbane (AU): Codon Publications

Copyright: The Authors.; 2017.
10. De Vleeschouwer S, Bergers G. Glioblastoma: To Target the Tumor Cell or the Microenvironment? In: De Vleeschouwer S, editor. Glioblastoma. Brisbane (AU): Codon Publications

Copyright: The Authors.; 2017.
11. Sottoriva A, Spiteri I, Piccirillo SG, Touloumis A, Collins VP, Marioni JC, et al. Intratumor heterogeneity in human glioblastoma reflects cancer evolutionary dynamics. Proc Natl Acad Sci U S A. 2013;110(10):4009-14.
12. Weathers SP, de Groot J. VEGF Manipulation in Glioblastoma. Oncology (Williston Park). 2015;29(10):720-7.
13. Wesseling P, Ruiter DJ, Burger PC. Angiogenesis in brain tumors; pathobiological and clinical aspects. J Neurooncol. 1997;32(3):253-65.
14. Colwell N, Larion M, Giles AJ, Seldomridge AN, Sizdahkhani S, Gilbert MR, et al. Hypoxia in the glioblastoma microenvironment: shaping the phenotype of cancer stem-like cells. Neuro Oncol. 2017;19(7):887-96.
15. Singh SK, Hawkins C, Clarke ID, Squire JA, Bayani J, Hide T, et al. Identification of human brain tumour initiating cells. Nature. 2004;432(7015):396-401.

16. Dawood S, Austin L, Cristofanilli M. Cancer stem cells: implications for cancer therapy. Oncology (Williston Park). 2014;28(12):1101-7, 10.
17. Singh SK, Clarke ID, Hide T, Dirks PB. Cancer stem cells in nervous system tumors. Oncogene. 2004;23(43):7267-73.
18. Najafi M, Mortezaee K, Majidpoor J. Cancer stem cell (CSC) resistance drivers. Life Sci. 2019;234:116781.
19. Bao S, Wu Q, McLendon RE, Hao Y, Shi Q, Hjelmeland AB, et al. Glioma stem cells promote radioresistance by preferential activation of the DNA damage response. Nature. 2006;444(7120):756-60.
20. Cheray M, Bégaud G, Deluche E, Nivet A, Battu S, Lalloué F, et al. Cancer Stem-Like Cells in Glioblastoma. In: De Vleeschouwer S, editor. Glioblastoma. Brisbane (AU): Codon Publications

21. Xu HS, Qin XL, Zong HL, He XG, Cao L. Cancer stem cell markers in glioblastoma - an update. Eur Rev Med Pharmacol Sci. 2017;21(14):3207-11.
22. Alameda F, Velarde JM, Carrato C, Vidal N, Arumí M, Naranjo D, et al. Prognostic value of stem cell markers in glioblastoma. Biomarkers. 2019;24(7):677-83.
23. Elsir T, Edqvist PH, Carlson J, Ribom D, Bergqvist M, Ekman S, et al. A study of embryonic stem cell-related proteins in human astrocytomas: identification of Nanog as a predictor of survival. Int J Cancer. 2014;134(5):1123-31.
24. Mooney KL, Choy W, Sidhu S, Pelargos P, Bui TT, Voth B, et al. The role of CD44 in glioblastoma multiforme. J Clin Neurosci. 2016;34:1-5.
25. Uribe D, Torres Á, Rocha JD, Niechi I, Oyarzún C, Sobrevia L, et al. Multidrug resistance in glioblastoma stem-like cells: Role of the hypoxic microenvironment and adenosine signaling. Mol Aspects Med. 2017;55:140-51.
26. Calabrese C, Poppleton H, Kocak M, Hogg TL, Fuller C, Hamner B, et al. A perivascular niche for brain tumor stem cells. Cancer Cell. 2007;11(1):69-82.
27. Kaur B, Khwaja FW, Severson EA, Matheny SL, Brat DJ, Van Meir EG. Hypoxia and the hypoxia-inducible-factor pathway in glioma growth and angiogenesis. Neuro Oncol. 2005;7(2):134-53.
28. Heddleston JM, Li Z, McLendon RE, Hjelmeland AB, Rich JN. The hypoxic microenvironment maintains glioblastoma stem cells and promotes reprogramming towards a cancer stem cell phenotype. Cell Cycle. 2009;8(20):3274-84.
29. Glass R, Synowitz M. CNS macrophages and peripheral myeloid cells in brain tumours. Acta Neuropathol. 2014;128(3):347-62.
30. Hambardzumyan D, Gutmann DH, Kettenmann H. The role of microglia and macrophages in glioma maintenance and progression. Nat Neurosci. 2016;19(1):20-7.
31. Gieryng A, Pszczolkowska D, Walentynowicz KA, Rajan WD, Kaminska B. Immune microenvironment of gliomas. Lab Invest. 2017;97(5):498-518.
32. Coniglio SJ, Eugenin E, Dobrenis K, Stanley ER, West BL, Symons MH, et al. Microglial stimulation of glioblastoma invasion involves epidermal growth factor receptor (EGFR) and colony stimulating factor 1 receptor (CSF-1R) signaling. Mol Med. 2012;18(1):519-27.

33. Bettinger I, Thanos S, Paulus W. Microglia promote glioma migration. Acta Neuropathol. 2002;103(4):351-5.
34. Carvalho da Fonseca AC, Wang H, Fan H, Chen X, Zhang I, Zhang L, et al. Increased expression of stress inducible protein 1 in glioma-associated microglia/macrophages. J Neuroimmunol. 2014;274(1-2):71-7.
35. Stupp R, Mason WP, van den Bent MJ, Weller M, Fisher B, Taphoorn MJB, et al. Radiotherapy plus Concomitant and Adjuvant Temozolomide for Glioblastoma. New England Journal of Medicine. 2005;352(10):987-96.
36. Gilbert MR, Dignam JJ, Armstrong TS, Wefel JS, Blumenthal DT, Vogelbaum MA, et al. A randomized trial of bevacizumab for newly diagnosed glioblastoma. N Engl J Med. 2014;370(8):699-708.
37. Chinot OL, Wick W, Mason W, Henriksson R, Saran F, Nishikawa R, et al. Bevacizumab plus radiotherapy-temozolomide for newly diagnosed glioblastoma. N Engl J Med. 2014;370(8):709-22.
38. Li YM, Suki D, Hess K, Sawaya R. The influence of maximum safe resection of glioblastoma on survival in 1229 patients: Can we do better than gross-total resection? J Neurosurg. 2016;124(4):977-88.
39. Fernandes C, Costa A, Osório L, Lago RC, Linhares P, Carvalho B, et al. Current Standards of Care in Glioblastoma Therapy. In: De Vleeschouwer S, editor. Glioblastoma. Brisbane (AU): Codon Publications; 2017.
40. Chaichana KL, Jusue-Torres I, Navarro-Ramirez R, Raza SM, Pascual-Gallego M, Ibrahim A, et al. Establishing percent resection and residual volume thresholds affecting survival and recurrence for patients with newly diagnosed intracranial glioblastoma. Neuro Oncol. 2014;16(1):113-22.
41. Hadjipanayis CG, Stummer W. 5-ALA and FDA approval for glioma surgery. J Neurooncol. 2019;141(3):479-86.
42. De Witt Hamer PC, Robles SG, Zwinderman AH, Duffau H, Berger MS. Impact of intraoperative stimulation brain mapping on glioma surgery outcome: a meta-analysis. J Clin Oncol. 2012;30(20):2559-65.
43. Grabowski MM, Recinos PF, Nowacki AS, Schroeder JL, Angelov L, Barnett GH, et al. Residual tumor volume versus extent of resection: predictors of survival after surgery for glioblastoma. J Neurosurg. 2014;121(5):1115-23.
44. Gilbert MR, Wang M, Aldape KD, Stupp R, Hegi ME, Jaeckle KA, et al. Dose-dense temozolomide for newly diagnosed glioblastoma: a randomized phase III clinical trial. J Clin Oncol. 2013;31(32):4085-91.
45. Feng E, Sui C, Wang T, Sun G. Temozolomide with or without Radiotherapy in Patients with Newly Diagnosed Glioblastoma Multiforme: A Meta-Analysis. Eur Neurol. 2017;77(3-4):201-10.
46. Stupp R, Roila F. Malignant glioma: ESMO Clinical Recommendations for diagnosis, treatment and follow-up. Ann Oncol. 2009;20(suppl_4):iv126-iv8.

47. Kazda T, Dziacky A, Burkon P, Pospisil P, Slavik M, Rehak Z, et al. Radiotherapy of Glioblastoma 15 Years after the Landmark Stupp's Trial: More Controversies than Standards? Radiol Oncol. 2018;52(2):121-8.
48. Denny BJ, Wheelhouse RT, Stevens MF, Tsang LL, Slack JA. NMR and molecular modeling investigation of the mechanism of activation of the antitumor drug temozolomide and its interaction with DNA. Biochemistry. 1994;33(31):9045-51.
49. Marchesi F, Turriziani M, Tortorelli G, Avvisati G, Torino F, De Vecchis L. Triazene compounds: mechanism of action and related DNA repair systems. Pharmacol Res. 2007;56(4):275-87.
50. Lee SY. Temozolomide resistance in glioblastoma multiforme. Genes & Diseases. 2016;3(3):198-210.
51. Uno M, Oba-Shinjo SM, Camargo AA, Moura RP, Aguiar PH, Cabrera HN, et al. Correlation of MGMT promoter methylation status with gene and protein expression levels in glioblastoma. Clinics (Sao Paulo). 2011;66(10):1747-55.
52. van Nifterik KA, van den Berg J, van der Meide WF, Ameziane N, Wedekind LE, Steenbergen RDM, et al. Absence of the MGMT protein as well as methylation of the MGMT promoter predict the sensitivity for temozolomide. British Journal of Cancer. 2010;103(1):29-35.
53. Ewend MG, Brem S, Gilbert M, Goodkin R, Penar PL, Varia M, et al. Treatment of Single Brain Metastasis with Resection, Intracavity Carmustine Polymer Wafers, and Radiation Therapy Is Safe and Provides Excellent Local Control. Clin Cancer Res. 2007;13(12):3637-41.
54. Brem H, Piantadosi S, Burger PC, Walker M, Selker R, Vick NA, et al. Placebo-controlled trial of safety and efficacy of intraoperative controlled delivery by biodegradable polymers of chemotherapy for recurrent gliomas. The Lancet. 1995;345(8956):1008-12.
55. Bregy A, Shah AH, Diaz MV, Pierce HE, Ames PL, Diaz D, et al. The role of Gliadel wafers in the treatment of high-grade gliomas. Expert Rev Anticancer Ther. 2013;13(12):1453-61.
56. Gallego JM, Barcia JA, Barcia-Mariño C. Fatal outcome related to carmustine implants in glioblastoma multiforme. Acta Neurochir (Wien). 2007;149(3):261-5; discussion 5.
57. Ashby LS, Smith KA, Stea B. Gliadel wafer implantation combined with standard radiotherapy and concurrent followed by adjuvant temozolomide for treatment of newly diagnosed high-grade glioma: a systematic literature review. World J Surg Oncol. 2016;14(1).
58. Petrecca K, Guiot MC, Panet-Raymond V, Souhami L. Failure pattern following complete resection plus radiotherapy and temozolomide is at the resection margin in patients with glioblastoma. J Neurooncol. 2013;111(1):19-23.
59. Chamberlain MC. Radiographic patterns of relapse in glioblastoma. J Neurooncol. 2011;101(2):319-23.
60. Minniti G, Amelio D, Amichetti M, Salvati M, Muni R, Bozzao A, et al. Patterns of failure and comparison of different target volume delineations in patients with glioblastoma treated with conformal radiotherapy plus concomitant and adjuvant temozolomide. Radiother Oncol. 2010;97(3):377-81.
61. Oh J, Sahgal A, Sanghera P, Tsao MN, Davey P, Lam K, et al. Glioblastoma: patterns of recurrence and efficacy of salvage treatments. Can J Neurol Sci. 2011;38(4):621-5.

62. McDonald MW, Shu HK, Curran WJ, Jr., Crocker IR. Pattern of failure after limited margin radiotherapy and temozolomide for glioblastoma. Int J Radiat Oncol Biol Phys. 2011;79(1):130-6.
63. Weller M, van den Bent M, Tonn JC, Stupp R, Preusser M, Cohen-Jonathan-Moyal E, et al. European Association for Neuro-Oncology (EANO) guideline on the diagnosis and treatment of adult astrocytic and oligodendroglial gliomas. Lancet Oncol. 2017;18(6):e315-e29.
64. Weller M, Cloughesy T, Perry JR, Wick W. Standards of care for treatment of recurrent glioblastoma—are we there yet? Neuro Oncol. 2012;15(1):4-27.
65. Wick W, Fricke H, Junge K, Kobyakov G, Martens T, Heese O, et al. A phase II, randomized, study of weekly APG101+reirradiation versus reirradiation in progressive glioblastoma. Clin Cancer Res. 2014;20(24):6304-13.
66. Debinski W, Gibo DM, Hulet SW, Connor JR, Gillespie GY. Receptor for interleukin 13 is a marker and therapeutic target for human high-grade gliomas. Clin Cancer Res. 1999;5(5):985-90.
67. Mintz A, Gibo DM, Slagle-Webb B, Christensen ND, Debinski W. IL-13Ralpha2 is a glioma-restricted receptor for interleukin-13. Neoplasia. 2002;4(5):388-99.
68. Wykosky J, Gibo DM, Stanton C, Debinski W. Interleukin-13 receptor alpha 2, EphA2, and Fos-related antigen 1 as molecular denominators of high-grade astrocytomas and specific targets for combinatorial therapy. Clin Cancer Res. 2008;14(1):199-208.
69. Hamaoka Y, Negishi M, Katoh H. EphA2 is a key effector of the MEK/ERK/RSK pathway regulating glioblastoma cell proliferation. Cell Signal. 2016;28(8):937-45.
70. Wykosky J, Gibo DM, Stanton C, Debinski W. EphA2 as a novel molecular marker and target in glioblastoma multiforme. Mol Cancer Res. 2005;3(10):541-51.
71. Toyama M, Hamaoka Y, Katoh H. EphA3 is up-regulated by epidermal growth factor and promotes formation of glioblastoma cell aggregates. Biochem Biophys Res Commun. 2019;508(3):715-21.
72. Day BW, Stringer BW, Al-Ejeh F, Ting MJ, Wilson J, Ensbey KS, et al. EphA3 maintains tumorigenicity and is a therapeutic target in glioblastoma multiforme. Cancer Cell. 2013;23(2):238-48.
73. Debinski W, Priebe W, Tatter SB. Maximizing Local Access to Therapeutic Deliveries in Glioblastoma. Part I: Targeted Cytotoxic Therapy. In: De Vleeschouwer S, editor. Glioblastoma. Brisbane (AU): Codon Publications

74. Qiu W, Song S, Chen W, Zhang J, Yang H, Chen Y. Hypoxia-induced EPHB2 promotes invasive potential of glioblastoma. Int J Clin Exp Pathol. 2019;12(2):539-48.
75. Kunwar S, Prados MD, Chang SM, Berger MS, Lang FF, Piepmeier JM, et al. Direct intracerebral delivery of cintredekin besudotox (IL13-PE38QQR) in recurrent malignant glioma: a report by the Cintredekin Besudotox Intraparenchymal Study Group. J Clin Oncol. 2007;25(7):837-44.
76. Vogelbaum MA, Sampson JH, Kunwar S, Chang SM, Shaffrey M, Asher AL, et al. Convection-enhanced delivery of cintredekin besudotox (interleukin-13-PE38QQR) followed by radiation therapy with and without temozolomide in newly diagnosed malignant gliomas: phase 1 study of final safety results. Neurosurgery. 2007;61(5):1031-7; discussion 7-8.

77. Kunwar S, Chang S, Westphal M, Vogelbaum M, Sampson J, Barnett G, et al. Phase III randomized trial of CED of IL13-PE38QQR vs Gliadel wafers for recurrent glioblastoma. Neuro Oncol. 2010;12(8):871-81.
78. Bobo RH, Laske DW, Akbasak A, Morrison PF, Dedrick RL, Oldfield EH. Convection-enhanced delivery of macromolecules in the brain. Proc Natl Acad Sci U S A. 1994;91(6):2076-80.
79. Lieberman DM, Laske DW, Morrison PF, Bankiewicz KS, Oldfield EH. Convection-enhanced distribution of large molecules in gray matter during interstitial drug infusion. J Neurosurg. 1995;82(6):1021-9.
80. The Cure Parkinson's Trust. The GDNF trial (as seen on BBC2) 2019 [Available from: https://www.parkinsonsmovement.com/tag/convection-enhanced-delivery-ced/.
81. Elenes EY, Rylander CG. Maximizing Local Access to Therapeutic Deliveries in Glioblastoma. Part II: Arborizing Catheter for Convection-Enhanced Delivery in Tissue Phantoms. In: De Vleeschouwer S, editor. Glioblastoma. Brisbane (AU): Codon Publications

82. Ksendzovsky A, Walbridge S, Saunders RC, Asthagiri AR, Heiss JD, Lonser RR. Convection-enhanced delivery of M13 bacteriophage to the brain. J Neurosurg. 2012;117(2):197-203.
83. Mehta AM, Sonabend AM, Bruce JN. Convection-Enhanced Delivery. Neurotherapeutics. 2017;14(2):358-71.
84. Jahangiri A, Chin AT, Flanigan PM, Chen R, Bankiewicz K, Aghi MK. Convection-enhanced delivery in glioblastoma: a review of preclinical and clinical studies. J Neurosurg. 2017;126(1):191-200.
85. Chen MY, Lonser RR, Morrison PF, Governale LS, Oldfield EH. Variables affecting convection-enhanced delivery to the striatum: a systematic examination of rate of infusion, cannula size, infusate concentration, and tissue-cannula sealing time. J Neurosurg. 1999;90(2):315-20.
86. Tanner PG, Holtmannspötter M, Tonn JC, Goldbrunner R. Effects of drug efflux on convection-enhanced paclitaxel delivery to malignant gliomas: technical note. Neurosurgery. 2007;61(4):E880-2; discussion E2.
87. Varenika V, Dickinson P, Bringas J, LeCouteur R, Higgins R, Park J, et al. Detection of infusate leakage in the brain using real-time imaging of convection-enhanced delivery. J Neurosurg. 2008;109(5):874-80.
88. Jahangiri A, Chin AT, Flanigan PM, Chen R, Bankiewicz K, Aghi MK. Convection-enhanced delivery in glioblastoma: a review of preclinical and clinical studies. Journal of neurosurgery. 2017;126(1):191-200.
89. Shi M, Sanche L. Convection-Enhanced Delivery in Malignant Gliomas: A Review of Toxicity and Efficacy. J Oncol. 2019;2019:9342796.
90. Deipolyi AR, Golberg A, Yarmush ML, Arellano RS, Oklu R. Irreversible electroporation: evolution of a laboratory technique in interventional oncology. Diagn Interv Radiol. 2014;20(2):147-54.
91. Lorenzo MF, Arena CB, Davalos RV. Maximizing Local Access to Therapeutic Deliveries in Glioblastoma. Part III: Irreversible Electroporation and High-Frequency Irreversible

Electroporation for the Eradication of Glioblastoma. In: De Vleeschouwer S, editor. Glioblastoma. Brisbane (AU): Codon Publications

92. Beebe SJ, Fox PM, Rec LJ, Willis EL, Schoenbach KH. Nanosecond, high-intensity pulsed electric fields induce apoptosis in human cells. Faseb j. 2003;17(11):1493-5.
93. Li W, Fan Q, Ji Z, Qiu X, Li Z. The effects of irreversible electroporation (IRE) on nerves. PLOS ONE. 2011;6(4):e18831-e.
94. Ellis TL, Garcia PA, Rossmeisl JH, Jr., Henao-Guerrero N, Robertson J, Davalos RV. Nonthermal irreversible electroporation for intracranial surgical applications. Laboratory investigation. J Neurosurg. 2011;114(3):681-8.
95. Rossmeisl JH, Jr., Garcia PA, Pancotto TE, Robertson JL, Henao-Guerrero N, Neal RE, 2nd, et al. Safety and feasibility of the NanoKnife system for irreversible electroporation ablative treatment of canine spontaneous intracranial gliomas. J Neurosurg. 2015;123(4):1008-25.
96. Phenix CP, Togtema M, Pichardo S, Zehbe I, Curiel L. High intensity focused ultrasound technology, its scope and applications in therapy and drug delivery. J Pharm Pharm Sci. 2014;17(1):136-53.
97. Sattiraju A, Sun Y, Solingapuram Sai KK, Li KCP, Mintz A. Maximizing Local Access to Therapeutic Deliveries in Glioblastoma. Part IV: Image-Guided, Remote-Controlled Opening of the Blood–Brain Barrier for Systemic Brain Tumor Therapy. In: De Vleeschouwer S, editor. Glioblastoma. Brisbane (AU): Codon Publications

98. Ter Haar G. HIFU Tissue Ablation: Concept and Devices. Adv Exp Med Biol. 2016;880:3-20.
99. Aryal M, Vykhodtseva N, Zhang YZ, Park J, McDannold N. Multiple treatments with liposomal doxorubicin and ultrasound-induced disruption of blood-tumor and blood-brain barriers improve outcomes in a rat glioma model. J Control Release. 2013;169(1-2):103-11.
100. Park EJ, Zhang YZ, Vykhodtseva N, McDannold N. Ultrasound-mediated blood-brain/blood-tumor barrier disruption improves outcomes with trastuzumab in a breast cancer brain metastasis model. J Control Release. 2012;163(3):277-84.
101. Svennersten K, Larsson KC, Berggren M, Richter-Dahlfors A. Organic bioelectronics in nanomedicine. Biochim Biophys Acta. 2011;1810(3):276-85.
102. Svirskis D, Travas-Sejdic J, Rodgers A, Garg S. Electrochemically controlled drug delivery based on intrinsically conducting polymers. J Control Release. 2010;146(1):6-15.
103. Wadhwa R, Lagenaur CF, Cui XT. Electrochemically controlled release of dexamethasone from conducting polymer polypyrrole coated electrode. J Control Release. 2006;110(3):531-41.
104. Miller LL, Zhou XQ. Poly(N-methylpyrrolylium) poly(styrenesulfonate) - a conductive, electrically switchable cation exchanger that cathodically binds and anodically releases dopamine. Macromolecules. 1987;20(7):1594-7.
105. Hepel M, Mahdavi F. Application of the Electrochemical Quartz Crystal Microbalance for Electrochemically Controlled Binding and Release of Chlorpromazine from Conductive Polymer Matrix. Microchemical Journal. 1997;56(1):54-64.

106. Sanjay ST, Zhou W, Dou M, Tavakoli H, Ma L, Xu F, et al. Recent advances of controlled drug delivery using microfluidic platforms. Adv Drug Deliv Rev. 2018;128:3-28.
107. Proctor CM, Slézia A, Kaszas A, Ghestem A, Agua Id, Pappa A-M, et al. Electrophoretic drug delivery for seizure control. Science Advances. 2018;4(8):eaau1291.
108. Fritsch RJ, Krause I. ELECTROPHORESIS. In: Caballero B, editor. Encyclopedia of Food Sciences and Nutrition (Second Edition). Oxford: Academic Press; 2003. p. 2055-62.
109. Stringer R. ELECTROPHORESIS | Overview. In: Worsfold P, Townshend A, Poole C, editors. Encyclopedia of Analytical Science (Second Edition). Oxford: Elsevier; 2005. p. 356-63.
110. Gas B. ELECTROPHORESIS | Principles. In: Worsfold P, Townshend A, Poole C, editors. Encyclopedia of Analytical Science (Second Edition). Oxford: Elsevier; 2005. p. 363-70.
111. Sjöström TA, Berggren M, Gabrielsson EO, Janson P, Poxson DJ, Seitanidou M, et al. A Decade of Iontronic Delivery Devices. Advanced Materials Technologies. 2018;3(5):1700360.
112. Seitanidou M, Tybrandt K, Berggren M, Simon DT. Overcoming transport limitations in miniaturized electrophoretic delivery devices. Lab Chip. 2019;19(8):1427-35.
113. Isaksson J, Kjäll P, Nilsson D, Robinson ND, Berggren M, Richter-Dahlfors A. Electronic control of Ca2+ signalling in neuronal cells using an organic electronic ion pump. Nat Mater. 2007;6(9):673-9.
114. Simon DT, Kurup S, Larsson KC, Hori R, Tybrandt K, Goiny M, et al. Organic electronics for precise delivery of neurotransmitters to modulate mammalian sensory function. Nat Mater. 2009;8(9):742-6.
115. Jonsson A, Song Z, Nilsson D, Meyerson BA, Simon DT, Linderoth B, et al. Therapy using implanted organic bioelectronics. Science Advances. 2015;1(4):e1500039.
116. Seitanidou M, Franco-Gonzalez JF, Sjöström TA, Zozoulenko I, Berggren M, Simon DT. pH Dependence of γ-Aminobutyric Acid Iontronic Transport. J Phys Chem B. 2017;121(30):7284-9.
117. Uguz I, Proctor CM, Curto VF, Pappa A-M, Donahue MJ, Ferro M, et al. A Microfluidic Ion Pump for In Vivo Drug Delivery. Advanced Materials. 2017;29(27):1701217.
118. Seitanidou M, Blomgran R, Pushpamithran G, Berggren M, Simon DT. Modulating Inflammation in Monocytes Using Capillary Fiber Organic Electronic Ion Pumps. Advanced Healthcare Materials. 2019;8(19):1900813.
119. Poxson DJ, Karady M, Gabrielsson R, Alkattan AY, Gustavsson A, Doyle SM, et al. Regulating plant physiology with organic electronics. PNAS. 2017;114(18):4597-602.
120. Bernacka-Wojcik I, Huerta M, Tybrandt K, Karady M, Mulla MY, Poxson DJ, et al. Implantable Organic Electronic Ion Pump Enables ABA Hormone Delivery for Control of Stomata in an Intact Tobacco Plant. Small. 2019.
121. Stukov AN, Filatova LV, Latipova DK, Bespalov VG, Belyaeva OA, Kireeva GS, et al. [Therapeutic activity of gemcitabine in intracranial tumors]. Vopr Onkol. 2015;61(2):274-9.
122. Pauwels B, Korst AEC, Lardon F, Vermorken JB. Combined Modality Therapy of Gemcitabine and Radiation. The Oncologist. 2005;10(1):34-51.
123. Vanderveken OM, Szturz P, Specenier P, Merlano MC, Benasso M, Van Gestel D, et al. Gemcitabine-Based Chemoradiation in the Treatment of Locally Advanced Head and Neck Cancer: Systematic Review of Literature and Meta-Analysis. The Oncologist. 2016;21(1):59-71.

124. Bastiancich C, Bastiat G, Lagarce F. Gemcitabine and glioblastoma: challenges and current perspectives. Drug Discovery Today. 2018;23(2):416-23.
125. Szegezdi J, Csizmadia F. Prediction of dissociation co.2.
126. Szegezdi J, Csizmadia F. A method for calculating the pKa values of small and large molecules.2.
127. Seitanidou M. Overcoming Limitations of Iontronic Delivery Devices: Linköping University Electronic Press; 2020.
128. Singh R, Shakya AK, Naik R, Shalan N. Stability-Indicating HPLC Determination of Gemcitabine in Pharmaceutical Formulations. International Journal of Analytical Chemistry. 2015.
129. Zhu D, Tu M, Zeng B, Cai L, Zheng W, Su Z, et al. Up-regulation of miR-497 confers resistance to temozolomide in human glioma cells by targeting mTOR/Bcl-2. Cancer Med. 2017;6(2):452-62.
130. Chahal M, Xu Y, Lesniak D, Graham K, Famulski K, Christensen JG, et al. MGMT modulates glioblastoma angiogenesis and response to the tyrosine kinase inhibitor sunitinib. Neuro Oncol. 2010;12(8):822-33.
131. Agnihotri S, Gajadhar AS, Ternamian C, Gorlia T, Diefes KL, Mischel PS, et al. Alkylpurine-DNA-N-glycosylase confers resistance to temozolomide in xenograft models of glioblastoma multiforme and is associated with poor survival in patients. J Clin Invest. 2012;122(1):253-66.
132. Meir EGV, Kikuchi T, Tada M, Li H, Diserens A-C, Wojcik BE, et al. Analysis of the p53 Gene and Its Expression in Human Glioblastoma Cells. Cancer Research. 1994;54(3):649-52.
133. Perazzoli G, Prados J, Ortiz R, Caba O, Cabeza L, Berdasco M, et al. Temozolomide Resistance in Glioblastoma Cell Lines: Implication of MGMT, MMR, P-Glycoprotein and CD133 Expression. PLOS ONE. 2015;10(10):e0140131.
134. Rieger J, Durka S, Streffer J, Dichgans J, Weller M. Gemcitabine cytotoxicity of human malignant glioma cells: modulation by antioxidants, BCL-2 and dexamethasone. European Journal of Pharmacology. 1999;365(2-3):301-8.
135. Hermisson M, Klumpp A, Wick W, Wischhusen J, Nagel G, Roos W, et al. O6-methylguanine DNA methyltransferase and p53 status predict temozolomide sensitivity in human malignant glioma cells. Journal of Neurochemistry. 2006;96(3):766-76.
136. Happold C, Roth P, Wick W, Schmidt N, Florea A-M, Silginer M, et al. Distinct molecular mechanisms of acquired resistance to temozolomide in glioblastoma cells. Journal of Neurochemistry. 2012;122(2):444-55.
137. Martin SJ, Reutelingsperger CP, McGahon AJ, Rader JA, van Schie RC, LaFace DM, et al. Early redistribution of plasma membrane phosphatidylserine is a general feature of apoptosis regardless of the initiating stimulus: inhibition by overexpression of Bcl-2 and Abl. J Exp Med. 1995;182(5):1545-56.
138. Dubessy C, Merlin JM, Marchal C, Guillemin F. Spheroids in radiobiology and photodynamic therapy. Crit Rev Oncol Hematol. 2000;36(2-3):179-92.
139. Hirschhaeuser F, Menne H, Dittfeld C, West J, Mueller-Klieser W, Kunz-Schughart LA. Multicellular tumor spheroids: an underestimated tool is catching up again. J Biotechnol. 2010;148(1):3-15.

140. Koledova Z. 3D Cell Culture: An Introduction. In: Koledova Z, editor. 3D Cell Culture: Methods and Protocols. Methods in Molecular Biology. New York, NY: Springer New York; 2017. p. 1-11.
141. Benton G, DeGray G, Kleinman HK, George J, Arnaoutova I. In vitro microtumors provide a physiologically predictive tool for breast cancer therapeutic screening. PLOS ONE. 2015;10(4):e0123312-e.
142. Degen JW, Walbridge S, Vortmeyer AO, Oldfield EH, Lonser RR. Safety and efficacy of convection-enhanced delivery of gemcitabine or carboplatin in a malignant glioma model in rats. J Neurosurg. 2003;99(5):893-8.
143. Murad GJ, Walbridge S, Morrison PF, Szerlip N, Butman JA, Oldfield EH, et al. Image-guided convection-enhanced delivery of gemcitabine to the brainstem. J Neurosurg. 2007;106(2):351-6.
144. Abrahamsson T, Poxson DJ, Gabrielsson EO, Sandberg M, Simon DT, Berggren M. Formation of Monolithic Ion-Selective Transport Media Based on "Click" Cross-Linked Hyperbranched Polyglycerol. Front Chem. 2019;7:484.
145. Poxson DJ, Gabrielsson EO, Bonisoli A, Linderhed U, Abrahamsson T, Matthiesen I, et al. Capillary-Fiber Based Electrophoretic Delivery Device. ACS applied materials & interfaces. 2019;11(15):14200-7.
146. Fleig A, Parekh AB. New insights into Ca(2+) channel function in health and disease. J Physiol. 2017;595(10):2997-8.
147. Berna-Erro A, Woodard GE, Rosado JA. Orais and STIMs: physiological mechanisms and disease. J Cell Mol Med. 2012;16(3):407-24.
148. Rosado JA, Diez R, Smani T, Jardín I. STIM and Orai1 Variants in Store-Operated Calcium Entry. Front Pharmacol. 2015;6:325.
149. Bogeski I, Kilch T, Niemeyer BA. ROS and SOCE: recent advances and controversies in the regulation of STIM and Orai. J Physiol. 2012;590(17):4193-200.
150. Ong HL, Subedi KP, Son GY, Liu X, Ambudkar IS. Tuning store-operated calcium entry to modulate Ca(2+)-dependent physiological processes. Biochim Biophys Acta Mol Cell Res. 2019;1866(7):1037-45.
151. Muik M, Fahrner M, Derler I, Schindl R, Bergsmann J, Frischauf I, et al. A Cytosolic Homomerization and a Modulatory Domain within STIM1 C Terminus Determine Coupling to ORAI1 Channels. J Biol Chem. 2009;284(13):8421-6.
152. Navarro-Borelly L, Somasundaram A, Yamashita M, Ren D, Miller RJ, Prakriya M. STIM1-Orai1 interactions and Orai1 conformational changes revealed by live-cell FRET microscopy. J Physiol. 2008;586(22):5383-401.
153. Wang Y, Deng X, Zhou Y, Hendron E, Mancarella S, Ritchie MF, et al. STIM protein coupling in the activation of Orai channels. Proc Natl Acad Sci U S A. 2009;106(18):7391-6.
154. Böhm J, Chevessier F, Maues De Paula A, Koch C, Attarian S, Feger C, et al. Constitutive activation of the calcium sensor STIM1 causes tubular-aggregate myopathy. Am J Hum Genet. 2013;92(2):271-8.
155. Misceo D, Holmgren A, Louch WE, Holme PA, Mizobuchi M, Morales RJ, et al. A dominant STIM1 mutation causes Stormorken syndrome. Hum Mutat. 2014;35(5):556-64.

156. Hou X, Pedi L, Diver MM, Long SB. Crystal structure of the calcium release-activated calcium channel Orai. Science. 2012;338(6112):1308-13.
157. Hoth M, Penner R. Calcium release-activated calcium current in rat mast cells. J Physiol. 1993;465:359-86.
158. Fahrner M, Derler I, Jardin I, Romanin C. The STIM1/Orai signaling machinery. Channels (Austin). 2013;7(5):330-43.
159. Hou X, Outhwaite IR, Pedi L, Long SB. Cryo-EM structure of the calcium release-activated calcium channel Orai in an open conformation. bioRxiv. 2020:2020.09.03.281964.
160. McNally BA, Somasundaram A, Yamashita M, Prakriya M. Gated regulation of CRAC channel ion selectivity by STIM1. Nature. 2012;482(7384):241-5.
161. Frischauf I, Litviňuková M, Schober R, Zayats V, Svobodová B, Bonhenry D, et al. Transmembrane helix connectivity in Orai1 controls two gates for calcium-dependent transcription. Sci Signal. 2017;10(507).
162. Waldherr L, Tiffner A, Mishra D, Sallinger M, Schober R, Frischauf I, et al. Blockage of Store-Operated Ca(2+) Influx by Synta66 is Mediated by Direct Inhibition of the Ca(2+) Selective Orai1 Pore. Cancers (Basel). 2020;12(10).
163. Prakriya M, Lewis RS. Regulation of CRAC Channel Activity by Recruitment of Silent Channels to a High Open-probability Gating Mode. Journal of General Physiology. 2006;128(3):373-86.
164. Krizova A, Maltan L, Derler I. Critical parameters maintaining authentic CRAC channel hallmarks. European Biophysics Journal. 2019;48(5):425-45.
165. Prakriya M, Feske S, Gwack Y, Srikanth S, Rao A, Hogan PG. Orai1 is an essential pore subunit of the CRAC channel. Nature. 2006;443(7108):230-3.
166. Vig M, Beck A, Billingsley JM, Lis A, Parvez S, Peinelt C, et al. CRACM1 Multimers Form the Ion-Selective Pore of the CRAC Channel. Current Biology. 2006;16(20):2073-9.
167. Yamashita M, Navarro-Borelly L, McNally BA, Prakriya M. Orai1 Mutations Alter Ion Permeation and Ca2+-dependent Fast Inactivation of CRAC Channels: Evidence for Coupling of Permeation and Gating. Journal of General Physiology. 2007;130(5):525-40.
168. Yeung PS, Yamashita M, Ing CE, Pomès R, Freymann DM, Prakriya M. Mapping the functional anatomy of Orai1 transmembrane domains for CRAC channel gating. Proc Natl Acad Sci U S A. 2018;115(22):E5193-e202.
169. Stathopulos PB, Li G-Y, Plevin MJ, Ames JB, Ikura M. Stored Ca2+ depletion-induced oligomerization of stromal interaction molecule 1 (STIM1) via the EF-SAM region: An initiation mechanism for capacitive Ca2+ entry. J Biol Chem. 2006;281(47):35855-62.
170. Huang Y, Zhou Y, Wong HC, Chen Y, Chen Y, Wang S, et al. A single EF-hand isolated from STIM1 forms dimer in the absence and presence of Ca2+. Febs j. 2009;276(19):5589-97.
171. Kar P, Nelson C, Parekh AB. Selective activation of the transcription factor NFAT1 by calcium microdomains near Ca2+ release-activated Ca2+ (CRAC) channels. J Biol Chem. 2011;286(17):14795-803.
172. Schober R, Waldherr L, Schmidt T, Graziani A, Stilianu C, Legat L, et al. STIM1 and Orai1 regulate Ca(2+) microdomains for activation of transcription. Biochim Biophys Acta Mol Cell Res. 2019;1866(7):1079-91.

173. Smyth JT, Dehaven WI, Bird GS, Putney JW, Jr. Ca2+-store-dependent and -independent reversal of Stim1 localization and function. J Cell Sci. 2008;121(Pt 6):762-72.
174. Baba Y, Hayashi K, Fujii Y, Mizushima A, Watarai H, Wakamori M, et al. Coupling of STIM1 to store-operated Ca2+ entry through its constitutive and inducible movement in the endoplasmic reticulum. Proc Natl Acad Sci U S A. 2006;103(45):16704-9.
175. Ong HL, de Souza LB, Zheng C, Cheng KT, Liu X, Goldsmith CM, et al. STIM2 enhances receptor-stimulated Ca(2)(+) signaling by promoting recruitment of STIM1 to the endoplasmic reticulum-plasma membrane junctions. Sci Signal. 2015;8(359):ra3.
176. Bird GS, Hwang SY, Smyth JT, Fukushima M, Boyles RR, Putney JW, Jr. STIM1 is a calcium sensor specialized for digital signaling. Curr Biol. 2009;19(20):1724-9.
177. Li Z, Lu J, Xu P, Xie X, Chen L, Xu T. Mapping the interacting domains of STIM1 and Orai1 in Ca2+ release-activated Ca2+ channel activation. J Biol Chem. 2007;282(40):29448-56.
178. Fahrner M, Derler I, Jardin I, Romanin C. The STIM1/Orai signaling machinery. Channels (Austin). 2013;7(5):330-43.
179. Stathopulos PB, Zheng L, Li GY, Plevin MJ, Ikura M. Structural and mechanistic insights into STIM1-mediated initiation of store-operated calcium entry. Cell. 2008;135(1):110-22.
180. Stathopulos PB, Schindl R, Fahrner M, Zheng L, Gasmi-Seabrook GM, Muik M, et al. STIM1/Orai1 coiled-coil interplay in the regulation of store-operated calcium entry. Nat Commun. 2013;4.
181. Yuan JP, Zeng W, Dorwart MR, Choi YJ, Worley PF, Muallem S. SOAR and the polybasic STIM1 domains gate and regulate Orai channels. Nat Cell Biol. 2009;11(3):337-43.
182. Park CY, Hoover PJ, Mullins FM, Bachhawat P, Covington ED, Raunser S, et al. STIM1 clusters and activates CRAC channels via direct binding of a cytosolic domain to Orai1. Cell. 2009;136(5):876-90.
183. Luik RM, Wang B, Prakriya M, Wu MM, Lewis RS. Oligomerization of STIM1 couples ER calcium depletion to CRAC channel activation. Nature. 2008;454(7203):538-42.
184. Stathopulos PB, Zheng L, Ikura M. Stromal interaction molecule (STIM) 1 and STIM2 calcium sensing regions exhibit distinct unfolding and oligomerization kinetics. J Biol Chem. 2009;284(2):728-32.
185. Zhou Y, Mancarella S, Wang Y, Yue C, Ritchie M, Gill DL, et al. The short N-terminal domains of STIM1 and STIM2 control the activation kinetics of Orai1 channels. J Biol Chem. 2009;284(29):19164-8.
186. Schober R, Bonhenry D, Lunz V, Zhu J, Krizova A, Frischauf I, et al. Sequential activation of STIM1 links Ca(2+) with luminal domain unfolding. Sci Signal. 2019;12(608).
187. Sallinger M, Tiffner A, Schmidt T, Bonhenry D, Waldherr L, Frischauf I, et al. Luminal STIM1 Mutants that Cause Tubular Aggregate Myopathy Promote Autophagic Processes. Int J Mol Sci. 2020;21(12).
188. Hirve N, Rajanikanth V, Hogan PG, Gudlur A. Coiled-Coil Formation Conveys a STIM1 Signal from ER Lumen to Cytoplasm. Cell Rep. 2018;22(1):72-83.
189. Zhou Y, Srinivasan P, Razavi S, Seymour S, Meraner P, Gudlur A, et al. Initial activation of STIM1, the regulator of store-operated calcium entry. Nat Struct Mol Biol. 2013;20(8):973-81.

190. Tian C, Du L, Zhou Y, Li M. Store-operated CRAC channel inhibitors: opportunities and challenges. Future Med Chem. 2016;8(7):817-32.
191. Monteith GR, Prevarskaya N, Roberts-Thomson SJ. The calcium-cancer signalling nexus. Nat Rev Cancer. 2017;17(6):367-80.
192. Hoth M. CRAC channels, calcium, and cancer in light of the driver and passenger concept. Biochim Biophys Acta. 2016;1863(6 Pt B):1408-17.
193. Prevarskaya N, Skryma R, Shuba Y. Ion Channels in Cancer: Are Cancer Hallmarks Oncochannelopathies? Physiol Rev. 2018;98(2):559-621.
194. Toth AB, Hori K, Novakovic MM, Bernstein NG, Lambot L, Prakriya M. CRAC channels regulate astrocyte Ca(2+) signaling and gliotransmitter release to modulate hippocampal GABAergic transmission. Sci Signal. 2019;12(582).
195. Liu H, Hughes JD, Rollins S, Chen B, Perkins E. Calcium entry via ORAI1 regulates glioblastoma cell proliferation and apoptosis. Exp Mol Pathol. 2011;91(3):753-60.
196. Kovacs GG, Zsembery A, Anderson SJ, Komlosi P, Gillespie GY, Bell PD, et al. Changes in intracellular Ca2+ and pH in response to thapsigargin in human glioblastoma cells and normal astrocytes. Am J Physiol Cell Physiol. 2005;289(2):C361-71.
197. Shi ZX, Rao W, Wang H, Wang ND, Si JW, Zhao J, et al. Modeled microgravity suppressed invasion and migration of human glioblastoma U87 cells through downregulating store-operated calcium entry. Biochem Biophys Res Commun. 2015;457(3):378-84.
198. Motiani RK, Hyzinski-Garcia MC, Zhang X, Henkel MM, Abdullaev IF, Kuo YH, et al. STIM1 and Orai1 mediate CRAC channel activity and are essential for human glioblastoma invasion. Pflugers Arch. 2013;465(9):1249-60.
199. Li G, Zhang Z, Wang R, Ma W, Yang Y, Wei J, et al. Suppression of STIM1 inhibits human glioblastoma cell proliferation and induces G0/G1 phase arrest. J Exp Clin Cancer Res. 2013;32:20.
200. Zhu M, Chen L, Zhao P, Zhou H, Zhang C, Yu S, et al. Store-operated Ca(2+) entry regulates glioma cell migration and invasion via modulation of Pyk2 phosphorylation. J Exp Clin Cancer Res. 2014;33:98.
201. Stauderman KA. CRAC channels as targets for drug discovery and development. Cell Calcium. 2018;74:147-59.
202. Dorr K, Kilch T, Kappel S, Alansary D, Schwar G, Niemeyer BA, et al. Cell type-specific glycosylation of Orai1 modulates store-operated Ca2+ entry. Sci Signal. 2016;9(418):ra25.
203. Yang S, Zhang JJ, Huang XY. Orai1 and STIM1 are critical for breast tumor cell migration and metastasis. Cancer Cell. 2009;15(2):124-34.
204. Chen YF, Chiu WT, Chen YT, Lin PY, Huang HJ, Chou CY, et al. Calcium store sensor stromal-interaction molecule 1-dependent signaling plays an important role in cervical cancer growth, migration, and angiogenesis. Proc Natl Acad Sci U S A. 2011;108(37):15225-30.
205. Dubois C, Vanden Abeele F, Lehen'kyi V, Gkika D, Guarmit B, Lepage G, et al. Remodeling of channel-forming ORAI proteins determines an oncogenic switch in prostate cancer. Cancer Cell. 2014;26(1):19-32.

206. Schindl R, Bergsmann J, Frischauf I, Derler I, Fahrner M, Muik M, et al. 2-aminoethoxydiphenyl borate alters selectivity of Orai3 channels by increasing their pore size. J Biol Chem. 2008;283(29):20261-7.
207. Zhang X, Xin P, Yoast RE, Emrich SM, Johnson MT, Pathak T, et al. Distinct pharmacological profiles of ORAI1, ORAI2, and ORAI3 channels. Cell Calcium. 2020;91:102281.